Formation and Physical Properties of Novel Carbonaceous Nano-Materials

冨田，知志

(Degree)
博士（理学）

(Date of Degree)
2002-03-31

(Date of Publication)
2008-05-30

(Resource Type)
doctoral thesis

(Report Number)
甲2563

(URL)
https://hdl.handle.net/20.500.14094/D1002563

博　士　論　文

Formation and Physical Properties of Novel Carbonaceous Nano-Materials

新規な炭素系ナノ物質の形成と物性に関する研究

平成 14 年 1 月

神戸大学大学院自然科学研究科

冨田　知志

Contents

Chapter 1

General Introduction

1.1 Classical Carbonaceous Materials

1.1.1 Carbon allotropes

Carbon, the sixth element of the periodic table and listed at the top of column IV, is a remarkable material. The interests of carbon material fundamentally originate from a variety of chemical bonding styles, which has never been seen in other elements [1, 2]. Each carbon atom has six electrons which occupy $1s^2$, $2s^2$, and $2p^2$ atomic orbitals. The $1s^2$ orbital contains two strongly bound core electrons and they are called core electrons. Four more weakly bound electrons occupy the $2s^2 2p^2$ valence orbitals and are called valence electrons. In the crystalline phase, the valence electrons give rise to $2s$, $2p_x$, $2p_y$, and $2p_z$ orbitals which are important in forming covalent bonds in carbon materials. Since the energy difference between the lower $2s$ level and upper $2p$ levels is small compared with the binding energy of the chemical bonds, the electric wave functions of these four electrons can readily mix with each other, thereby changing the occupation of one $2s$ and three $2p$ atomic orbitals so as to enhance the binding energy of the C atom with its neighboring atoms. In contrast to other group IV elements such as Si and Ge, the absence of nearby inner orbitals except for the spherical $1s$ orbital facilitates hybridizations involving only valence s and p orbitals for carbon. The mixing of a single $2s$ electron with one, two, or three $2p$ electrons is called sp^n hybridization with n=1,2,3. As a results, in principle, a carbon atom can adopt three different bonding configurations, sp, sp^2, and sp^3 as shown in Fig. 1.1 [3].

These bonding styles realize the atoms to form a variety of carbon allotropes. The most famous carbon allotropes are diamond and graphite. Diamond, one of the most brilliant and hardest gems, has three dimensional structure. The structure originates from the tetrahedrally directed sp^3 hybrid orbitals which form strong σ bonds with adjacent atoms

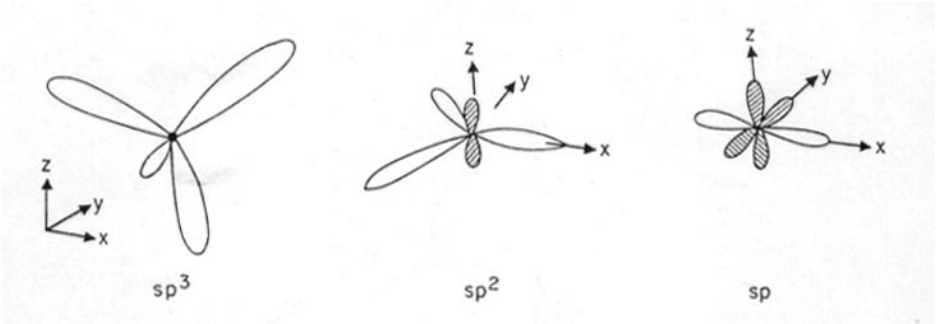

Figure 1.1: Schematic representation of sp^3, sp^2, and sp hybridized atoms [3].

Table 1.1: Several key properties of graphite and diamond [3, 2].

	Structure	a_{c-c}(nm)	Electronic states	E_g(eV)	Density(g·cm^{-3})
Graphite	Hexagonal	0.142 (C=C)	Semimetal	-	2.267
Diamond	Tetrahedral	0.154 (C-C)	Insulating	5.47	3.515

at angles of 109.5°. On the contrary, graphite is basically composed of two-dimensional sp^2 network, called graphene. At a carbon sp^2 site in the graphene, three of the four electrons are assigned to the trigonally directed sp^2 hybrid orbitals, which form σ bonds at angles of 120° between the segments connecting nearest-neighbor atoms. The fourth electron lies in a p_z orbital lying normal to the σ bonding plane. The p_z orbitals form weaker π bonds with adjacent p_z orbitals. These sp^2 graphene sheets are weakly connected each other by van der Waals force, leading to the formation of graphite structure (quasi-two-dimensional system). Several key properties of graphite and diamond are given in Table 1.1. The table clearly shows that the different bonding configurations give rise to completely different properties between two allotropes. In addition to diamond and graphite, carbyne consisting of sp bondings is proposed as one-dimensional allotrope. At sp site, only two of the electrons form σ bonds, along $\pm x$ in Fig. 1.1, and the two other electrons are left in orthogonal p_y and p_z orbitals to form π bonds. Among three allotropes of carbon, we will focus on graphite and describe the fundamental properties in detail in a following subsection.

1.1.2 Fundamental properties of graphite

The ideal structure of graphite is the ground state for the infinite crystal of carbon. Figure 1.2(a) shows the crystalline structure of graphite. As already mentioned, this crystal structure consists of layers in which the carbon atoms are arranged in an open

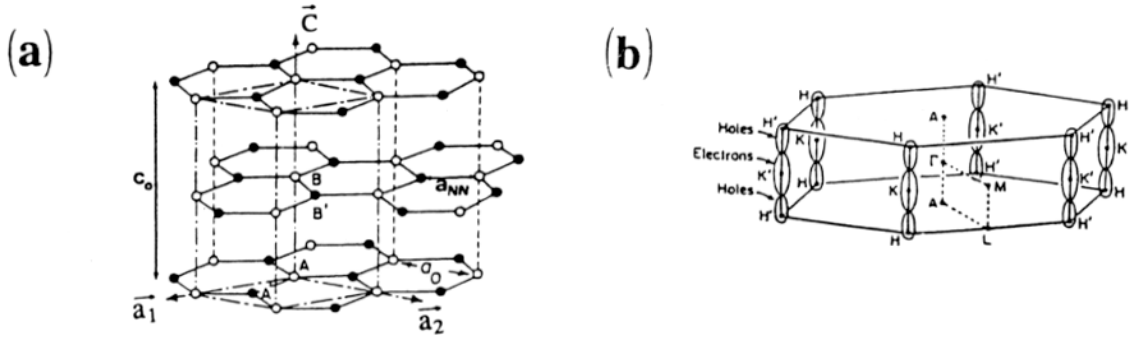

Figure 1.2: (a) Crystalline structure of hexagonal graphite. The dimensions of the unit cell, which is represented by dotted-dashed lines, are a_0 and c_0. a_{NN} is the distance between nearest neighbors. (b) Graphite Brillouin zone and a schematic version of the graphite electron and hole Fermi surfaces located along the $H - K$ axes [4, 5].

honeycomb network (graphene) containing two atoms per unit cell in each layer with a small in-plane nearest neighbor distance a_{c-c} of 0.1421 nm and an in-plane lattice constant a_0 of 0.2462 nm. The sp^2 graphene layers are stacked in the ABAB stacking sequence with a c-axis lattice constant c_0 of 0.6708 nm and an interplanar distance $c_0/2$ of ~ 0.3354 nm. This crystal structure is consistent with the D^4_{6h} ($P6_3/mmc$) space group and has four carbon atoms per unit cell. The interplanar distance (0.3354 nm) is much larger than the in-plane nearest and second neighbor distance (0.1421 nm and 0.2462 nm, respectively), implying the weak connection between the graphene layers. Therefore, the electronic structure of graphite is mainly governed by that of a 2D graphene sheet.

Because of two carbon atoms per unit cell in the graphene, the unit cell contains six σ electrons and two π electrons. These electrons forms eight electronic bands in the graphene sheet. The first four bands (three bonding σ bands and one bonding π band) are occupied by electrons while the last four (three antibonding σ^* bands and one antibonding π^* band) are empty. Since the π states are weakly bound, they lies closer to the Fermi level (E_F) than the σ states. As a result, the filled π band will form the valence band and the empty π^* band will form the conduction band. Figure 1.3(a) illustrates the schematic representation of electron density of states around E_F for graphene sheet [6]. Owing to symmetry properties, π and π^* bands are degenerate at the K point of the 2D Brillouin zone. The 2D graphene is thus a zero-gap semiconductor.

The interaction between graphene sheets modifies this situation and create a semimetal for graphite. In crystalline graphite, a unit cell contains four π electrons, and thus two valence π bands and two conduction π bands are formed as shown in Fig. 1.4. Two valence

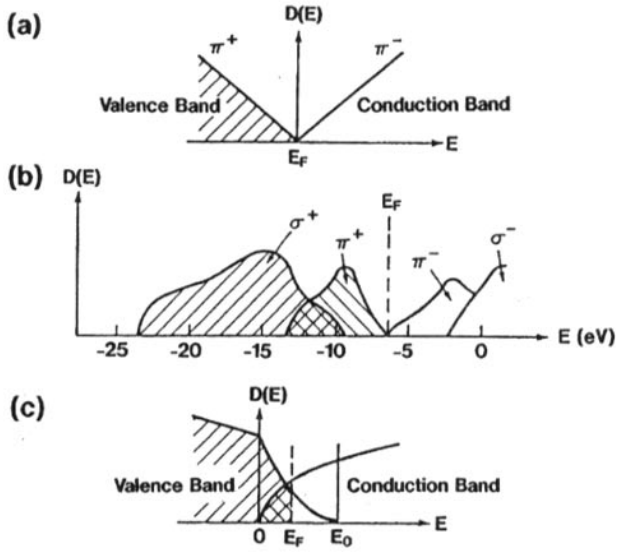

Figure 1.3: Schematic illustration of electron density of states: around E_F for a graphene sheet (a), in entire energy region for graphite (b) and around E_F for graphite (c) [6].

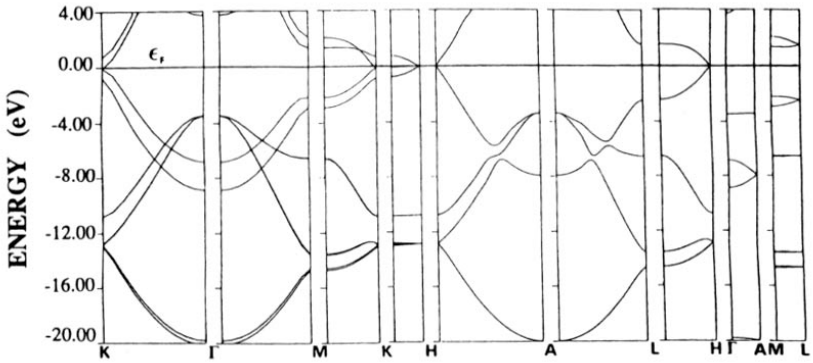

Figure 1.4: *AB initio* band structure of graphite along different lines in the Brillouin zone calculated by Charlier *et al.* [5].

π bands are completely occupied by electrons. The interplanar interaction brings about a slight overlap (about 0.04 eV) between valence and conduction π bands as shown in Figs. 1.3(b) and (c). This overlap gives rise to the generation of conduction π electrons in graphite. The electron and hole Fermi surfaces located along the $H-K$ axes in Brillouin zone of graphite is shown in Fig. 1.2(b). Due to the slight overlap, the carrier density in graphite is much lower ($\sim 5\times10^{24}$ m^{-3}) than that in metal. The conductivity of graphite is, however, comparable to that of metal mainly owing to the small effective mass of the carriers in the graphene plane.

The graphene layers often do not form the perfect graphite crystal structure with perfect ABAB layer stacking. Instead, stacking faults, which means departures from the ABAB stacking order, are formed and these faults give rise to a small increase in the inter layer distance ($c_0/2$) from the value of 0.3354 nm in quasi-2D graphite until about 0.3440 nm, at which the stacking of the individual carbon layers becomes uncorrelated. The resulting structure of these uncorrelated 2D graphene layers is called turbostratic graphite. In addition to the stacking faults, a series of defects, e.g., dangling bonds, bond angle disorder, bond length disorder, and hybridization, in the graphene planes is contained in so-called disordered graphite. These defects seriously affect and drastically change the properties of graphite. A further increase in the number of defects finally leads to the formation of the completely disordered three-dimensional carbon material, in which both sp^2 and sp^3 hybridizations are randomly present, so-called amorphous carbon.

The structure of graphite, in other words, the degree of disorder in graphite structure, can be studied by observing the lattice vibrational modes [7]. For the investigation of phonon mode structures, three complementary experimental techniques are especially important: inelastic neutron scattering, Raman and infrared spectroscopy. While inelastic neutron scattering is capable of exploring the phonon modes in the entire Brillouin zone, infrared and Raman spectroscopy probe predominantly zone-center modes. Graphite crystallizes according to the D^4_{6h} space group and has twelve phonon modes at $q=0$. These modes are classified as two silent modes ($2B_{1g}$), three acoustic modes (A_{2u}+E_{1u}), three infrared-active modes(A_{2u}+E_{1u}), and four Raman active modes ($2E_{2g}$). Zone-center optical phonon modes are shown in Fig. 1.5.

For decades, Raman spectroscopy has proven to be a simple but powerful tool for observing phonon modes of graphite related materials. As mentioned in the above, owing to the small wave vector of light relative to Brillouin zone dimensions in solids, first-order Raman scattering is, in principle, confined to the excitation of phonon modes close to the zone-center in phonon dispersion curves. Information on the phonon dispersion relations for zone-edge in the Brillouin zone as shown in Fig. 1.6(a) [8] can be obtained from second-order Raman spectra, where contributions are made by pairs of phonons with

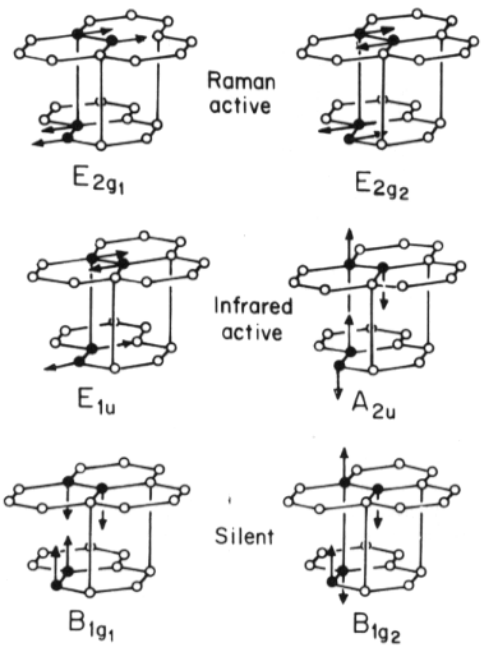

Figure 1.5: Zone-center optical phonon modes in graphite [7]. For the in-plane modes (E_{1u}, E_{2g_1}, E_{2g_2}), only one of the degenerate pair of modes is shown. The c-axis modes (A_{2u}, E_{1g_1}, E_{1g_2}) are nondegenerated. Infrared and Raman activities are indicated. The zero frequency acoustic modes (E_{1u}, A_{2u}) corresponding to pure translations are not shown.

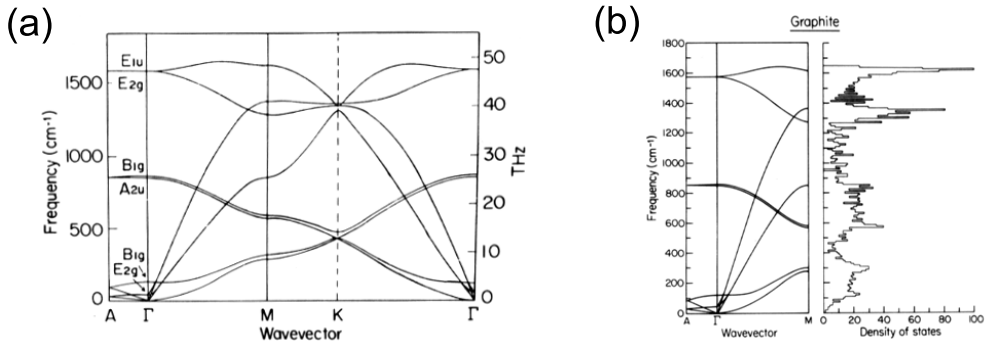

Figure 1.6: (a) Graphite phonon dispersion curves along several high symmetry axes from Maeda *et al.* [8]. Zone-center phonon modes are indicated at Γ-point. (b) Phonon dispersion relations and the corresponding phonon density of states by Leung *et al.* [12].

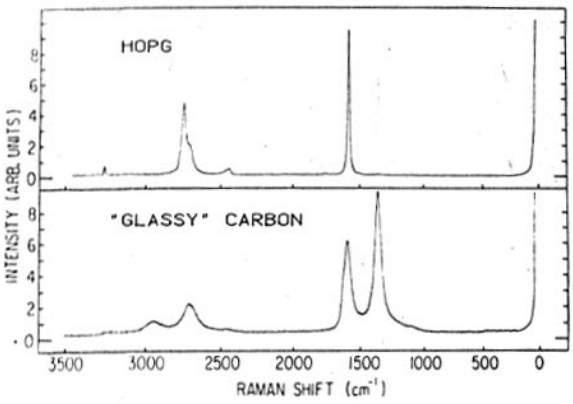

Figure 1.7: Typical first- and second-order Raman spectra of highly oriented pyrolytic graphite (HOPG) and "grassy" carbon [9].

vectors q and $-q$. Figure 1.7 shows typical first- and second-order Raman spectra of highly oriented pyrolytic graphite (HOPG) and "grassy" carbon [9]. Both the first-order Raman spectra in Fig. 1.7 exhibit a band at 1582 cm^{-1}. This band corresponds to E_{2g_2} modes in graphite as shown in Fig. 1.6(a). Since the band is commonly observed for graphite related materials, it is called G band. In addition to G band, the first-order Raman spectrum for glassy carbon in Fig. 1.7 shows a band at about 1350 cm^{-1}. The band has been known to be absent for highly crystallized graphite, for example, HOPG, and be commonly observed for disordered graphitic materials [10]. The band is thus known empirically as disorder-induced band and often called D band. Despite the fact that the presence of the D band and the intensity of this band is commonly used for practical applications to evaluate the amount of disorder in carbon material, the physical origin of the D band has been an open question for some decades. There has been an only general agreement that the band is caused by zone-edge phonons because the phonon dispersion curves [Fig. 1.6(a)] indicate that no zone-center phonons exist around 1350 cm^{-1}.

For the origin of the D band, Tuinstra and Koenig [11] proposed that the appearance of the D band was explained by considering the relaxation of the full D_{6h} symmetry for the case of finite graphite crystallites, thereby allowing many modes to show Raman activity, such as A_{1g} breathing modes in small aromatic clusters. A closely related approach, which involves the relaxation of symmetry, is the phonon density of states (DOS) model by Nemanich and Solin [9]. In this model, the band is due to the phonon DOS singularities at about 1350 cm^{-1} by phonons near M point as shown in Fig. 1.6(b) [12]. Both of the models, however, fail to give an explanation of the observed dispersion nature of the D band with excitation laser energy. Recently, Dresselhause and co-workers [13] reported

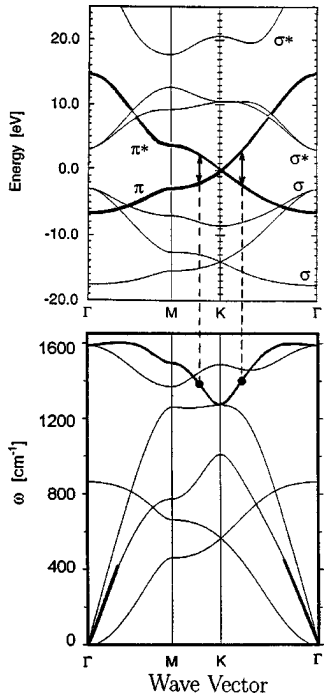

Figure 1.8: Electronic energy bands (top) and phonon dispersion curves (bottom) of 2D graphene. Both the longitudinal optic phonon branch that is strongly coupled to electronic bands in the optical excitation, and the electronic bands near the Fermi level ($E = 0$) that are linear in k are indicated by heavy lines. The slope for the transversal acoustic phonon branch is also indicated by heavy lines [13].

that the origin and dispersion of the D band can be explained in terms of a resonant Raman process by phonons near the K point of the Brillouin zone. As shown in Fig. 1.8, the longitudinal optic phonons at Δq from K point are coupled with the electrons at the same distance Δk ($= \Delta q$), which transit from π to π^* states by an resonance with the incident laser energy. The optical phonon branch, which produces the E_{2g} phonons at the Γ point, appears to be mixed with the transversal acoustic (TA) branch at the K point; this is thought to be essential to understanding the highly dispersive nature of the D band.

1.2 New Carbonaceous Materials

1.2.1 Carbonaceous nano-materials

As mentioned in the previous section, it has been believed for long time that the carbon has only three allotropes, i.e., three-dimensional diamond, quasi-two-dimensional graphite,

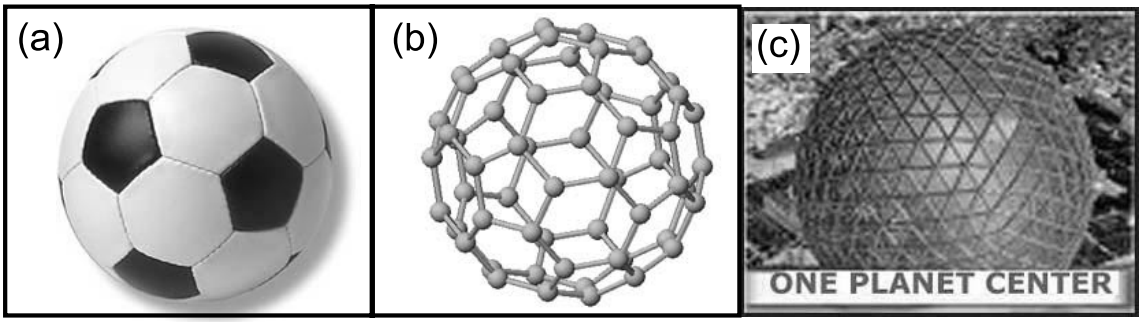

Figure 1.9: (a) Soccer ball, (b) C_{60}, and (c) a Geodesic Dome by R. Buckminster Fuller.

and one-dimensional carbyne. The era of troika has broken by the appearance of the fourth allotrope with zero-dimension. The fourth member, C_{60}, was serendipitously discovered by Kroto, Smalley, and Curl in 1985 [14]. They sought a linear carbon chain as the laboratory replica of the carbonaceous interstellar dust, and tried to create them by laser-assisted cluster beam apparatus. Under specific growth conditions, the carbon cluster consisting of sixty carbon atoms is found to be very stable. The total energy of a small number (30-100) of carbon atoms is generally reduced by eliminating dangling bonds, even at the expense of increasing the strain energy, thereby promoting the formation of closed cage molecule. Authors in Ref.[14] thus attributed the stability of C_{60} to the soccer ball structure (truncated icosahedron), where sixty carbon atoms are all equivalent and arranged in twelve pentagonal and twenty hexagonal rings, as shown in Figs.1.9(a) and 1.9(b). The molecule having such structure contains no dangling bonds and the strain associated with bending a planar array of hexagons is evenly distributed over a nuclear cage of diameter about 0.7 nm. Since the structure is very similar to the works named Geodesic Domes [Fig. 1.9(c)] by R. Buckminster Fuller, who is an American architect [15], this new member of carbon allotrope was christened buckminsterfullerene. This serendipitous discovery of the fullerene was the dawn of the new era in the history of carbon materials, opening the way to the world of carbonaceous nano-materials.

Although there were a lot of theoretical predictions, the confirmation of precise structure and properties of C_{60} had to wait their mass production enough to carry out the macroscopic measurements. This breakthrough on the fullerene research was brought by Krätschmer and Huffman in 1990 [16]. In their landmark work, they produced carbon soot by carbon evaporation in He gas atmosphere and found macroscopic quantities of C_{60} in the soot. The optical transmittance spectroscopy of the C_{60} showed four absorption peaks in infrared region. The number and position of the peaks are both consistent with the theoretically predicted ones. They also found that C_{60} fullerenes are soluble in aromatic

solvents (e.g., benzen and toluene) and C_{60} crystals, named fullerite, could be grown from the solution as the solvent evaporated. These properties were used to separate C_{60}, C_{70}, etc. molecules from the other non-soluble forms of carbon products, and to produce thin film of solvent-free fullerene crystals by sublimation. At last, nuclear magnetic resonance (NMR) study using the mass-produced C_{60} clearly demonstrated that the C_{60} actually has the soccer ball structure [17]. Since the Krätschmer and Huffman breakthrough, the fullerene has been intensively studied by physical, chemical, and mechanical techniques. This historical fact tells us that the establishment of a technique for the mass production of the materials is crucial for the development of the researches on carbonaceous nano-materials.

Since the epoch-making discovery of C_{60} [14, 16], fullerenes have attracted great interest from the view points of both science and technology. In 1991, Haddon *et al.* reported the first evidence that the fullerene solids could be doped by the alkali metals [18]. They had grown thin films of C_{60} after first attaching electrical leads to the glass substrate. When exposing the film to a flux of alkali metal atoms, they found that the resistivity dropped with exposure time, reached a minimum, then increased and ultimately saturated. The drop was thought to be owing to the electron transfer from the alkali metal dopants to the conduction bands of fullerene solids derived from the lower unoccupied molecular orbital (LUMO) of fullerenes. Among the properties of the doped fullerene solids, named fullerides, the most attention from the physics community was the appearance of superconductivity by K_3C_{60}, Rb_3C_{60}, and related fullerides. For $Rb_1Cs_2C_{60}$, a rather high superconducting transition temperature T_c reached 33 K [19]. In addition to the spacing between fullerene molecules in their solid, the central cavity of the fullerene molecule also should be a strong binding site for a wide range of atoms, leading to the formation of fullerenes with atoms captured within the closed carbon shells, called endohedral metallofullerenes. By using laser ablation technique with a target of La-impregnated low-density graphite, Heath *et al.* succeeded in producing La@C_{60} [20]. The metallofullerene suggested a "superatom" concept in which the caged atom would donate (or accept) charge from the cage, providing a positive (or negative) core. Solids derived from such species are believed to offer intriguing possibilities [21]. These fullerene-based materials show promise as the building blocks of a host of new chemical species.

1.2.2 Novel carbonaceous nano-materials

Recently, much attention has turned towards novel cage-like carbonaceous nano-materials, and intensive researches have inevitably led to the explosive evolution of the fullerene family. In 1991 [22], Iijima found the multi-walled carbon nanotubes (MWNT), consisting of graphite multi-layers wrapped into nested coaxial cylinders, in the carbon deposit

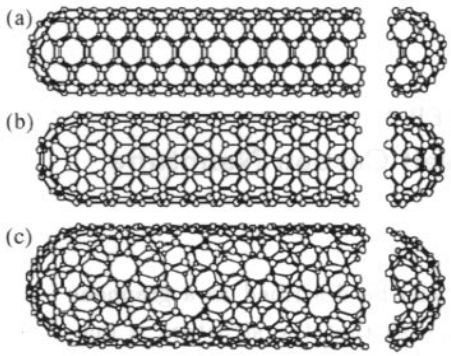

Figure 1.10: Classification of single-walled carbon nanotubes (SWNTs): (a) armchair, (b) zigzag, and (c) chiral SWNTs [2].

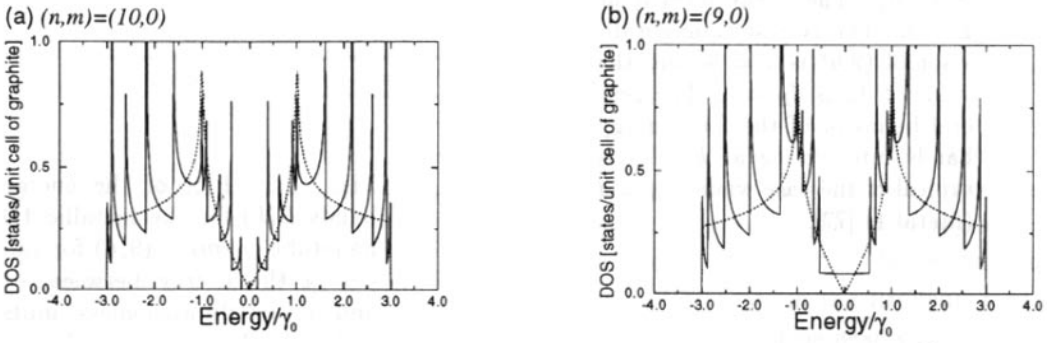

Figure 1.11: Electron 1D density of states per unit cell of 2D graphene sheet for two $(n, 0)$ zigzag single-walled nanotubes (SWNTs): (a) the $(10, 0)$ SWNT which has semiconducting behavior, (b) the $(9, 0)$ SWNT which has metallic behavior [2]. Also shown in the figure is the density of states for the 2D graphene sheet.

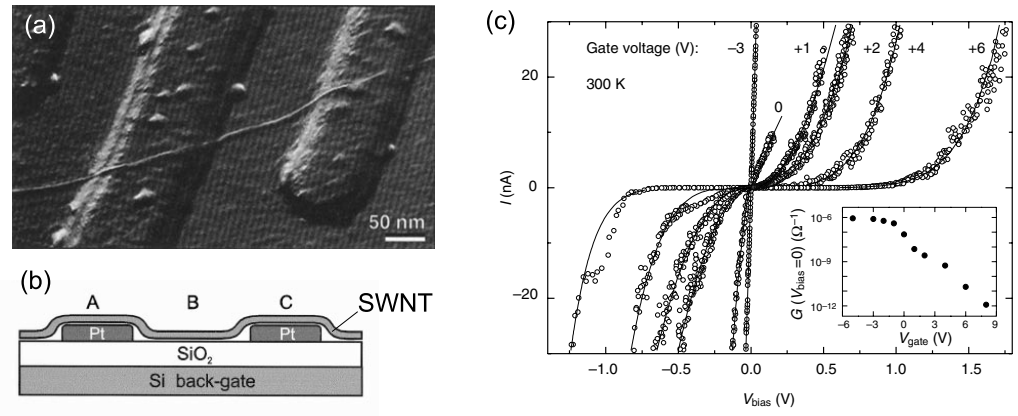

Figure 1.12: (a)Atomic force microscopic image of a metallic single-walled carbon nanotube (SWNT) on top of a Si/SiO_2 substrate with two 15-nm-thick Pt electrodes [27]. The individual metallic SWNTs can act as quantum wires at low temperature. (b) Schematic side view of the single carbon nanotube field-effect transistor [28]. A single semiconducting SWNT is contacted by two electrodes. The Si substrate, which is covered by a layer of SiO_2 300 nm thick, acts as a back-gate. (c) Two probe $I - V_{bias}$ curves for various values of the gate voltage (V_{gate}).

formed by an arc discharge. In addition to the MWNT, the synthesis of single-walled carbon nanotubes (SWNT) with seamless single cylinder [23, 24] and ropes of closed-packed SWNTs [25] were reported. The structural images of several SWNTs are shown in Fig. 1.10. The pace of research on SWNT has been particularly accelerated by the findings of the extraordinary electrical transport properties of SWNTs. Their longitudial conductivity is very sensitive to the detailed atomic structure and their diameter; a slight change of the diameter can result in the SWNT being either metallic or semiconducting along its length (Fig. 1.11) [2]. In addition, isolated SWNTs are expected to show high thermal conductivity as high-purity diamond, which is one of the best thermal conductors [26]. Such unusual behaviors of SWNT bring about the birth of the much talked-about nano-electronics and make SWNTs play an important roles at the cutting edge of nano-technology. As shown in Fig. 1.12, Dekker and co-workers have indeed demonstrated that the individual metallic SWNTs can act as quantum wires at extremely low temperature [27], and a room-temperature transistor can be fabricated using a single semiconducting SWNT [28].

Following the nanotubes, carbon onions [29] and carbon nanocapsules [30, 31], which are focused in this thesis, have been discovered as novel carbonaceous nano-materials in the next generation. Additionally, there are a lot of reports regarding the creation of novel carbonaceous nano-materials, e.g., single-walled carbon nanohorn [32], SWNTs en-

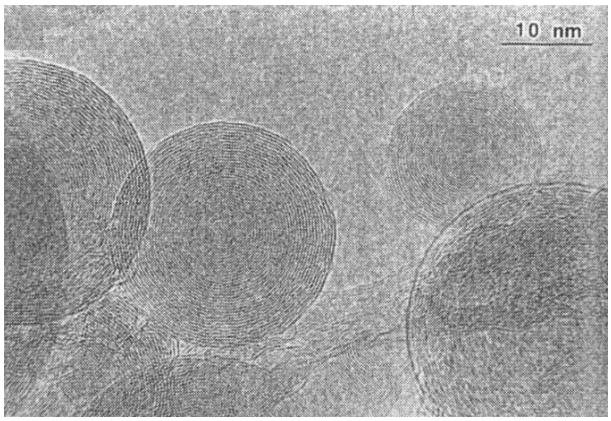

Figure 1.13: Carbon onions first reported by Ugarte [29].

capsulating fullerenes or metallofullerene (carbon peapods) [33], shortened multi-walled nanotube strucutres encapsulating fullerenes (bucky shuttle) [34]. These novel carbonaceous nano-materials including carbon onions and nanocapsules are expected as the key-elements in the century of nano-science and nano-technology.

1.3 Carbon Onions

1.3.1 Historical perspective of carbon onions

The carbon onion, which is one of the new members of the fullerene family, consists of concentric curved graphitic sheets. The formation of carbon onions was first reported by Ugarte [29]. He observed that carbon soot particles and tubular graphitic structure are transformed into quasi-spherical carbon onions by intense electron-beam irradiation in a transmission electron microscope (TEM) as shown in Fig. 1.13. The driving force of the transformation was considered to be a collision between irradiated electrons and carbon atoms, so called "knock-on effects". The elimination of dangling bonds in the onions was believed to lead to their quasi-perfect spherical shapes [35].

Banhart and Ajayan [36] reported that the further bombardment of the onions with high-dose electrons at elevated temperature in a TEM induces the graphite-diamond transformation in the center of the carbon onions. Since the high pressure is needed to transform graphite into diamond, the onions are considered to act as nanoscopic pressure cells. Moreover, the onions are expected to be potentially good solid lubricant as it is the case for WS_2 nanoparticle having an onion-like structure [37]. In order to seek further possibilities for potential applications of onions in the technological field, macroscopic experiments on

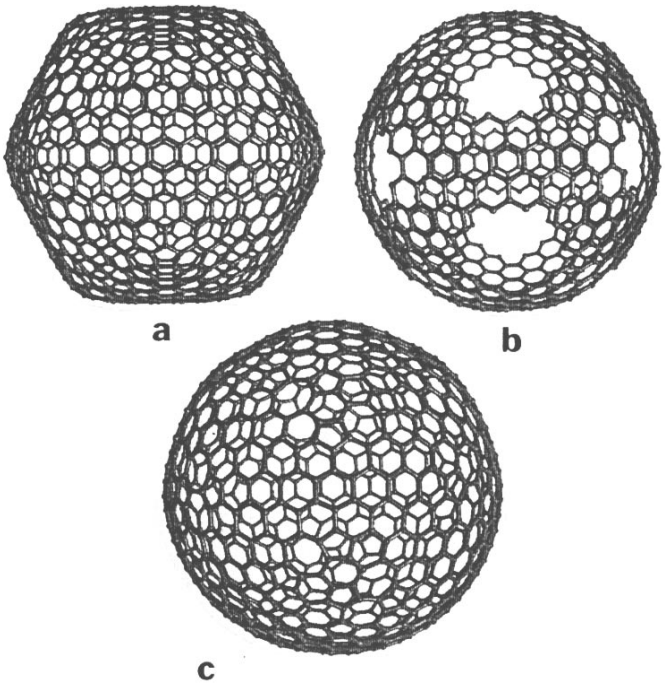

Figure 1.14: a: Icosahedral C_{960} with facets. b: Relaxed C_{720} with holes in the pentagonal rings (obtained from C_{960}). c: C_{888} quasi-spherical shell with the holes filled by heptagonal and pentagonal rings [40].

the onions to reveal their fundamental properties have been indispensable.

In particular, it is still unclear why onion structures are highly spherical and how the graphitic carbon atoms rearrange in order to attain sphericity [38, 39, 40, 41, 42]. It was initially suggested that the onions were nested fullerenes consisting of graphitic cages, which contain only pentagonal and hexagonal carbon rings as illustrated in Fig.1.14a [43]. In this model, the onion structures exhibit facets if not oriented along the five-fold axes and the facets are more pronounced for bigger onions. Although Terrones and Terrones [41], based on theoretical considerations, showed that the sphericity is improved by introducing heptagons and additional pentagons, so-called Stone-Wales defects, into the carbon networks as shown in Fig. 1.15B, this model illustrated in Fig. 1.14c has not yet been experimentally verified. The structure of spherical onions has not yet been clarified whether they consist of fullerene-like perfect shells made of only pentagonal, hexagonal, and heptagonal carbon rings (Fig. 1.14c) or more defective structures with a large number of defects or holes (Fig. 1.14b). Electronic and optical properties of the onions that are deeply related with their structure has been also open questions. Nevertheless, detailed experimental studies of structure and physical properties of the onions have been prevented by the difficulty in the mass production of the onions in

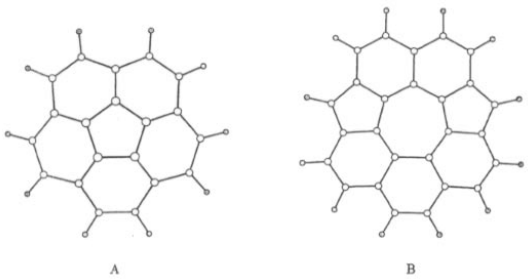

Figure 1.15: A: Pentagon in hexagonal network. B: 5-7-5 Stone-Wales defect in hexagonal network [42].

uniform morphology and size [44].

So far, only a few methods have been reported to prepare carbon onions in a large quantity. These are high temperature annealing of amorphous carbon soot [45], high-dose carbon ion implantation into metal substrate [46], and high temperature annealing of diamond nanoparticles [48]. The first method was reported by de Heer and co-workers [45]. Since they used amorphous carbon soot, which is formed by an arc discharge method and thus not so uniform in the size, as starting materials, it is difficult to prepare uniform-sized onions. Cabioc'h and his co-workers [46] have developed the second method. By implanting carbon ions into Ag substrates at elevated temperatures, they succeeded in preparing thin films consisting of spherical carbon onions. Very recently they reported the fabrication of carbon onion thin films on quartz substrates [47]. In the ion-implantation method, the formation of polyhedral onions with facets is difficult because of the irradiation environments.

In contrast to the previous two techniques, the last one first reported by Kuznetsov *et al.* [48] has several advantages. One of them is that carbon onions in uniform size can be prepared mainly owing to the formation mechanism; since one nanodiamond is transformed into one onion from the surface to the center, the onions in uniform size can be obtained by using initial diamond nanoparticles with narrow size distribution. Another advantage is that the morphology of the onions can be varied from spherical to polyhedral by controlling the annealing condition [49]. Therefore, the carbon onions prepared from diamond nanoparticles enable us to carry out a systematic experimental study of the onions that gives deeper insight into their fundamental properties including structure, electronic and optical properties.

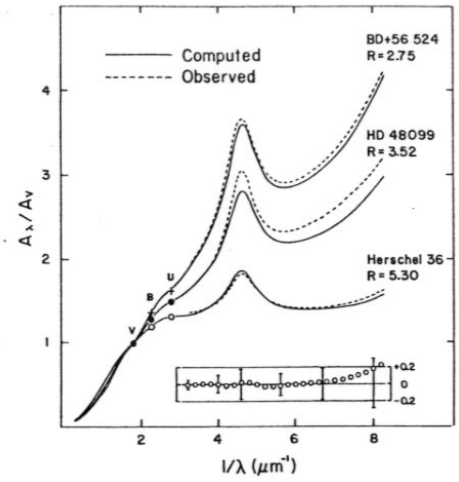

Figure 1.16: Interstellar extinction curves along different lines of sight [54].

1.3.2 Carbon onions in astrophysics

As well as in the material science, carbon onions have been a subject of interest in astronomy and astrophysics [50, 51, 52]. The astronomical observation has established an optical extinction bump with almost constant position at 217.5 nm (4.6 μm^{-1}, 5.7 eV), coexisting with a variation of the width by more than 30 % along different lines of sight (Fig. 1.16) [53, 54]. The bump in the interstellar extinction curves is believed to originate from carbonaceous dust in the interstellar space [54]. It is well known that this astronomical interests led to the serendipitous discovery of C_{60} [14] as already described. Many sophisticated models of the dust particles have already been constructed to explain the 4.6 μm^{-1} interstellar feature; e.g., graphitic particles with a size distribution [55], a mixture of sphere composed of graphite, amorphous carbon, and silicate [56, 57], irregular or fractal arrangement of graphite and amorphous carbon [58, 59], polycyclic aromatic hydrocarbon [60], and natural coal [61]. However, these models failed to reproduce the large variation in the resonance width while maintaining a constant energy of the absorption peak.

Carbon onions are proposed as alternative possible candidates for the carbonaceous dust particles giving rise to the interstellar feature at 4.6 μm^{-1}. Detailed theoretical considerations has already been performed by Lucas and co-workers [51, 52]. They predicted that a water-coated spherical carbon onion with diamond core successfully reproduced an absorption peak around 4.6 μm^{-1} and the decorrelation between the peak position and the width [52]. This onion model, however, still contained several discrepancies; owing to the water coating, the width of the onion resonance is larger than that of the observational data and an additional absorption peak around 7 μm^{-1} that has not been confirmed by

observation emerges.

In laboratory experiments, the pioneering work by de Heer and Ugarte [62] showed that water suspensions of polyhedral onions, which are prepared by annealing carbon soot, exhibit an extinction peak at 3.8 μm^{-1}. The heavy red shift from 4.6 μm^{-1} was tentatively explained by the water environment and clustering effect. Recently, Wada *et al.* [63] reported that the carbonaceous material containing onion-like carbon nanoparticles was found in the ejecta of methan plasma, in a laboratory analog for the mass ejection from the stellar atmosphere. Although the material exhibited an absorption peak around 4.6 μm^{-1}, it is composed of not only the onions but also organic components. To our knowledge, extinction properties of carbon onions based on the laboratory experiments have not well explained the contribution of the onions to the interstellar absorption bump. The ambiguity is largely because of the difficulty in the mass production of the uniform-sized and -shaped onions to carry out the macroscopic optical measurements. In addition, lacking is the successful interpretation of the experimental results by theoretical considerations based on the constructed onion model. In this astronomical context, both the experimental and theoretical studies on the optical properties of the well-defined carbon onions are highly desired to give a clearcut explanation for this long-standing important problem in astronomy and astrophysics.

1.4 Carbon Nanocapsule Systems

1.4.1 Magnetic-metal filled carbon nanocapsules

Metal nanoparticles wrapped in concentric layers of encapsulating graphitic carbon, called metal filled carbon nanocapsules, have been intensively studied since LaC_2 was successfully encapsulated as shown in Fig. 1.17 [30, 31]. In particular for magnetic-metal filled carbon nanocapsules, the interesting magnetic behavior of magnetic-metal nanoparticles and the oxidation resistance of the carbon coating have led to the consideration of these particles for applications in areas such as magnetic data storage, magnetic tonor for xerography, fellofluids, and contrast agents in magnetic resonance imaging [64]. For magnetic recording media, graphitic coating increases the effective distance of neighboring magnetic particles [65]. The increase reduces particle-particles exchange coupling, which is an important issue in ongoing attempt to synthesize extremely high-density magnetic recording media [66, 67, 68]. In order to realize ultra-high-density magnetic recording media of the next generation, a system consisting of size-controlled magnetic nanoparticles isolated by thickness-controlled non-magnetic phases is indispensable [69].

Magnetic-metal filled carbon nanocapsules have been produced by various methods via vapor phase reaction, e.g., standard arc methods [70, 71] and modified arc methods

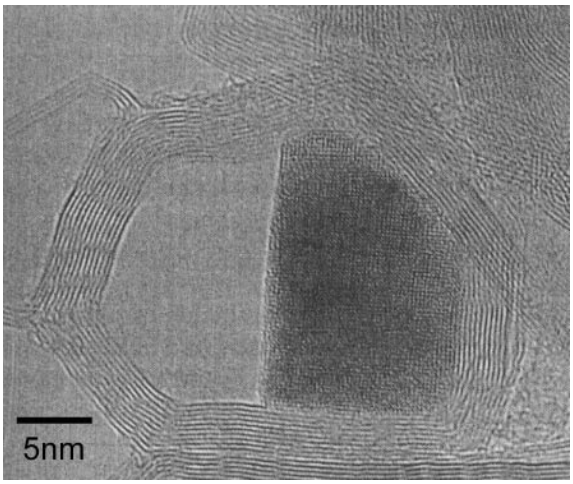

Figure 1.17: Carbon nanocapsule encapsulating LaC_2 reported by M. Tomita *et al.* [31].

[65, 72]. The nanocapsules are thought to be formed by so-called "dissolution-precipitation mechanism", in which carbon is dissolved into the metal, and then graphite precipitates as coating layers on quenching. Jiao and Seraphin [73] showed that, for the nanocapsules prepared by the modified arc discharge, the thickness of the coating increases by post annealing. They claimed that the addition of graphitic layers results from a precipitation of carbon previously dissolved in the metal, suggesting the dissolution-precipitation mechanism in these systems.

In contrast to vapor phase reaction, few method to produce carbon nanocapsules via solid state reaction has been reported so far. Fabrication via solid state reaction is expected to enable us to achieve larger yield than vapor phase reaction. Harris *et al.* [74] recently succeeded in producing carbon nanocapsules by annealing microporous carbons which had been impregnated with the material to be encapsulated. In this method, however, it is difficult to control the thickness of the coating layers. Fabrication method of size-controlled carbon nanocapsules with thickness-controlled graphitic coating via solid state reaction is required to open the way to the potential applications of filled carbon nanocapsules.

1.4.2 Filled carbon nanocapsule thin fillms

The march of areal density in magnetic recording media has continued at a pace of one order of magnitude per decade till 1990 and at a more explosive pace in the last decade (Fig. 1.18) [75]. In order to attempt the application of carbon nanocapsules to magnetic recording media, it is important to develop thin films composed of filled carbon nanocap-

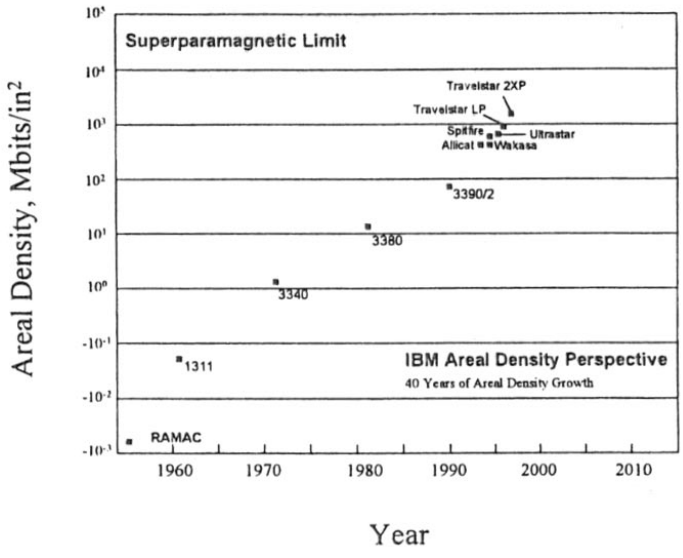

Figure 1.18: The increase in magnetic storage density of IBM disk drives with time [75].

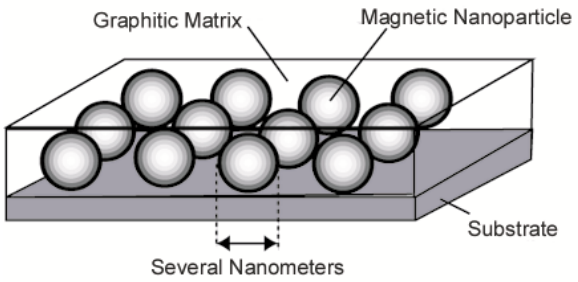

Figure 1.19: A schematic image of the M-C nanogranular thin film.

sules, so-called nanogranular thin films. In particular, nanogranular thin films consisting of iron-group metal nanoparticles several nanometers in diameter separated by graphitic matrices (M-C nanogranular thin films) as shown in Fig. 1.19 are proposed as a possible candidate for realizing magnetic recording media with an ultra-high areal density ($\sim$ 100 Gb/in^2) [67, 76, 77].

In the M-C nanogranular films, the magnetic metal particles are sufficiently small to possess a magnetic single-domain structure. These particles are expected to exhibit high coercivities because the simultaneous switching of polarity takes places only by coherent rotation of the moments against strong anisotropy force. Moreover, owing to the immiscibility of carbon with the metals, the nanoparticles are separated by thin graphitic

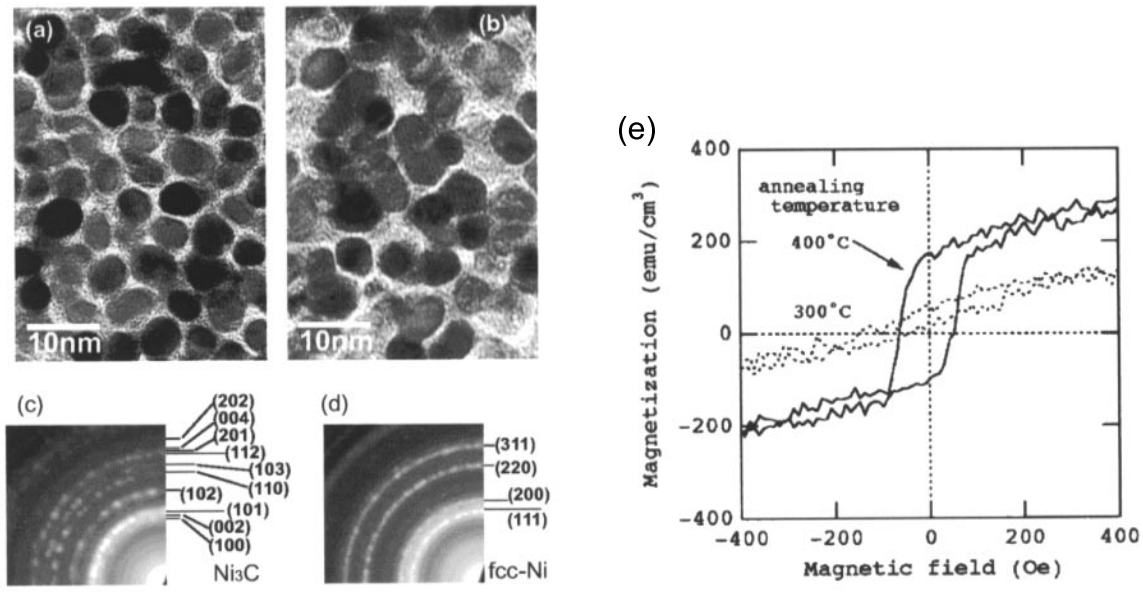

Figure 1.20: Typical TEM images for Ni-C composite thin films annealed at (a) 300 °C and (b) 400 °C, and corresponding SAED patterns [(c) and (d)], respectively. (e) *M-H* curves for Ni-C composite thin films prepared at two different annealing temperatures [80].

carbon layers in the case of low carbon concentration in the film. The separation leads to a reduction of the noise via a decrease in particle-particle exchange coupling as already mentioned [78]. The carbon matrices have another advantage in the fabrication process of thin film media. Carbon has been used for overcoats of the practical media because of their superb wear resistance and surface smoothness By using carbon as an intergranule material, the fabrication processes of the recording layer and overcoat can be integrated [79]. The M-C nanogranular thin film is thus a promising material for the ultra-high density recording media.

Recently, we have succeeded in preparing Ni-C nanogranular thin films using co-sputtering method together with post-annealing [80]. In Ni-C nanogranular thin films, Ni nanoparticles were about 5.6 nm in average diameter with a narrow size distribution [Fig. 1.20(b)]. However, the coercivity of the film was not sufficiently high ($\sim$ 50 Oe) as shown in Fig. 1.20(e). The low coercivity of the film is one of the drawbacks in the application for recording media. In order to remove the drawback, an improvement of the magnetic properties is required. In addition to the applied physical context, the formation mechanism and magnetic properties of such nanogranular thin films are also of great interests from the viewpoints of fundamental physics of magnetic nanoparticle systems.

1.5 Chapter Overview and Goals of This Thesis

1.5.1 Structure and physical properties of carbon onions

The goal of the first part of this thesis is to reveal structures and physical properties of carbon onions. Spherical and polyhedral carbon onions in macroscopic quantities are prepared by annealing diamond nanoparticles. In Chapter 2, the carbon onions are investigated by high-resolution transmission electron microscopy (HRTEM), Raman spectroscopy, electron energy-loss spectroscopy (EELS), and electron spin resonance (ESR). The author shows the annealing temperature dependences of the structure and electronic properties of carbon onions. Several deeper insights into the correlation between structure and electronic states of carbon onions are given. As a results, the author will propose a new structural model of the onions (a defective spherical onion model). In Chapter 3, in order to address further the structure and formation mechanism of the carbon onions, the synchrotron X-ray diffraction (XRD) studies on a series of the onion samples are carried out. Chapter 4 is devoted to the experimental and theoretical studies on optical extinction properties of the carbon onions. The author shows experimental extinction spectra of spherical onions can be interpreted well by the theoretical considerations for the aggregate of defective spherical onions. On the other hands, the experimental spectrum for polyhedral onions is explained by the aggregate of anisotropic graphite ellipsoids. Furthermore,

the defective spherical onions model reproduces the interstellar extinction feature at 4.6 μm^{-1}, suggesting that isolated defective spherical carbon onion is a likely candidate for the carbonaceous interstellar dust particles giving rise to the extinction feature.

1.5.2 Fabrication and physical properties of filled carbon nanocapsule systems

The goal of the second part is to develop the fabrication technique of filled carbon nanocapsules systems and study their formation mechanism and properties. Chapter 5 covers a new and simple method for synthesizing Co, Ni, and Fe filled carbon nanocapsules via solid state reaction. The author intends to clarify the formation mechanism of Co filled carbon nanocapsules by *in-situ* TEM, conventional XRD, and Raman spectroscopy. Finally a novel formation mechanism of the filled carbon nanocapsules will be proposed. In Chapter 6, the formation technique of thin films composed of magnetic-metal filled carbon nanocapsules, named magnetic-metal carbon nanogranular thin films, will be developed. The formation mechanism and magnetic properties of the thin films are studied. The author will show several important findings for realizing the thin films with a high coercivity.

References

[1] A. M. Rao and M. S. Dresselhaus, in *Nanostructured Carbon for Advanced Applcations*, edited by G. Benedek, P. Milani, and V. G. Ralchenko (Kluwer Academic Publishers, Dordrcht, 2001).

[2] R. Saito, G. Dresselhaus, and M. S. Dresselhaus, *Physical Properties of Carbon Nanotubes* (Imperial College Press, London, 1998).

[3] J. Robertson, Advance in Physics **35**, 317 (1986).

[4] M. S. Dresselhaus, G. Dresselhaus, K. Sugihara, I. L. Spain, and H. A. Goldberg, *Graphite Fibers and Filaments,* Springer Series in Material Sciences, Vol. 5 (Springer-Verlag, Berlin, 1988).

[5] J.-C. Charlier, X. Gonze, and J.-P. Michenaud, Phys. Rev. B **43**, 4579 (1991).

[6] I. L. Spain, *Chemistry and Physics of Carbon*, edited by P. L. Walker Jr., and P. A. Thrower (Marcel Dekker, N.Y., 1980).

[7] M. S. Dresselhaus and G. Dresselhaus, *Light Scattering in Solids III*, edited by M. Cardona and G. Güntherodt (Springer-Verlag, Berlin, 1982).

[8] M. Maeda, Y. Kuramoto, and C. Horie, J. Phys. Soc. Japan **47**, 337 (1979).

[9] R. J. Nemanich and S. A. Solin, Phys. Rev. B **20**, 392 (1979).

[10] D. S. Knight and W. B. White, J. Mater. Res. **4**, 385 (1989).

[11] F. Tuinstra and J. L. Koenig, J. Chem. Phys. **53**, 1126 (1970).

[12] S. Y. Leung, M. S. Dresselhaus, and G. Dresselhaus, Physica B **105**, 375 (1981).

[13] M. J. Matthews, M. A. Pimenta, G. Dresselhaus, M. S. Dresselhaus, and M. Endo, Phys. Rev. B **59**, R6585 (1999).

[14] H. W. Kroto, J. R. Heath, S. C. O'Brien, R. F. Curl, and R. E. Smalley, Nature **318**, 162 (1985).

[15] The World Wide Web site of Buckminster Fuller Institute, U.S.A. (http://www.bfi.org/index.html).

[16] W. Krätschmer, L. D. Lamb, K. Fostiropoulos, and D. R. Huffman, Nature **347**, 354 (1990).

[17] R. Taylor, J. P. Hare, A. K. Abdul-Sada, and H. W. Kroto, J. Chem. Soc., Chem. Comm. 1423 (1990).

[18] R. C. Haddon, *et al.*, Nature **350**, 320 (1991).

[19] K. Tanigaki, T. W. Ebbesen, S. Saito, J. Mizuki, T. S. Tsai, Y. Kubo, and S. Kuroshima, Nature **352**, 222 (1991).

[20] J. R. Heath, S. C. O'Brien, Q. Zhang, Y. Liu, R. F. Curl, H. W. Kroto, and R. E. Smalley, J. Am. Chem. Soc. **107**, 7779 (1985).

[21] J. H. Weaver and D. M. Poirier, in *Solid Sate Physics* **48**, edited by H. Ehrenreich and F. Spaepen (Academic Press, San Diego, 1994).

[22] S. Iijima, Nature **354**, 56 (1991).

[23] S. Iijima and T. Ichihashi, Nature **363**, 603 (1993).

[24] D. S. Bethune, C. H. Kiang, M. S. de Vries, G. Gorman, R. Savy, J. Vazquez, and R. Beyers, Nature **363**, 605 (1993).

[25] T. Guo, C.-M. Jin, and R. E. Smalley, Chem. Phys. Lett. **243**, 49 (1995).

[26] S. Berber, Y.-K. Kwon, and D. Tomanek, Phys. Rev. Lett. **84**, 4613 (2000).

[27] S. J. Tans, M. H. Devoret, H. Dai, A. Thess, R. E. Smalley, L. J. Geerlings, and C. Dekker, Nature **386**, 474 (1997).

[28] S. J. Tans, A. R. M. Verschueren, and C. Dekker, Nature **393**, 49 (1998).

[29] D. Ugate, Nature **359**, 707 (1992).

[30] R. S. Ruoff, D. C. Lorents, B. Chan, R. Malhotra, and S. Subramoney, Science **259**, 346 (1993).

[31] M. Tomita, Y. Saito, and T. Hayashi, Jpn. J. Appl. Phys. **32**, L280 (1993).

[32] S. Iijima, M. Yudasaka, R. Yamada, S. Bandow, K. Suenaga, F. Kokai, and K. Takahashi, Chem. Phys. Lett. **309**, 165 (1999).

[33] B. W. Smith, M. Monthioux, and D. E. Luzzi, Nature **396**, 323 (1998).

[34] Y-K. Kwon, D. Tománek, and S. Iijima, Phys. Rev. Lett. **82**, 1470 (1999).

[35] D. Tomanek, W. Zhang, and E. Krastev, Phys. Rev. B **48**, 15461 (1993).

[36] F. Banhart and P. M. Ajayan, Nature **382**, 433 (1996).

[37] L. Rapoport, F. Yu. Bilik, M. Homyonfer, S. R. Cohen, and R. Tenne, Nature **387**, 791 (1997).

[38] A. Maiti, C. J. Brabec, and J. Bernholc, Modern Phys. Lett. B **7**, 1883 (1993).

[39] J. P. Lu and W. Yang, Phys. Rev. B **49**, 11421 (1994).

[40] H. Terrones and M. Terrones, Fullerene Science & Technology **4**, 517 (1996).

[41] H. Terrones and M. Terrones, J. Phys. Chem. Solids **58**, 1789 (1997).

[42] K. R. Bates and G. E. Scuseria, Theor. Chem. Acc. **99**, 29 (1998).

[43] H. W. Kroto and K. Mckay, Nature **331**, 328 (1988).

[44] D. Ugarte, Carbon **33**, 989 (1995).

[45] W. S. Bacsa, W. A. de Heer, D. Ugarte, and A. Châtelain, Chem. Phys. Lett. **211**, 346 (1993).

[46] T. Cabioc'h, J. P. Riviere, and J. Delafond, J. Mater. Sci. **30**, 4787 (1995).

[47] T. Cabioc'h, E. Thune, and M. Jaouen, Chem. Phys. Lett. **320**, 202 (2000).

[48] V. L. Kuznetsov, A. L. Chuvilin, Y. V. Butenko, I. Y. Mal'kov, and V. M. Titov, Chem. Phys. Lett. **222**, 343 (1994).

[49] E. D. Obraztsova, M. Fujii, S. Hayashi, V. L. Kuznetsov, Yu. V. Butenko, and A. L. Chuvilin, Carbon **36**, 821 (1998).

[50] P. Appel, D. Östling, and G. Mukhopadhyay, Solid State Commun. **87**, 219 (1993).

[51] A. A. Lucas, L. Henrard, and Ph. Lambin, Phys. Rev. B **49**, 2888 (1994).

[52] L. Henrard, Ph. Lambin, and A. A. Lucas, Astrophys. J. **487**, 719 (1997).

[53] E. L. Fitzpatrick and D. Massa, Astrophys. J. Suppl. **72**, 163 (1990).

[54] J. S. Mathis, Annu. Rev. Astron. Astrophys. **28**, 37 (1990).

[55] J. S. Mathis, W. Rumpl, and K. H. Nordsiek, Astrophys. J. **217**, 425 (1977).

[56] P. A. Aannestad, Astrophys. J. **443**, 653 (1995).

[57] J. S. Mathis and G. Whiffen, Astrophys. J. **341**, 808 (1989).

[58] J. -M. Perrin and J.-P. Sivan, Astron. Astrophys. **247**, 497 (1991).

[59] E. L. Wright, Astrophys. J. **320**, 818 (1987).

[60] W. Lee and T. J. Wdoviak, Astrophys. J. **410**, L127 (1993).

[61] R. Papoular, J. Conard, O. Guillois, I. Nenner, C. Reynaud, and J. -N. Rouzaud, Astron. Astrophys. **315**, 222 (1996).

[62] W. A. de Heer and D. Ugarte, Chem. Phys. Lett. **207**, 480 (1993).

[63] S. Wada, C. Kaito, S. Kimura, H. Ono, and A. T. Tokunaga, Astron. Astrophys. **345**, 259 (1999).

[64] J. H. J. Scott and S. A. Majetich, Phys. Rev. B **52**, 12564 (1995).

[65] J. J. Host, J. A. Block, K. Parvin, V. P. Dravid, J. L. Alpers, T. Sezen, and R. LaDuca, J. Appl. Phys. **83**, 793 (1998).

[66] T. Yogi and T. Nguyen, IEEE Trans. Magn. **29**, 307 (1993).

[67] J. -J. Delaunay, T. Hayashi, M. Tomita, S. Hirono, and S. Umemura, Appl. Phys. Lett. **71**, 3427 (1997).

[68] M. Yu, Y. Liu, A. Moser, D. Weller, and D. J. Sellmyer, Appl. Phys. Lett. **75**, 3992 (1999).

[69] E. S. Murdock, R. F. Simmons, and R. Davidson, IEEE Trans. Magn. **28**, 3078 (1992).

[70] M. E. McHenry, S. A. Majetich, J. O. Artman, M. DeGraef, and S. W. Staley, Phys. Rev. B **49**, 11358 (1994).

[71] Y. Saito, T. Yoshikawa, M. Okuda, N. Fujimoto, S. Yamamoto, K. Wakoh, K. Sumiyama, K. Suzuki, and A. Kasuya, J. Appl. Phys. **75**, 134 (1994).

[72] J. Jiao, S. Seraphin, X. Wang, and J. C. Withers, J. Appl. Phys. **80**, 103 (1996).

[73] J. Jiao and S. Seraphin, J. Appl. Phys. **83**, 2442 (1998).

[74] P. J. F. Harris and S. C. Tsang, Chem. Phys. Lett. **293**, 53 (1998).

[75] P. J. Grundy, J. Phys. D: Appl. Phys. **31**, 2975 (1998).

[76] T. J. Konno, K. Shoji, K. Sumiyama, and K. Suzuki, J. Magn. and Magn. Mater. **195**, 9 (1999).

[77] H. Zeng, M. L. Yan, Y. Liu, and D. J. Sellmyer, J. Appl. Phys. **89**, 810 (2001).

[78] K. E. Johnson, C. M. Mate, J. A. Merz, R. L. White, and A. W. Wu, IBM J. Res. Develop. **40**, 511 (1996).

[79] T. Hayashi, S. Hirono, M. Tomita, and S. Umemura, Nature **381**, 772 (1996).

[80] O. Mamezaki, H. Adachi, S. Tomita, M. Fujii, and S. Hayashi, Jpn. J. Appl. Phys. **39**, 6680 (2000).

Part I

Structure and Physical Properties of Carbon Onions

Chapter 2

Electronic States of Carbon Onions

2.1 Introduction

As mentioned in the previous chapter, the electronic states of carbon onions have been unclear mainly because of the difficulty in preparing the onions enough to study by macroscopic investigation technique. In this chapter, spherical and polyhedral carbon onions are prepared from diamond nanoparticles and investigated by high-resolution transmission electron microscopy (HRTEM), Raman spectroscopy, electron energy-loss spectroscopy (EELS), and electron spin resonance (ESR).

The EELS combined with transmission electron microscope is a strong tool for the analysis of electronic states in nanosize particles. Especially, the energy-loss near-edge structure (ELNES) in the core-loss spectrum is directly correlated to the density of the unoccupied conduction band states [1]. The shape of the ELNES thus contains useful information about the nearest neighbor environment of atoms in covalent bonding. Although Cabioc'h *et al.* [2] studied the EELS of carbon thin films containing onions prepared by the carbon ion implantation method, they showed only the low-loss spectra of onions; the core-loss spectra have not been reported.

ESR is also a powerful technique to study the microstructure and the electronic properties of carbon-related materials. Recently, Andersson *et al.* [3] studied the structure and electronic states of faceted polyhedral carbon onions by ESR. They concentrated their attention on providing evidence of a considerable enhancement in the density of states at the Fermi energy (edge state) [4]. However, no attention has been paid on the spherical onion, which is considered to be an intermediate state in the transformation from a diamond nanoparticle into a polyhedral onion. Little is thus known about the correlation between the structure and electronic states of carbon onions.

We will demonstrate here the annealing temperature dependences of the structure and electronic states of carbon onions. As the annealing temperature increases diamond

nanoparticles are transformed into spherical onions and finally into polyhedral onions. It was found by EELS measurements that the core-loss spectrum of spherical carbon onions was similar to that of nc-D, although the low-loss spectrum and the high-resolution transmission electron microscopic observation suggest the formation of graphitic sp^2 network. The feature in the core-loss spectrum indicates that spherical onions have a number of sp^3 bonds in themselves. ESR spectra for spherical onions show a presence of narrow signal corresponding to the dangling bond spins and an absence of additional broad signal corresponding to conduction π electron spins. The π electrons in spherical onions are thus localized in small domains of sp^2 graphitic sheets, and do not act as conduction electrons. Our findings strongly suggest that the structure of spherical onions is far from the perfectly closed graphitic shells. On the contrary, in polyhedral onions, ESR studies indicates that conduction π electrons are generated. Polyhedral onions have ordered graphitic structure, and thus π electrons in them can act as conduction electrons. The present study clarifies the mechanism of transformation from diamond nanoparticles into carbon onions, and gives deeper insight into the correlation between the structure and electronic states of carbon onions.

2.2 Experimental Procedure

Carbon onions were prepared by the annealing of diamond nanoparticles about 5 nm in diameter [5]. Initial diamond nanoparticles are commercially available. For TEM, Raman and ESR studies, about 20 mg of nanoparticles were stuffed into a hole (2.5 mm in diameter) which was drilled through the center of a graphite rod (5 mm in diameter and 7 mm in length). The graphite rod was then annealed by an electron beam irradiation in vacuum ($< 2.5\times10^{-3}$ Pa). Annealing took place for 30 min at the temperatures ranging from 700 to 2200 °C. For EELS studies, diamond nanoparticles were put onto a tungsten boat and resistively heated in vacuum ($< 10^{-2}$ Pa). Annealing was carried out at different temperatures ranging from 1700 to 2000 °C. The annealing temperatures were monitored by a radiative pyrometer [TR-630 (MINOLTA)].

HRTEM studies were performed with a JEOL JEM-2010 electron microscope operated at 200 kV. Samples were dispersed in ethanol and placed on holey carbon thin films supported by copper grids. In the EELS study, a Gatan parallel EELS system (model 666) mounted with the electron microscope was used. The energy resolution of the system was 1.0 eV (FWHM of zero-loss peak) and the maximum dispersion was 0.05 eV per channel. In all studies, the spectra were acquired from the areas of 25 nm in the specimens. All of the energy-loss spectra were carefully measured from the specimens which were suspended across the hole of holey carbon films. Thus the spectra were not affected by supporting

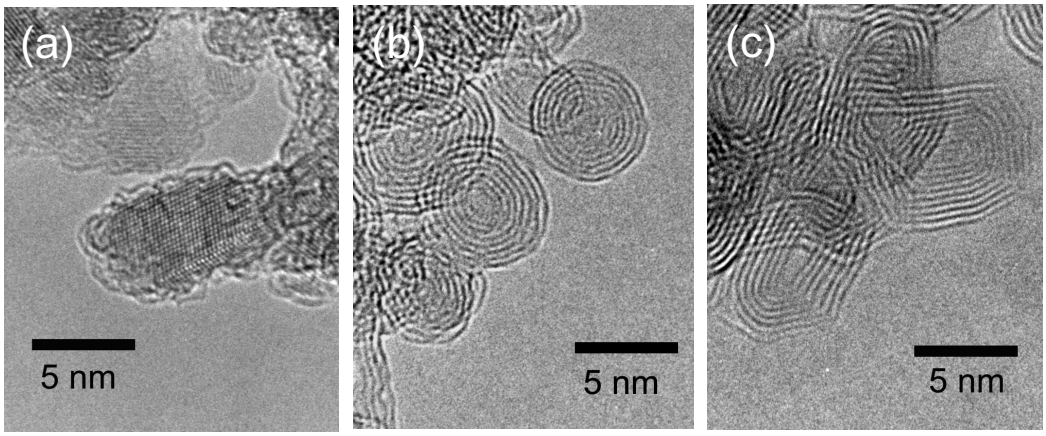

Figure 2.1: HRTEM images of (a) diamond nanoparticles, (b) spherical carbon onions and (c) polyhedral carbon onions. Diamond nanoparticles are transformed into spherical onions at about 1700 °C. Polyhedral onions are dominant in the sample annealed above 1900 °C.

carbon films.

For Raman measurements, samples were put into holes which were drilled in Al blocks. Raman spectra were recorded in a back-scattering configuration at room temperature by using a JOBIN YVON U1000 double monochromator equipped with a Hamamatsu Photonics R943-02 photomultiplier and a photon-counting system. The excitation source was a 457.9 nm line of an Ar-ion laser. The laser power was kept less than 20 mW in order to avoid the local heating. All Raman spectra were analyzed by fitting the spectra to Lorentzian line shapes.

ESR studies were carried out with a conventional X-band spectrometer [EMX EPR system (Bruker)]. Samples of 5-20 mg were put into a quartz glass tube and placed in the cavity. The magnetic field and the microwave frequency during the measurements were calibrated using a nuclear magnetic resonance gaussmeter and a frequency counter, respectively. The intensity of the ESR signal from the sample was normalized by that from $CuSO_4 \cdot 5H_2O$ as reference and by the weight of the sample.

2.3 Results

2.3.1 Transmission electron microscopy

The starting material in the present study is diamond nanoparticles with average diameter of 5 nm as shown in Fig. 2.1(a). We can observe lattice fringes corresponding to the {111} planes of diamond. Figure 2.1(a) also shows amorphous carbon layers on the surfaces of

diamonds. Previously, we reported that the annealing at temperatures up to 800 °C does not noticeably affect the structure and size of the diamond nanoparticles [6].

After annealing at about 1700 °C, spherical carbon onions around 5 nm in diameter [Fig. 2.1(b)] can be seen. Unwanted carbon formations such as amorphous carbon particles have not been observed. The result suggests that diamond nanoparticles are transformed to spherical onions by the annealing. The spacing of lattice fringes is about 0.344 nm, which is close to that of the (002) planes of graphite.

At temperatures above 1900 °C, faceted polyhedral onions as shown in Fig. 2.1(c) are dominant in the samples. It is thought that spherical onions are transformed to polyhedral onions through the annealing above 1900 °C. Lattice fringes of polyhedral onions are more distinct and straight than those of spherical onions, indicating that polyhedral onions consist of further ordered graphitic sp^2 planes. The observed size of polyhedral onions is slightly larger than that of initial diamond nanoparticles. The increase in the volume is caused by the difference in the densities between diamond (3.515 g/cm^3) and graphite (2.267 g/cm^3) [3].

2.3.2 Raman spectroscopy

Figure 2.2 shows Raman spectra for the samples annealed at temperatures from 1500 to 2200 °C. All the spectra show two broad Raman bands around 1350 and 1580 cm^{-1}. The band at about 1580 cm^{-1} corresponds to the E_{2g} mode in the graphite structure of carbon (G band); in the spectrum range from 1200 to 1700 cm^{-1}, an ideal single-crystal graphite shows only this band at 1580 cm^{-1} [7]. The width of the G band is related to the disorder within the carbon sp^2 sheets [8]. Figure 2.3(a) shows the annealing temperature dependence of the full-width at half-maximum (FWHM) of the G band. The FWHM decreases as the annealing temperature increases.

In addition to the G band, so-called D band appears at about 1350 cm^{-1} for finite-size crystals of graphite (e.g. polycrystalline graphite, glassy carbon, etc.) [8, 9]. The true origin of the band has been an open debate [10, 14]. However it has been empirically known that a modest amount of disorder and the resultant decrease in in-plane domain size (L_a) of the graphitic sp^2 sheets can give rise to the band [8, 15]. We thus believe that the relative intensity of the D to G bands (I_D/I_G) can be used to represent the "relative" L_a, although the quantitative evaluation is difficult [10]. In Fig. 2.3(b), I_D/I_G of the spectra in Fig. 2.2 is plotted as a function of the annealing temperature. The I_D/I_G decreases with increasing the annealing temperature.

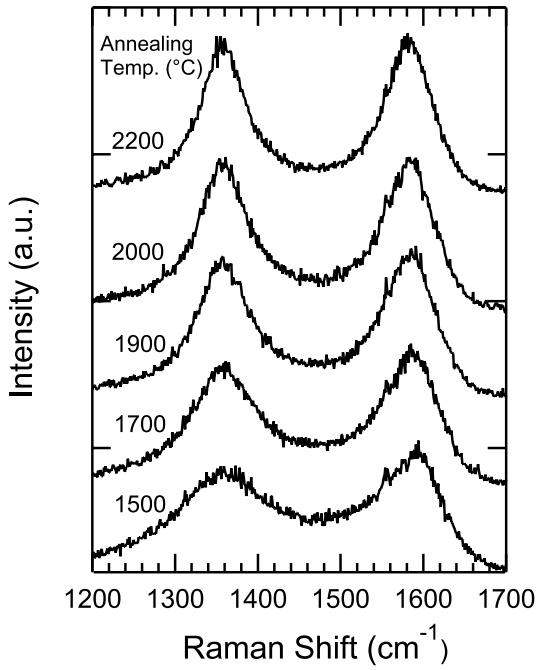

Figure 2.2: Raman spectra obtained with different annealing temperatures from 1500 to 2200 °C.

2.3.3 Electron energy-loss spectroscopy

Figure 2.4(a) shows the low-loss region of the EELS spectra for diamond nanoparticles, spherical onions and polyhedral onions. The spectrum of diamond nanoparticles (spectrum A) shows a broad peak around 25 eV. The spectrum is different from that of bulk diamond, which shows a peak at 33 eV due to the collective excitation of σ electrons in the valence band (σ-plasmon peak) with a shoulder at 25 eV due to the interband transition of σ electrons [11]. In Fig. 2.1(a), we can see thin amorphous layers on the surface of diamond nanoparticles. Generally, amorphous carbon exhibits a weak peak at 6 eV and a broad peak at 24 eV. These peaks are assigned to the collective excitation of π electrons (π-plasmon peak) and the collective excitation of total $\pi+\sigma$ valence electrons ($\pi+\sigma$ plasmon peak), respectively. The broad peak at 25 eV in spectrum A is considered to be the superposition of those of the diamond nanoparticles and the surface amorphous layers [12]. The π-plasmon peak of the surface amorphous layers is thought to be too weak and broad to appear in the spectrum A.

As diamond nanoparticles are transformed to spherical carbon onions, the peak shifts toward the lower energy (spectrum B). We can interpret this shift as the disappearance of the diamond core component and the growth of the $\pi+\sigma$ plasmon peak. In addition, we note here that the π-plasmon peak (indicated by arrow) appears around 6 eV. In the

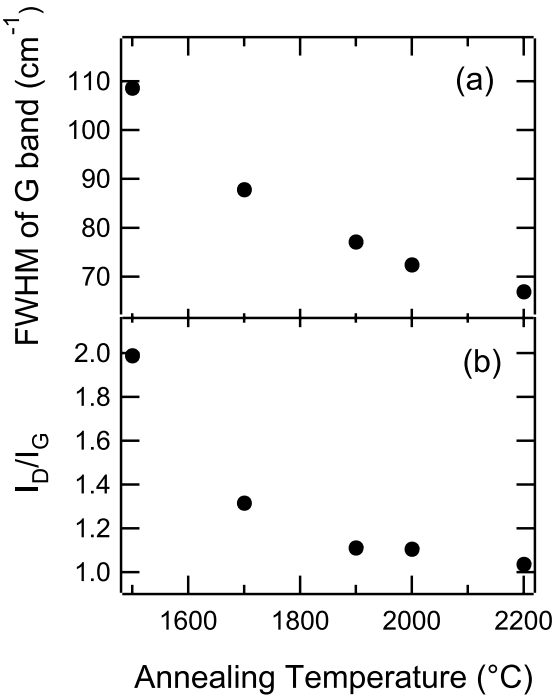

Figure 2.3: Annealing temperature dependences of (a) the FWHM of the G band and (b) the relative intensity of the D to G bands (I_D/I_G). Both of them decrease with increasing annealing temperature.

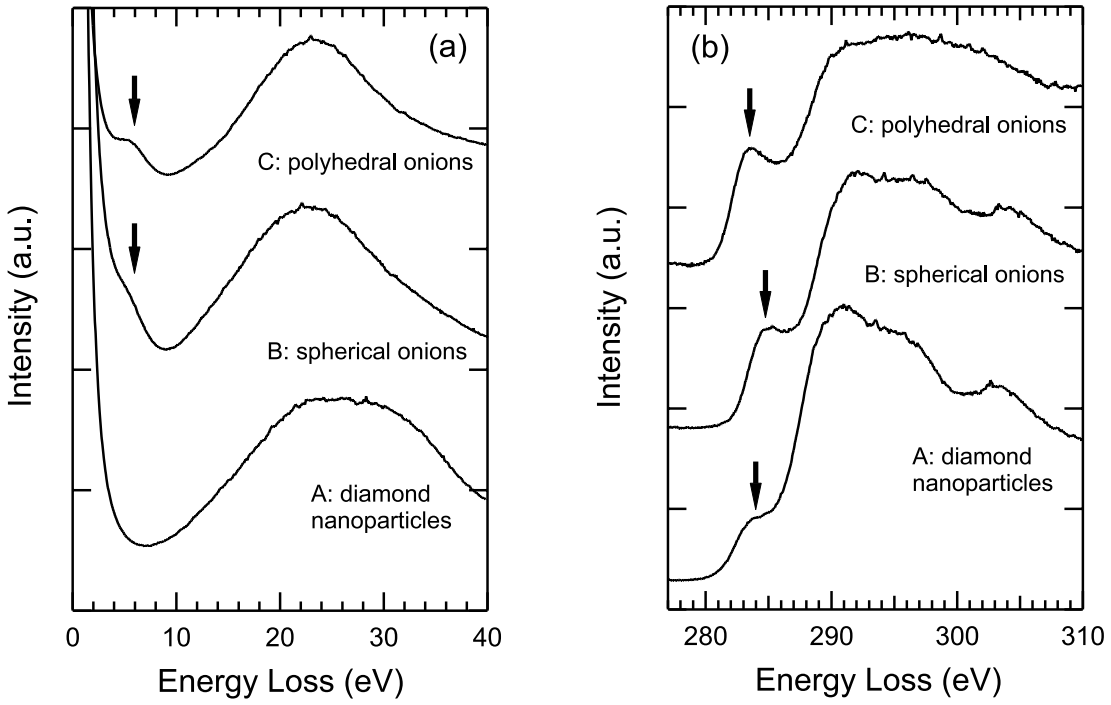

Figure 2.4: (a) EELS spectra in low-loss region and (b) in carbon K-edge core-loss region of 5 nm diamond nanoparticles (spectrum A), spherical carbon onions (spectrum B) and polyhedral carbon onions (spectrum C). The similarity in the shape of the ELNES of core-loss spectra between diamond nanoparticles and spherical onions indicates that spherical carbon onions have a number of sp^3 bonds.

low-loss spectrum of polyhedral onions (spectrum C), the energy of the π+σ plasmon peak is similar to that of spherical onions, although the π-plasmon peak is more pronounced. Since the energy of the π+σ plasmon peak represents the total density of π+σ valence electrons, the valence electron density of spherical onions is considered to be similar to that of polyhedral ones. These results imply that, through the transformation from diamond nanoparticles to carbon onions, the sp^3 network of carbon changes into sp^2 one, in agreement with the sequence of the HRTEM observation in Fig. 2.1.

Figure 2.4(b) shows the core-loss spectra in the carbon K-edge region. In the bulk diamond, the 1s $\rightarrow \sigma^*$ transition starts at $\sim$290 eV. In addition to the 1s $\rightarrow \sigma^*$ transition, bulk graphite and amorphous carbon show a peak at 285.4 eV due to the transition from the 1s core level to the π^* band (1s $\rightarrow \pi^*$ transition). In the spectrum of diamond nanoparticles [spectrum A in Fig. 2.4(b)], we can see a shoulder at about 284 eV (indicated by arrow) corresponding to the 1s $\rightarrow \pi^*$ transition, which is absent in the ideal diamond. The surface amorphous layers of diamond nanoparticles are considered to be responsible for the shoulder [12, 13]. The relative intensity of the 1s $\rightarrow \pi^*$ transition to the 1s $\rightarrow \sigma^*$ transition increases as diamonds are transformed into the onions (spectrum B and C).

The spectrum B in Fig. 2.4(b) represents the core-loss spectrum of spherical carbon onions. Although the spectrum B is shifted slightly toward the higher energy relative to the spectrum A and C, it is due to the fluctuation of the origin of the voltage axis during the EELS measurement. No definite shift was observed within the accuracy of our instrument. It is interesting to note that the ELNES above 1s $\rightarrow \sigma^*$ transition for spherical onions, which shows two peaks at 290 and 303 eV and a shoulder at around 297 eV, is similar to that for diamond nanoparticles (spectrum A) in the position and number of the peaks. To the first approximation, the ELNES represents the local density of the unoccupied states and provides useful information about the atoms in covalent bonding. The similarity in the shape of the ELNES between diamond nanoparticles and spherical onions indicates that spherical carbon onions have a number of sp^3 bonds. The fine structures above 1s $\rightarrow \sigma^*$ transition observed for diamond nanoparticles and spherical onions disappear for polyhedral onions (spectrum C), suggesting that sp^3 bonds almost completely change to sp^2 ones.

2.3.4 Electron spin resonance

Figure 2.5 shows the ESR spectra for initial diamond nanoparticles and samples obtained with different annealing temperatures. For diamond nanoparticles, we can observe a narrow signal with a peak-to-peak linewidth (ΔH_{pp}) of 8.5 G. The g value is estimated at g=2.0024. The small linewidth and the small deviation of the g value from the free-electron-spin g value (2.0023) indicate that the observed signal does not originate from

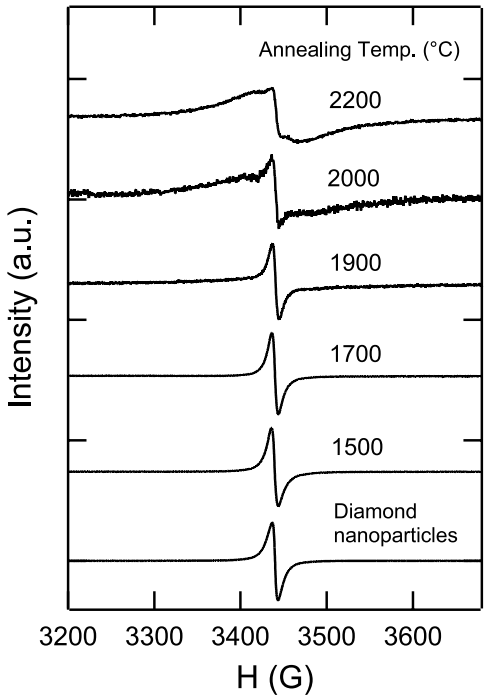

Figure 2.5: Dependence of ESR spectra on the annealing temperature. Note that, in addition to a narrow ESR signal, a broad one emerges at temperatures higher than 1900 °C.

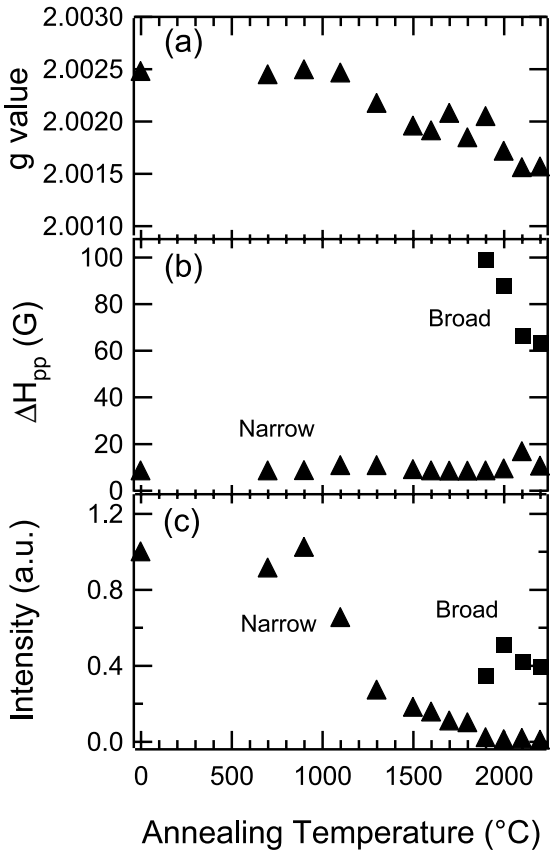

Figure 2.6: (a) g value, (b) ΔH_{pp} and (c) integrated intensity of narrow (triangle) and broad (square) ESR signals as a function of the annealing temperature.

magnetic impurities such as transition-metal in the sample [3].

At annealing temperatures from 1500 to 1700 °C, samples show a narrow ESR signal having a g value of 2.0020. The intensity of the signal increased with decreasing the measurement temperature, i.e., the signal shows a Curie-type temperature dependence. At annealing temperatures above 1900 °C, a broad signal appears in addition to the narrow one. The Q value of the ESR cavity was extremely low for these samples. In order to estimate the g value, ΔH_{pp} and intensity, the line shape was analyzed by fitting both the narrow and broad signals to Lorentzian line shapes. Although the observed broad signal was not quite Lorentzian, the deviation from the Lorentzian line shape was very small. Therefore, the present analysis gives an accurate order of magnitude [16].

The g value, ΔH_{pp} and intensity are plotted as a function of the annealing temperature in Figs. 2.6(a), 2.6(b) and 2.6(c), respectively. These values do not depend on the annealing temperature below 900 °C. In contrast, above 900 °C, the intensity of the narrow signal drastically decreases. At the same time, the g value becomes smaller,

although the ΔH_{pp} is almost the same. From 1500 to 1800 °C, the intensity of the signal gradually decreases as the annealing temperature increases. The intensity of the narrow signal finally becomes very small above 1900 °C and the broad signal appears. The ΔH_{pp} of the broad signal is estimated to be about 60-100 G and the g value is almost the same as that of the narrow signal. The ΔH_{pp} of the broad signal decreases with increasing the annealing temperature, although the intensity is almost independent of the annealing temperature.

2.4 Discussion

2.4.1 Transformation from diamond nanoparticles to carbon onions

In Fig. 2.5, diamond nanoparticles show a narrow ESR signal having a g value of 2.0024 and ΔH_{pp} of about 8.5 G. For CVD diamond, the ESR signal corresponding to vacancy-related defects in the diamond structure has ΔH_{pp} of 3-4 G [17, 18]. On the other hand, amorphous carbon shows a signal having ΔH_{pp} of 6-10 G [19]. The ESR signal with the ΔH_{pp} of 8.5 G observed for the diamond nanoparticles may thus be attributed to the dangling bond localized spins in the surface amorphous layers, which are seen in the HRTEM image [Fig. 2.1(a)]. The spin concentration of diamond nanoparticles estimated by using $CuSO_4 \cdot 5H_2O$ (1 spin/molecule) as a reference is 3.5×10^{20} spins/g. Above 900 °C, the intensity of the ESR signal drastically decreases and the g value becomes smaller. These changes are believed to be associated with the elimination of the surface amorphous carbon layers and the transformation of diamond nanoparticles into carbon onions because HRTEM observation suggests that the transformation starts around 900 °C [6].

The formation mechanism of carbon onions from diamond nanoparticles has already been proposed by Kuznetsov *et al.* [5]. They suggested that the (111) planes of diamond are transformed to the (001) planes of graphite as shown in Fig. 2.7. Recently, they discussed that two curved graphite sheets are formed from three (111) diamond planes by a "zipper"-like migration mechanism with the carbon atoms of the middle diamond layer being distributed equally between the two growing graphitic sheets [20]. This transformation proceeds from the surface to the center in the diamond nanoparticles. Therefore, the transformation results in the formation of carbon onions having almost the same diameter as the initial diamond nanoparticles. This mechanism is consistent with our observation, which shows that the carbon onions about 5 nm in diameter are formed from diamond nanoparticles with the average diameter of 5 nm (Fig. 2.1).

Since the transformation proceeds from the surface to the center, the particle at an early stage of the transformation has interface between inner diamond and outer graphite

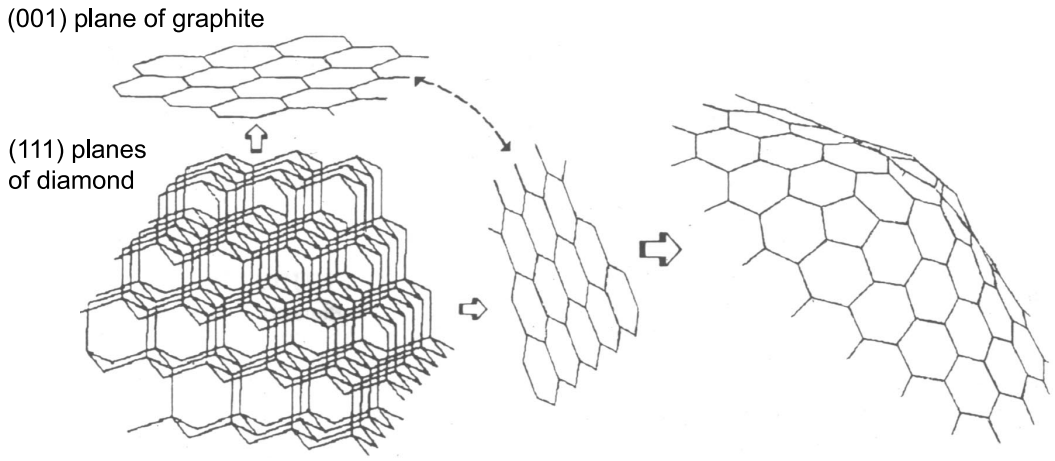

Figure 2.7: The scheme of the nanodiamond-onion transformation [5]. The (111) planes of diamond are transformed to the (001) planes of graphite.

phases. It is plausible that such interface contains dangling bonds. These dangling bonds are thought to be an alternative origin of the narrow ESR signal above 900 °C. The area of the interface becomes smaller with the progress of the transformation. This results in the decrease in the intensity of the narrow signal with increasing the annealing temperature up to 1500 °C.

2.4.2 Localization of π electrons in spherical carbon onions

In Fig. 2.5, there remains a narrow signal with a g value of 2.0020 around 1700 °C, where spherical carbon onions are formed. Since the g value becomes smaller at this temperature (g=2.0020), the signal is not believed to originate from the surface amorphous carbon layers of initial diamond nanoparticles and the interface between inner diamond and outer graphite phases during the transformation.

We should discuss here the origin of the narrow ESR signal observed around 1700 °C. De Vita *et al.* [21] theoretically performed the first-principles molecular dynamics simulations of a microscopic surface-induced diamond-to-graphite transition. Their results are shown in Fig. 2.8. Their simulations imply that, at an advanced stage of the transition, there is an intermediate disordered state, where the sp^3 and sp^2 bonds coexist; sp^3 bonds are located at peripheries of graphitic sp^2 sheets. In the transformation process from the diamond nanoparticle to the polyhedral onion, the spherical onion is an intermediate state as shown in Fig. 2.1. EELS study indeed pointed out that the spherical onion contains a number of sp^3 bonds in the structure. sp^3 like bonds at the peripheries of graphitic sp^2 sheets are thought to act as defects and may induce dangling bonds in

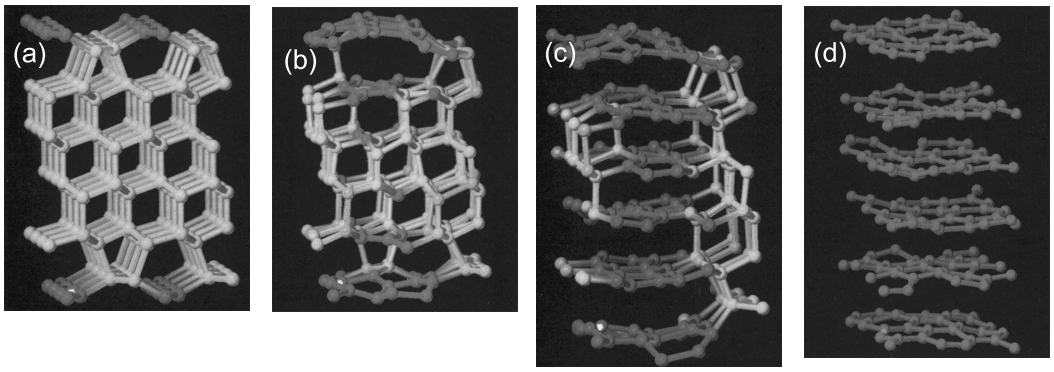

Figure 2.8: The first-principles molecular dynamics simulations of a microscopic surface-induced diamond-to-graphite transition [21].

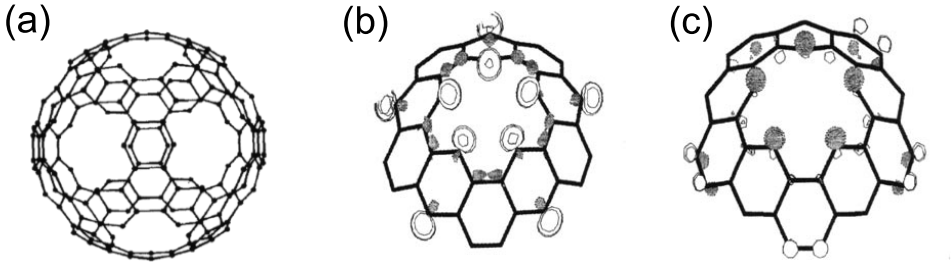

Figure 2.9: (a) The holed carbon cage C_{180}, which can be obtained by removing pentagonal rings from the I_h C_{240}. Localized σ- (b) and π- type (c) molecular orbitals in the holed graphitic structure [23].

the onions. Therefore, the narrow signal around 1700 °C in Fig. 2.5 can be assigned to the localized dangling bond spins associated with structural defects in the spherical carbon onions. This assignment is consistent with the observed Curie-type temperature dependence. The concentration of the localized spins in spherical onions is evaluated to be 3.9×10^{19} spins/g. This value corresponds to about 10 dangling bonds per spherical onion, when the number of carbon atoms in a spherical onion is assumed to be the same as that in a diamond nanoparticles 5 nm in diameter ($\sim$ 12000 atoms). We thus conclude that the spherical carbon onion consists of defective graphitic sp^2 shells (defective spherical onions), and is far from perfectly closed graphitic shells.[22].

The structural defects affect the electronic states in spherical onions. Very recently, Okotrub *et al.* [23] studied the carbon onions, which are prepared from diamond nanoparticles, by X-ray emission spectroscopy. Spherical onions exhibits a significant increase of the high-energy maximum in the emission spectrum that might be caused by the defect structures of graphitic networks. The feature was very similar to the calculated spectrum for the holed carbon cage C_{180} [Fig. 2.9(a)], which can be obtained by removing pentagonal rings from the I_h C_{240}. Furthermore, the localization of the electrons in the holed graphitic structures [Figs. 2.9(b) and 2.9(c)] is theoretically indicated. Their results are consistent with our present results by EELS and ESR. It should be stressed again that present ESR spectra for the spherical onions show only the narrow signal corresponding to dangling bond spins, although HRTEM and Raman studies suggest that they are composed of graphitic sp^2 sheets and EELS study indicates the presence of π electrons. The absence of an ESR signal due to conduction π electrons suggests that π electrons in defective spherical onions are considered to be localized in the small domains of graphitic sp^2 sheets with dangling bond defects in the peripheries, and do not move across the domains.

2.4.3 Delocalization of π electrons in polyhedral carbon onions

Above 1900 °C, a broad ESR signal emerges in addition to the narrow one. Taking into consideration the extremely low Q value observed, the additional broad signal can be assigned to conduction π electrons in the polyhedral onions, which are dominant above 1900 °C. For activated carbon fibers, a broad signal superimposed upon a narrow one was assigned to conduction π electron spins by Nakayama and co-workers [16, 24].

Present Raman studies show that both the FWHM of the G band and the I_D/I_G decrease as annealing temperature increases from 1500 to 1900 °C (Fig. 2.3). These results can be interpreted as the decrease in the number of defects and the increase in L_a, respectively. ESR study also indicates that the concentration of the dangling bond localized spins becomes smaller ($\sim 7.6 \times 10^{18}$ spins/g) at 1900 °C. In other words,

graphitization proceeds with increasing the annealing temperature, and spherical onions are transformed into polyhedral ones. As a result of the decrease in the number of defects, π electrons in polyhedral onions are delocalized; π electrons can act as conduction electrons. Nevertheless, ESR spectra also exhibit a weak narrow signal which is assigned to the dangling bond spins, indicating that there still remains a small number of dangling bonds associated with structural defects in polyhedral onions.

Figure 2.6(b) shows that ΔH_{pp} of the broad ESR signal decreases with increasing the annealing temperature. In the Raman study above 1900 °C, the FWHM of the G band decreases as the annealing temperature increases [Fig. 2.3(a)], indicating an improvement in the crystallinity. The improvement of the crystallinity in polyhedral onions is considered to lead to the decrease in ΔH_{pp} of the broad ESR signal. di Vittorio *et al.* [16] and Andersson *et al.* [3] discussed the large linewidth $\Delta \mathrm{H}_{pp}$ of the ESR signal corresponding to conduction π electrons. They showed that the linewidth depends on the spin-lattice (T_1) and spin-spin (T_2) relaxation times as

$$\Delta H_{pp} \propto \frac{\hbar}{g\mu_B}\left(\frac{1}{T_2} + \frac{1}{2T_1}\right), \tag{2.1}$$

where μ_B is the Bohr magneton.

For T_1, there are two kinds of relaxation process. One is associated with electron scattering by the phonons in the domain of the graphitic sp^2 sheet, and the other by the domain boundary. T_1 is thus expressed as

$$\frac{1}{T_1} \approx \alpha(\Delta g)^2\left(\frac{1}{\tau_b} + \frac{1}{\tau_p}\right), \tag{2.2}$$

where α is a numerical factor, Δg is the deviation of the g value from the g_0, τ_b and τ_p are the scattering time by boundaries and phonons, respectively. The boundary scattering mechanism is related to the Fermi velocity (υ_F) and the in-plane domain size (L_a) as $\tau_b = L_a/\upsilon_F$. Since υ_F is known about 9.7×10^5 m/s for π electrons in bulk graphite, τ_b is roughly estimated to be 10^{-15} s for several nanometers in L_a. On the other hand, τ_p associated with the in-plane and out-of-plane phonons are reported to be several orders of magnitude larger than the τ_b [3, 25, 26]; the contribution of scattering by phonons to the T_1 relaxation is small enough to be negligible in the broad linewidth. T_1 relaxation is thus governed by the boundary scattering process. As a result, T_1 have a relation as

$$\frac{1}{T_1} \propto \frac{\upsilon_F}{L_a}. \tag{2.3}$$

For the T_2 process, the dipolar interaction between conduction π electrons can be omitted because the conduction electrons move rapidly within the small domain of the graphitic sp^2 sheets. However, the boundaries of the small domains in polyhedral onions

still contain localized electrons associated with dangling bonds. Therefore, the dipolar interaction between conduction electron delocalized spins and dangling bond localized spins has to be taken into consideration in the T_2 process. The dipolar width ΔH_{pp} with this process depends on the average distance between conduction π electrons and dangling bonds (r) as

$$\Delta H_{pp} \propto 1/r^3, \tag{2.4}$$

within a graphitic domain with a size of several nanometers [16].

The above relations show that the ESR linewidth ΔH_{pp} corresponding to the conduction π electrons is related to L_a and r, indicating that ΔH_{pp} is sensitive to the degree of the ordering in the graphitic sp^2 sheets. As can be seen in Fig. 2.6(b), the ΔH_{pp} of the broad signal becomes small as annealing temperature increases above 1900 °C. We should mention here whether T_1 or T_2 process mainly contributes to the annealing temperature dependence of the linewidth of the broad ESR signal. Present Raman studies show that FWHM of the G band similarly decreases with increasing the annealing temperature above 1900 °C [Fig. 2.3(a)] whereas I_d/I_g is almost constant [Fig. 2.3(b)]. The result suggests that, although the L_a is almost the same, the number of the defects such as dangling bond at the peripheries of the small domain decreases. The decrease in the number of defects is believed to bring about the increase in r. Therefore, the increase in r mainly contributes to the decrease in ΔH_{pp}. We conclude that the contribution by the T_2 process, which is associated with r, is dominant in the annealing temperature dependence of the linewidth of the broad ESR signal; in other words, the ESR signal corresponding to the conduction π electrons is mainly governed by the spin-spin relaxation between conduction π electron delocalized spins and dangling bond localized spins.

2.5 Conclusion

We have investigated the structure and electronic properties of carbon onions, and the correlation between them. HRTEM observation demonstrated that diamond nanoparticles are transformed into spherical carbon onions by the annealing at 1700 °C, and finally into polyhedral onions above 1900 °C. Raman spectroscopy indicated that the transformation is brought about by the progress of graphitization with increasing the annealing temperature. The low-loss spectrum in the EELS study showed that the graphitic structure is dominant in both spherical and polyhedral carbon onions. Nevertheless, the core-loss spectrum of spherical onions is similar to that of diamond nanoparticles, suggesting that a number of sp^3 bonds are contained in spherical carbon onions. In ESR studies, we found that spherical onions show only the narrow ESR signal with a g value of 2.0020 due to the dangling bonds associated with structural defects in the onions, although HRTEM,

Raman and EELS studies indicate the presence of π electrons. These results suggest that the spherical onion consists of small domains of graphitic sp^2 sheets with dangling bond defects in the peripheries. π electrons in spherical onions are thus localized in the small domains and do not act as conduction electrons. On the other hand, for polyhedral onions, an additional broad signal due to conduction π electrons appears, suggesting that further graphitization decreases the number of dangling bonds and leads to the delocalization of π electrons. The ESR signal corresponding to the conduction π electrons is mainly governed by the spin-spin relaxation between conduction π electron delocalized spins and dangling bond localized spins. Present results strongly suggest that the structure of spherical carbon onions is far from perfectly closed graphitic shells and the sphericity is attributed to imperfect shells with a number of defects such as dangling bonds (defective spherical onions). Moreover, the polyhedral onions have an ordered graphitic structure as a result of a further progress in graphitization.

References

[1] R. F. Egerton and M. J. Whelan, Journal of Electron Spectroscopy and Related Phenomena **3**, 232 (1974).

[2] T. Cabioc'h, J. P. Rivière, M. Jaouen, J. Delafond, and M. F. Denanot, Synthetic Metals **77**, 253 (1996).

[3] O. E. Andersson, B. L. V. Prasad, H. Sato, T. Enoki, Y. Hishiyama, Y. Kaburagi, M. Yoshikawa, and S. Bandow, Phys. Rev. B **58**, 16387 (1998).

[4] K. Nakada, M. Fujita, G. Dresselhaus, and M. S. Dresselhaus, Phys. Rev. B **54**, 17954 (1996).

[5] V. L. Kuznetsov, A. L. Chuvilin, Y. V. Butenko, I. Y. Mal'kov, and V. M. Titov, Chem. Phys. Lett. **222**, 343 (1994).

[6] E. D. Obraztsova, M. Fujii, S. Hayashi, V. L. Kuznetsov, Yu. V. Butenko, and A. L. Chuvilin, Carbon **36**, 821 (1998).

[7] F. Tuinstra and J. L. Koenig, J. Chem. Phys. **53**, 1126 (1970).

[8] D. S. Knight and W. B. White, J. Mater. Res. **4**, 385 (1989).

[9] R. J. Nemanich and S. A. Solin, Phys. Rev. B **20**, 392 (1979).

[10] H. Wilhelm, M. Leaurain, E. McRae, and B. Humbert, J. Appl. Phys. **84**, 6552 (1998).

[11] R. F. Egerton, *Electron Energy-Loss Spectroscopy in the Electron Microscope*, (Plenum, New York, 1996).

[12] P. J. Fallon and L. M. Brown, Diamond Relat. Mater. **2**, 1004 (1993).

[13] D. F. Blake, F. Freund, K. F. M. Krishnan, C. J. Echer, R. Shipp, T. E. Bunch, A. G. Tielens, R. J. Lipari, C. J. D. Hetherington, and S. Chang, Nature **332**, 611 (1988).

[14] M. J. Matthews, M. A. Pimenta, G. Dresselhaus, M. S. Dresselhaus, and M. Endo, Phys. Rev. B **59**, R6585 (1999).

[15] J. Robertson, Adv. Phys. **35**, 317 (1986).

[16] S. L. di Vittorio, A. Nakayama, T. Enoki, M. S. Dresselhaus, M. Endo, and N. Shindo, J. Mater. Res. **8**, 2282 (1993).

[17] M. Fanciulli and T. D. Moustakas, Phys. Rev. B **48**, 14982 (1993).

[18] C. F. O. Graeff, C. E. Nebel, M. Stutzmann, A. Flöter, and R. Zachai, J. Appl. Phys. **81**, 234 (1997).

[19] I. Watanabe and K. Sugata, Jpn. J. Appl. Phys. **27**, 1808 (1988).

[20] V. L. Kuznetsov, I. L. Zilberberg, Yu. V. Butenko, A. L. Chuvilin, and B. Segall, J. Appl. Phys. **86**, 863 (1999).

[21] A. De Vita, G. Galli, A. Canning, and R. Car, Nature **379**, 523 (1996).

[22] A. Maiti, C. J. Brabec, and J. Bernholc, Modern Phys. Lett. B **7**, 1883 (1993).

[23] A. V. Okotrub, L. G. Bulusheva, V. L. Kuznetsov, Yu. V. Butenko, A. L. Chuvlin, and M. I. Heggie, J. Phys. Chem. A **105**, 9781 (2001).

[24] A. Nakayama, K. Suzuki, T. Enoki, S. L. di Vittorio, M. S. Dresselhaus, K. Koga, M. Endo, and N. Shindo, Synthetic Metals **55-57**, 3736 (1993).

[25] K. Sugihara, Phys. Rev. B **28**, 2157 (1983).

[26] K. Sugihara, Phys. Rev. B **37**, 7063 (1988).

Chapter 3

Structural Analysis of Carbon Onions

3.1 Introduction

In the previous chapter, we have studied carbon onions prepared from diamond nanoparticles by transmission electron microscopy (TEM), Raman spectroscopy, electron energy-loss spectroscopy (EELS), and electron spin resonance (ESR). From the TEM studies, we demonstrated that, by annealing diamond nanoparticles at about 1700 °C, spherical onions are formed. At above 1900 °C, spherical onions are transformed into polyhedral ones with facets. EELS and ESR studies revealed that the spherical onions consist of defective graphitic shells having structural defects such as dangling bonds instead of the fullerene-like perfectly closed shells containing only pentagonal, hexagonal, and heptagonal carbon rings [1]. The further progress of graphitization develops the graphitic sp^2 networks and brings about the formation of polyhedral onions.

Although the previous chapter provides a possible structural model of the spherical onions (a defective spherical onion model), the precise structure is still unclear. Since detailed knowledge of the structure of the onions is crucial to fully understand their physical, chemical and mechanical properties, a more detailed structural study is strongly required. In this chapter, in order to acquire more detailed information about the structures and formation mechanism of the onions transformed from diamond nanoparticles, we have carried out the synchrotron x-ray diffraction studies on a series of carbon onions.

3.2 Experiment

The carbon onions 20 mg in quantities were prepared by the method described in the previous chapter. Briefly, spherical carbon onions were formed by annealing diamond

nanoparticles at about 1700 °C in vacuum. Polyhedral onions were dominant at temperature higher than 1900 °C. The diameter of the obtained onions is almost the same as that of the initial diamond nanoparticles because one diamond nanoparticle is transformed into one onion.

The x-ray diffraction experiment was performed on the ID01 beam line at European Synchrotron Radiation Facility (ESRF) in Grenoble, France, which is a source of third generation. The optics consisted of a double-crystal Si_{111} monochromator, located between two mirrors. Such an arrangement provides a fixed-exit monochromatic beam and maintains the focal spot of 0.134×0.024 mm^2 (Full Width in Half Maximum in the horizontal and vertical directions, respectively) and allows an energy resolution of 1 eV on an absolute scale ($\Delta E/E \sim 10^{-4}$) after calibration by appropriate absorption edges. A high rate of harmonic rejection ($< 10^{-4}$) is due to the use of two mirrors. In the present experiment the energy of the incident beam was tuned to 8.1 keV yielding the wavelength of 1.53 $\mathring{A}$. The samples were mounted on a goniometer axis into 2 mm Lindemann glass capilaries. The measurements were performed for the four samples: the initial diamond nanoparticles, the diamond nanoparticles annealed at 1400 °C, the spherical onions formed at 1700 °C and the polyhedral onions formed at 2000 °C. In order to remove the background the additional measurements were carried out for air scattering and the empty capillary which were then subtracted from the recorded intensities.

3.3 Results

The intensity patterns for the four samples are shown in Figs. 3.1-3.4, covering the full angular range of the measurements.

3.3.1 Diamond nanoparticles

The diffraction pattern for initial diamond nanoparticles shows prominent peaks at angles of 43.34°, 74.68°, 90.36° and 118.37° which correspond to the normal structure factor peaks of diamond for the (111), (220), (311) and (400) reflections, respectively. The instrument resolution is 0.1°, so these peaks are much broader than would normally be observed in crystalline diamond. The diffraction broadening arises primarily from the size of the nanoparticles but can also be caused by strains and defects in the crystal material itself. The parameters for the five main peaks observed for this sample are given in Table 3.1 with corresponding values for normal diamond. There is subsidiary broad peak centered on 26°. As shown in the following subsections, this peak corresponds to the (002) peak of graphite and therefore suggests that there may be some contribution from small quantities of sp^2-bonded carbon in the initial sample material. The surface

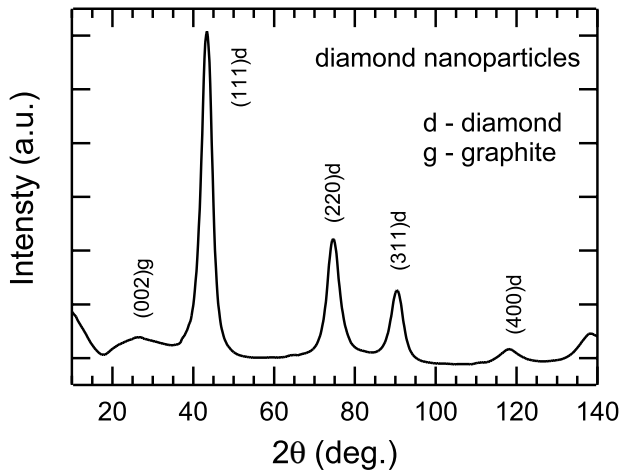

Figure 3.1: The x-ray diffraction profile for initial diamond nanoparticles.

amorphous carbon layers of the diamond nanoparticles as shown in the previous chapter is considered to be responsible for this peak. The rise in intensity at low angles may be partly attributed to incomplete corrections for air scattering but is primarily due to small angle scattering arising from the particulate nature of the material; for this angle-scale, the rise indicates the presence of very small fragments of diamond.

3.3.2 Nanoparticles after heat treatment at 1400 °C

The diffraction pattern for the sample annealed at 1400 °C shows significant changes from that for initial diamonds. The three main diamond peaks are reduced in intensity and show considerable narrowing of the peak profile. The second peak occurs at a slightly reduced angle but the mean position of the other peaks remains the same. These parameters are also listed in Table 1 and compared in the following subsection. The most obvious change in the pattern is the growth of a broad graphite peak (002) at 25.22° and the lower intensity peaks at 53.06° and 79.08°. These peaks are broader than the original diamond peaks and indicate that either the number of correlated graphene sheets is very small or that they are highly defective as in activated carbons [2]. It is clear that parts of the diamond nanoparticles have been converted from a sp^3-bonded structure to one containing a significant number of sp^2-bonded layers. The simplest interpretation of these results is to assume that there is a distribution of particle sizes in initial diamond nanoparticles and that the smaller particles are converted to graphite at a lower temperature than the larger ones [4]. These characteristics are discussed more fully in the following subsection.

Table 3.1: Summary of the present results. The values of uncertainties are given in parentheses.

sample	2θ(deg.)	FWHM(deg.)	2θ(deg.) for diamond
diamond nanoparticles	26.02 (1.00)	15.26 (3.50)	
	43.34[d] (0.02)	2.99 (0.15)	43.62
	74.68[d] (0.03)	3.87 (0.18)	74.69
	90.36[d] (0.12)	3.51 (0.20)	90.69
	118.37[d] (0.30)	5.50 (0.40)	118.17
1400 °C	25.22 (0.03)	7.76 (0.160)	
	43.40[d] (0.02)	2.75 (0.18)	
	43.51 (0.02)	0.72 (0.18)	
	53.06 (0.43)	11.76 (1.76)	
	74.72[d] (0.04)	1.81 (0.18)	
	79.08 (0.34)	11.38 (0.94)	
	90.60[d] (0.09)	3.41 (0.30)	
	118.09[d] (0.53)	2.93 (1.80)	
1700 °C	24.46 (0.04)	6.67 (0.18)	
	43.58 (0.04)	3.34 (0.23)	
	51.76 (0.49)	9.31 (2.08)	
	75.07[d] (0.32)	1.94 (0.70)	
	79.09 (0.28)	6.51 (1.06)	
	90.84[d] (0.73)	11.47 (2.32)	
	119.78[d] (2.93)	12.34 (4.00)	
2000 °C	24.57 (0.04)	6.39 (0.18)	
	43.48 (0.04)	3.61 (0.20)	
	51.78 (0.50)	14.87 (2.50)	
	78.75 (0.35)	5.97 (1.07)	
	88.37 (0.80)	37.00 (12.00)	

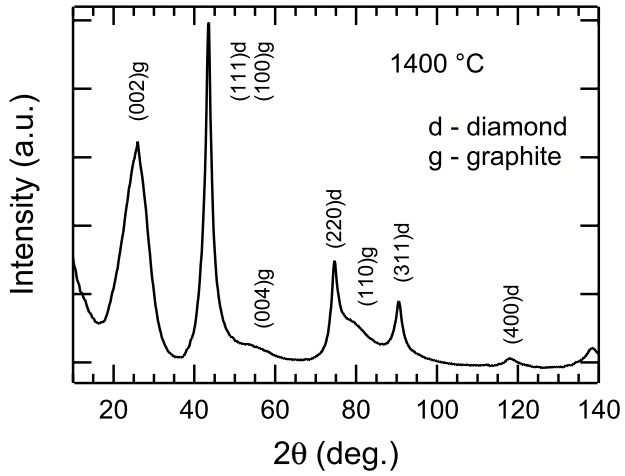

Figure 3.2: The diffraction intensity for a sample after heat treatment at 1400 °C.

3.3.3 Formation of spherical onions at 1700 °C

For the sample annealed at 1700 °C, there is an increase in the graphitic (002) peak with a slight narrowing of the profile. The second, third and fourth diamond peaks are further reduced, indicating that much of the sp^3 coordination has been effectively removed at the higher temperature. A broad peak remains at 43.5° which corresponds to the same position as the original diamond peak but it has an asymmetric profile and can be more readily attributed to the graphitic (100) peak. However, the (111) diamond peak is also expected to appear at this position. It is important to notice that the FWHM of the (220), (311) and (400) diamond peaks are increased in comparison with sample annealed at 1400 °C which indicates that the size of the diamond nanoparticles is clearly reduced.

3.3.4 Development of facetted polyhedral onions at 2000 °C

After heat treatment at 2000 °C, the main graphitic peak increases in intensity and narrows slightly. This effect is reproduced in the asymmetric double peak covering the 40-60° range. This change indicates a greater correlation between the graphene sheets and the development of facetted planes on the surface of the particles, as revealed in the TEM pictures. The diamond peaks disappear completely which indicates that there are no original diamond correlations in the final sample.

For the onions, the diffraction peaks of graphite indexed as (002n) and (hk0) are expected to appear in the profile. The peaks (hkl) with l not equal to 0, i.e., (101), (112), (201), are due to the cross-correlations between graphitic layers. Since the graphitic interlayer correlation is considered not to be retained in the onions, these peaks disappear

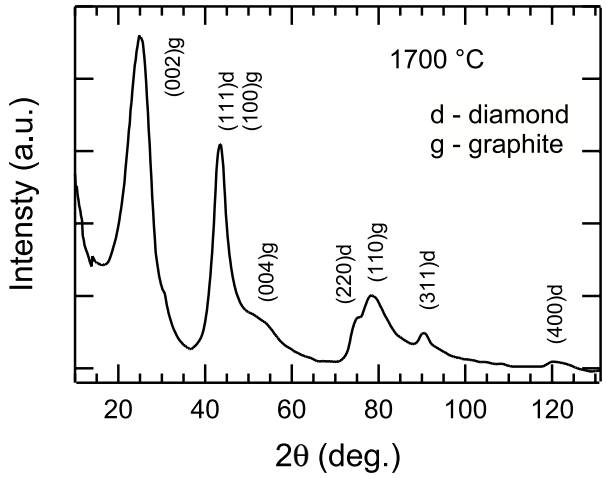

Figure 3.3: The diffraction intensity for a sample consisting of spherical carbon onions after heat treatment at 1700 °C.

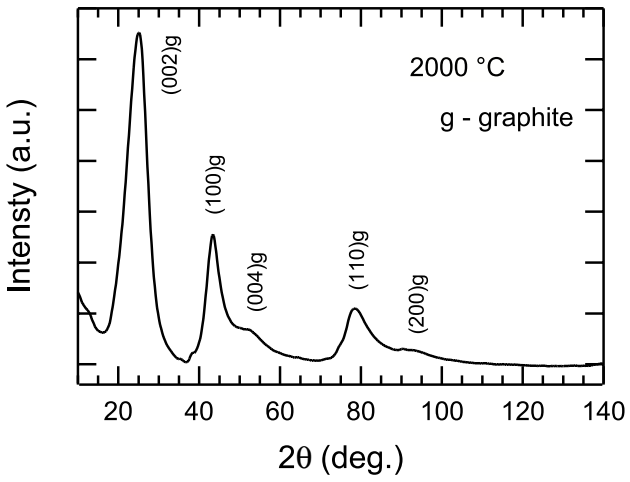

Figure 3.4: The diffraction intensity for a sample consisting of polyhedral carbon onions after heat treatment at 2000 °C.

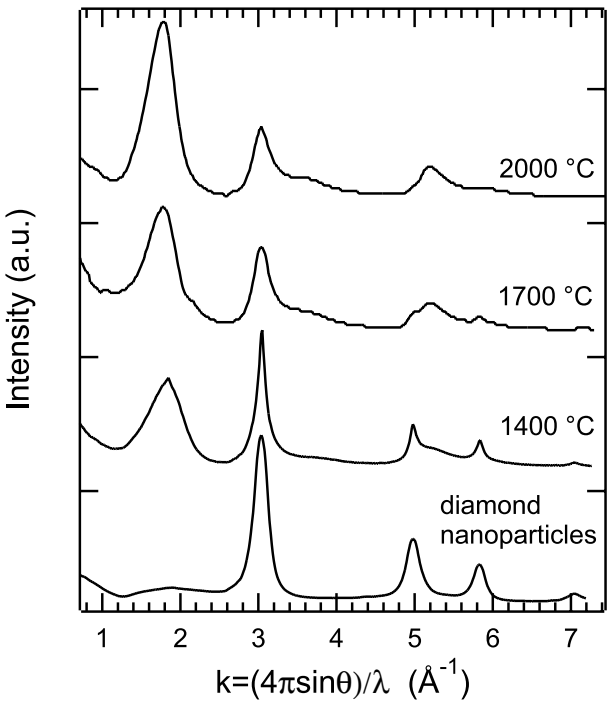

Figure 3.5: The super-imposed results of the four samples shown as a function of the scattering vector k.

in the present diffraction profiles in Figs. 3.2-3.4. Indeed, the profile in Fig. 3.4 is very similar to those observed for turbostratic carbons or nanotubes in which layers are stacked without correlation [3].

3.4 Discussion

The present results illustrate the structural changes occurring in the heat treatment of the diamond particles at different temperatures. The measured intensities for each of the samples may be converted to a function of the scattering vector $k = 4\pi \sin\theta/\lambda$ (2θ is the scattering angle and λ is the wavelength) and are shown super-imposed in Fig. 3.5 to emphasize the changes. These results can be compared with the findings of other studies using different techniques. The diffraction measurements are complementary to the TEM results as the scattering data is obtained from the whole of the sample volume whereas the TEM probes only a small selected sample volume. However, there is good general agreement between the two methods as illustrated by the discussion in the following paragraphs.

The broad features of the peaks observed in all samples result from the finite size of

the nanoparticles which are stated to be in the region several nanometers. Diffraction broadening is a well-known feature for finite-sized crystallites and results from the restricted range of the contributions from the correlated layers of the crystal. The width of the peak is inversely proportional to the dimensions of particle and can be represented by the Scherrer equation [5]

$$\beta = \frac{K\lambda}{D\cos\theta_B}, \tag{3.1}$$

where β in the unit of radian is the angular half-width of the peak (after correction for instrumental resolution), λ is the incident x-ray wavelength, θ_B is the Bragg angle in the unit of degree and D is the dimension of the crystallite or the distance for which there are correlated layers ; K is a constant that is close to unity and depends on the shape of the crystallite ($K = 0.9$ in the present study). In the present study the observed width is much greater than the instrumental resolution so that the value of β can be readily extracted from the observed data. An approximate evaluation from the datasets gives D-values that suggest a mean crystallite size of 3 ± 0.2 nm. This value is smaller than that estimated from the TEM measurements but this apparent discrepancy is not regarded as important because the diffraction profile will give an average over all crystallite sizes. There is evidence that the range is large as the base of the peaks is broad, indicating the presence of quite small crystallites. Furthermore, the diffraction data represent an effective range in the correlated layers of the crystallite which may be smaller than the actual particle size. Taking the lattice distortion into consideration, the cyrstalline size D can be roughly estimated as follows

$$\Delta S = \frac{K}{D} + 2eS, \tag{3.2}$$

where $K = 0.9$, $\Delta S = (2\beta\cos\theta_B)/\lambda$, $S = (2\sin\theta_B)/\lambda$, and $e = \Delta d_{hkl}/d_{hkl}$. Assuming the degree of the lattice distortion $e = 0.01$, D of about 4.2-4.5 nm can be obtained. It is possible, in principle, to estimate the size distribution from a detailed analysis of the profile but it does not seem justified in the present case and does not have a direct impact on the discussion of the structural changes with temperature which follows.

The first transition at or below 1400 °C shows the development of peaks associated with graphite but there is a considerable narrowing of the main diamond peak. This change in profile suggests that the smaller diamond particles are more readily converted to graphite than the larger ones, leaving the residual diamond particles with a narrower distribution of sizes. It is also noticeable that the graphite (002) peak is much broader than the original diamond (111) peak indicating that the number of graphite layers for this sample material remains small. These changes are in agreement with the TEM results that indicate the development of a graphitic layer on the outside of the particles. The sharpening of the diamond peaks is also seen in the (220) and (311) reflections although

these peaks are superimposed on new broad peaks of graphitic origin. The diffraction results are therefore entirely in accord with the conclusions drawn from the TEM data.

The second transition at or below 1700 °C shows a further change in pattern corresponding to the development of a more graphitic nature but the diamond features have not completely disappeared and remain as low intensity broad peaks; this behaviour is particularly noticeable for the peak at 75° (or $k \sim 5$ Å^{-1}). This transition corresponds to the development of carbon onions in the TEM pictures but it seems likely that the several spherical onions still contain tiny diamond central cores. The residual diamond peaks are broadened because the particle size is effectively reduced by the conversion of the outer coat to a spherical shell with graphitic features. Once again, the diffraction results are in agreement with the TEM studies.

The final stage concerns the transition at or below 2000 °C. There is now no clear evidence of a diamond peaks. There is an increase in the intensities of all the broad graphitic peaks. The TEM pictures show the development of facetted graphite sheets on the outside of the particles but this change is not directly reflected in the diffraction pattern because the peaks remain broad. The values of intershell spacing 0.35-0.36 nm for the onions, estimated from the position of the first diffraction peaks appearing at 24-25°, are clearly greater than that of graphite (0.335 nm). This comparison indicates that intershell interaction in graphitic shells of onions obtained at 1700 °C and 2000 °C is much weaker same as in tubostratic graphite when compared to perfect graphite, being consistent with the defective spherical onion model proposed in the previous chapter.

The sequence of changes observed in both the diffraction and the TEM studies confirm a steady transformation of sp^3-bonding to sp^2-bonding with increasing heat-treatment temperature. This characteristic can also be revealed in spectroscopic studies such as Raman, ESR, and EELS in the previous chapter. The EELS data shows in low-loss and K-edge core-loss regions that the sp^2-bonded structure is dominant in carbon onions. However, the core-loss spectra exhibit features which can be related to $1s \rightarrow \sigma^*$ transition and is considered to be explained by the presence of the tiny residual diamond nanoparticles in the center of the spherical onions or bridge-like sp^3 bondings between adjacent sp^2 planes. These features disappear for the polyhedral onions. On the other hand, the $1s \rightarrow \pi^*$ transition, characteristic of bulk graphite and disordered graphite-like carbons, was observed for the original diamond nanoparticles which indicates the presence of disordered sp^2 bondings in the starting materials. The intensity of the $1s \rightarrow \pi^*$ transition increase with annealing temperature suggesting that the sp^3 bonds completely change to sp^2 ones. Similar tendency was revealed by Raman spectroscopy. The ESR studies suggested localization of π electrons in the spherical onions and delocalization in the polyhedral onions which are in agreement with the present observation because delo-

calization of the π electrons can be regarded as indication of graphitization undergoing at temperatures higher than 1900 °C.

The most interesting dataset is that for sample annealed at 1700 °C, with the formation of the spherical carbon onions. In the present case the number of layers is expected to be in the region of eight to ten or possibly less for the smaller particles. Current TEM studies suggest that the shells are constructed of genuine spherical layers although it is thought that larger onions may have outer layers that are segmented and adopt a planar graphene structure [6]. Unlike nanotubes, the shells must therefore have curvature in two directions and there is a theoretical interest in the local bonding arrangement. The fundamental morphology of C_{60} provides a basic concept of sphericity based on the combination of five and six-membered rings. Some of the higher order fullerenes also have a spherical conformation [7] but it is difficult to see how a series of layers can be created with the correct inter-layer spacings for stability. Due to the broad nature of the peaks in the present diffraction data, it is not possible to make any further comments on the likely structure of the onions in terms of the atomic pair correlation function. However, diffraction studies covering a wider k-range should enable this aspect to be investigated, as already demonstrated for pulsed neutron measurements on activated carbons [8].

3.5 Conclusion

In this chapter, we have investigated the transformation of diamond nanoparticles by heat treatment up to 2000 °C using synchrotron x-ray diffraction. Precise measurements have been made on four heat-treated samples using a high intensity beam from a synchrotron radiation source. The changes in the diffraction pattern have been analyzed in terms of variation in the intensities and peak profiles of the Bragg peaks arising from diamond and graphite-like structures. The results demonstrate a sequence of changes which correlate well with TEM studies on same samples and involve a transformation from a sp^3 to sp^2-type bonding configuration. There is an initial development of a graphitic outer coat on the diamond nanoparticles which then becomes transformed into a carbon onion with a spherical shell surrounding a diamond core. The interlayer distance for the onions is larger than that for bulk graphite, indicating that the graphitic shells in the onions are defective and interlayer interaction is much weaker. At higher temperatures, the diamond core is reduced in size and the outer layers develop a facetted graphitic structure. The results are also in good agreement with other studies based on Raman, ESR, and EELS measurements in the previous chapter. It is essential to point out that x-ray diffraction is a direct probe of the atomic structure and provide information about atomic arrangement without making any additional hypothesis which are necessary when other techniques are

used. The detailed atomic arrangement of the carbon onions cannot be deduced from the present measurements but further work will address this issue.

References

[1] H. Terrones and M. Terrones, J. Phys. Chem. Solids. **58**, 1789 (1997).

[2] A. Szczygielska, A. Burian, and J. C. Dore, submitted.

[3] A. Burian, J. C. Dore, H. E. Fischer, and J. Sloan, Phys. Rev. B. **59**, 1665 (1999).

[4] V. L. Kuznetsov, I. L. Zilberberg, Y. V. Butenko, A. L. Chuvilin, and B. Segall, J. Appl. Phys. **86**, 863 (1999).

[5] H. P. Klug and L. E. Alexander, *X-ray Diffraction Procedures for Polycrystalline and Amorphous Materials.* (Wiley, New York, 1974).

[6] F. Moreau, A. A. Lucas, Ph. Lambin, J. C. Dore, A. Burian, J. Sloan, and M. L. H. Green, submitted.

[7] M. S. Dresselhaus, G. Dresselhaus, and P. C. Eklund, *Science of Fullerenes and Carbon Nanotubes* (Academic Press, New York, 1996).

[8] J. C. Dore, M. Sliwinski, A. Burian, W. S. Howells, and A. Cazorla, J. Phys. Cond. Matt. **11**, 9189 (1999).

Chapter 4

Extinction Spectra of Carbon Onions

4.1 Introduction

Optical properties of carbon onions have attracted interest in the context of carbonaceous nano-material science and technology. Moreover, carbon onions have been proposed as possible candidates for the carbonaceous dust particles giving rise to an interstellar extinction bump at 4.6 μm^{-1} [1, 2]. In this chapter, we study optical extinction properties of spherical and polyhedral carbon onions prepared from diamond nanoparticles [3]. The onions have already been defined by transmission electron microscopy (TEM), electron energy-loss spectroscopy (EELS), and electron spin resonance (ESR) in chapter 2, and synchrotron x-ray diffraction in chapter 3. The results in the previous chapters and the experimental procedures in the present study are briefly summarized in the following section. In section 4.3, the optical transmission spectroscopy of the onions is carried out. Section 4.4 is devoted to the presentation of several theoretical considerations for extinction properties of the onions in order to interpret the experimental results. Furthermore, in section 4.5, we address the correlation between the onions and the interstellar extinction bump at 4.6 μm^{-1}. Conclusion in section 4.6 finally closes the chapter.

4.2 Ultraviolet-Visible Extinction Spectroscopy of Carbon Onions

4.2.1 Experimental procedure

Detailed sample preparation procedure has already been described in the previous chapter. Basically, samples were prepared by annealing diamond nanoparticles 5 nm in diameter [3]. As shown in the chapters 2 and 3, diamond nanoparticles are transformed into spherical

carbon onions by annealing at about 1700 °C. Since the transformation proceeds from the surface to the center in the diamond nanoparticle, there are core-shell type particles, where shells and cores are respectively graphitic layers and diamonds, in an intermediate stage of the transformation. Owing to this formation mechanism, onions about 5 nm in diameter can be prepared from diamond nanoparticles about 5 nm in diameter with narrow size distribution. The previous ESR studies reveled that the graphite shells of spherical onions contain a number of structural defects such as dangling bonds; they have rather defective structure (defective spherical onions) than fullerene-like perfect shells. Under the annealing at temperatures higher than 1900 °C, spherical onions are further graphitized, resulting in the formation of polyhedral onions with facets. The TEM observation at low magnification also showed that the onions clump together into much larger cluster. From the catalog specification of initial diamond nanoparticles, the diameter of clusters is assumed be about 120-140 nm. For the present optical transmittance spectroscopy, we prepare samples annealed at temperatures of between 900 to 2100 °C.

The ultraviolet-visible (UV-Vis.) transmission spectroscopy in the wavelength (λ μm) ranging from 0.2 to 0.6 μm was carried out using double-beam type spectrometer (Shimadz UV-3101PC). Samples were dispersed ultrasonically into the distilled water (about 0.2 mg/cm^3). The water suspension was then put into synthesized quartz cell that is almost transparent in this wavelength region. Another cell filled with only distilled water was used for the reference. The recorded transmittance $T_{(\lambda)}$, where $T_{(\lambda)}$ is the transmittance at the wavelength λ, is converted into the extinction $E_{(\lambda)}$ by the equation, $E = -\log_{10} T$. All of the extinction spectra were normalized by using the following equation [4]

$$NE_{(\lambda)} = [E_{(\lambda)} - E_{(\lambda=0.55)}]/[E_{(\lambda=0.44)} - E_{(\lambda=0.55)}]. \tag{4.1}$$

4.2.2 Ultraviolet-visible extinction spectra

Figure 4.1 shows experimental UV-Vis. extinction spectra. For convenience, the horizontal axis was converted into the wavenumber ($1/\lambda$ μm^{-1}). A spectrum for initial diamond nanoparticles denoted by "as-pre." increases monotonically to the UV region. The monotonic rising extinction continuum cannot be explained by the intrinsic absorption of the diamond, because the band-edge absorption of the bulk diamond normally starts above 5 μm^{-1}.

As the annealing temperature increases, the extinction at higher wavenumbers decreases. In addition, the sample annealed at 1100 °C shows a broad peak at about 3.7 μm^{-1}. At 1700 °C, the broad peak is more pronounced and slightly shifted to a higher wavenumber about 3.9 μm^{-1}. It is worth noticing here that defective spherical onions are observed by TEM around these temperatures. The peak around 3.9 μm^{-1} at 1700

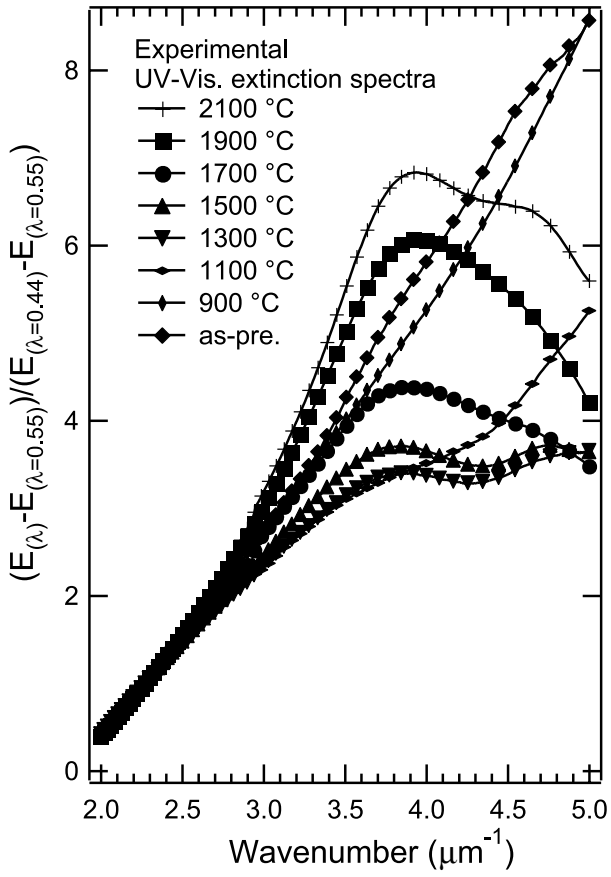

Figure 4.1: UV-Vis. extinction spectra for the samples annealed at various annealing temperatures.

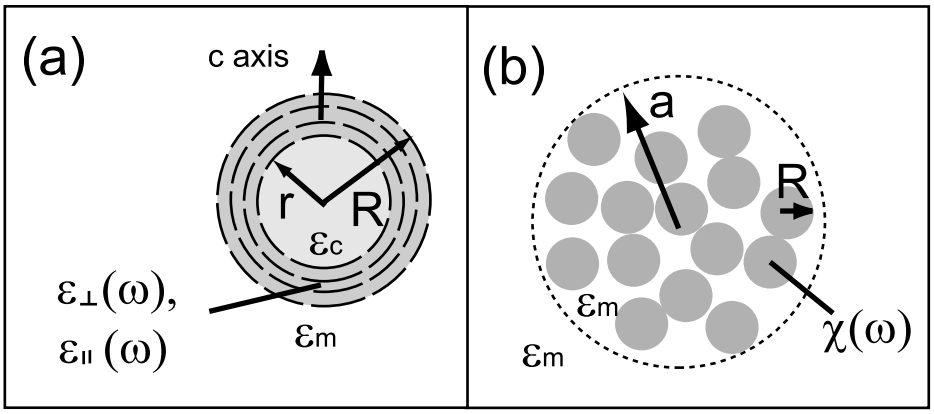

Figure 4.2: Schematic illustrations of (a) a defective spherical onion and (b) a spherical aggregate of the onions.

°C is thus due to the defective spherical onions. With further increasing the annealing temperature, an additional peak at about 4.6 μm^{-1} emerges and the spectrum at 2100 °C exhibits two peaks. The appearance of the double peak is believed to be associated with the formation of polyhedral onions with facets.

In the next section, we will consider theoretically the optical extinction properties of the onions, and address the following features in the experimental spectra: 1. the rising extinction continuum for initial diamond nanoparticles, 2. the broad extinction peak at about 3.9 μm^{-1} for defective spherical onions, 3. the two peaks at 3.9 and 4.6 μm^{-1} for polyhedral onions.

4.3 Theoretical Considerations for the Extinction Spectra of Carbon Onions

4.3.1 Defective spherical onion model

The absorption spectra for carbon onions with diamond or hollow cores have already been calculated by Lucas and co-workers [1, 2]. The spherical coordinates (unit vectors $\mathbf{r}$, θ, ϕ) provide the dielectric tensor of graphitic multishell expressed as

$$\epsilon(\omega) = \epsilon_{\perp}(\omega)(\theta\theta + \phi\phi) + \epsilon_{\parallel}(\omega)\mathbf{rr}, \tag{4.2}$$

where $\omega = 2\pi/\lambda$. $\epsilon_{\perp}(\omega)$ and $\epsilon_{\parallel}(\omega)$ are the components of the dielectric tensor of the graphitic shells in the direction perpendicular and parallel to the c-axis, respectively. As illustrated in Fig. 4.2(a), the spherical onion is composed of outer graphitic shells with

radius R and inner core with radius r. The core, which is filled with diamond or is empty, can be expressed by an isotropic dielectric function of $\epsilon_c(\omega)$. Considering an onion placed in a homogeneous medium with dielectric constant ϵ_m, the multipolar polarizability of order l in the MKSA system of units can be calculated by the following equation

$$\alpha_l(\omega) = 4\pi\epsilon_0 R^{2l+1} \frac{\epsilon_m[(\epsilon_\parallel u_- - \epsilon_c l)(\epsilon_\parallel u_+ - \epsilon_m l) - \rho_l(\epsilon_\parallel u_+ - \epsilon_c l)(\epsilon_\parallel u_- - \epsilon_m l)]}{(l\epsilon_c - \epsilon_\parallel u_+)[\epsilon_\parallel u_- + \epsilon_m(l+1)]\rho_l - (l\epsilon_c - \epsilon_\parallel u_-)[\epsilon_\parallel u_+ + \epsilon_m(l+1)]}, \tag{4.3}$$

where $u_\pm = 0.5\{-1 \pm [1+4l(l+1)\epsilon_\perp(\omega)/\epsilon_\parallel(\omega)]^{1/2}\}$, $\rho_l = (r/R)^{u_+ - u_-}$. ϵ_0 is the permittivity of vacuum. This expression depends on the radius ratio r/R and, of course, the input dielectric functions. At the non-retarded limit, where the diameter of the sphere is so small compared with the wavelength that the retardation effects in the particle can be negligible, the electric field of plane-wave electromagnetic radiation with frequency ω only induces an electric dipole ($l = 1$) which absorbs energy from the wave with the cross section $\sigma(\omega)$. The $\sigma(\omega)$ is directly given by the imaginary part of $\alpha_{l=1}(\omega)$ of the multishell according to

$$\sigma(\omega) = \frac{4\pi\omega}{c} Im[\alpha_{l=1}(\omega)], \tag{4.4}$$

where c is the velocity of light.

In reference [2] by Henrard *et al.*, the dielectric functions of graphitic shells ($\epsilon_\perp(\omega)$ and $\epsilon_\parallel(\omega)$) were set to those of bulk graphite which depend on the crystalographic orientations ($\epsilon_{g\perp}(\omega)$ and $\epsilon_{g\parallel}(\omega)$). However, the graphitic shells of spherical onions prepared from diamond nanoparticles contain a number of defect as already mentioned in chapter 2. To take the effects of defects into the considerations, $\epsilon_\perp(\omega)$ and $\epsilon_\parallel(\omega)$ should be replaced by the dielectric functions of defective graphite. Although the dielectric function could be derived accurately using first-principle approach, such method for defective graphite has not yet been established. Therefore, in the present study, we simply assumed that the dielectric functions of defective graphite shell are the admixtures of dielectric functions of bulk graphite ($\epsilon_{g\perp}(\omega)$, $\epsilon_{g\parallel}(\omega)$) and that of amorphous carbon ($\epsilon_a(\omega)$) as follows

$$\epsilon_\perp(\omega) = c_g\epsilon_{g\perp}(\omega) + (1 - c_g)\epsilon_a(\omega), \tag{4.5}$$

$$\epsilon_\parallel(\omega) = c_g\epsilon_{g\parallel}(\omega) + (1 - c_g)\epsilon_a(\omega), \tag{4.6}$$

where c_g is the concentration of graphite in the defective graphite shells, thus representing the degree of graphitization of the shells. The dielectric functions, $\epsilon_{g\perp}(\omega)$, $\epsilon_{g\parallel}(\omega)$, and $\epsilon_a(\omega)$ used in the present calculations are shown in the Fig. 4.3.

We can calculate here absorption cross section for an isolated defective onion. Figure 4.4 shows computed spectra for the defective onion with R=2.5 nm (5 nm in diameter) in water medium ($\epsilon_m = 1.777$). r/R was varied from 0.96 (curve a) to 0.14 (curve j) by changing r from 2.4 to 0.35 nm. The c_g in all the spectra was set to be of 0.8 because

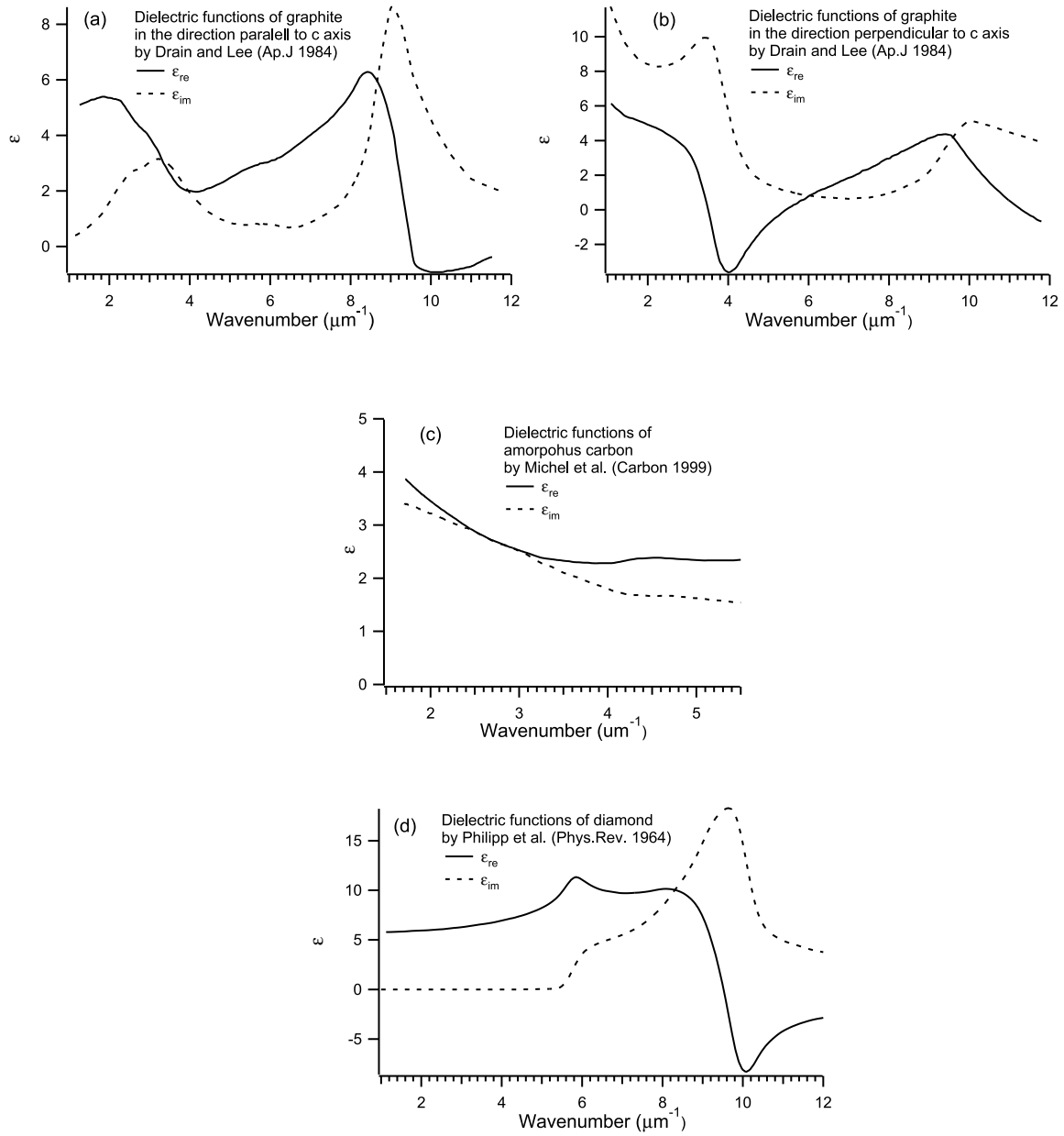

Figure 4.3: Dielectric functions used in the present calculations are shown. Dielectric functions of graphite in the direction (a) perpendicular and (b) parallel to the c axis tabulated by Drain and Lee [5]. (c) Dielectric functions of amorphous carbon tabulated by Michel *et al.* [6]. (d) Dielectric functions of diamond tabulated by Phillip and Taft [7].

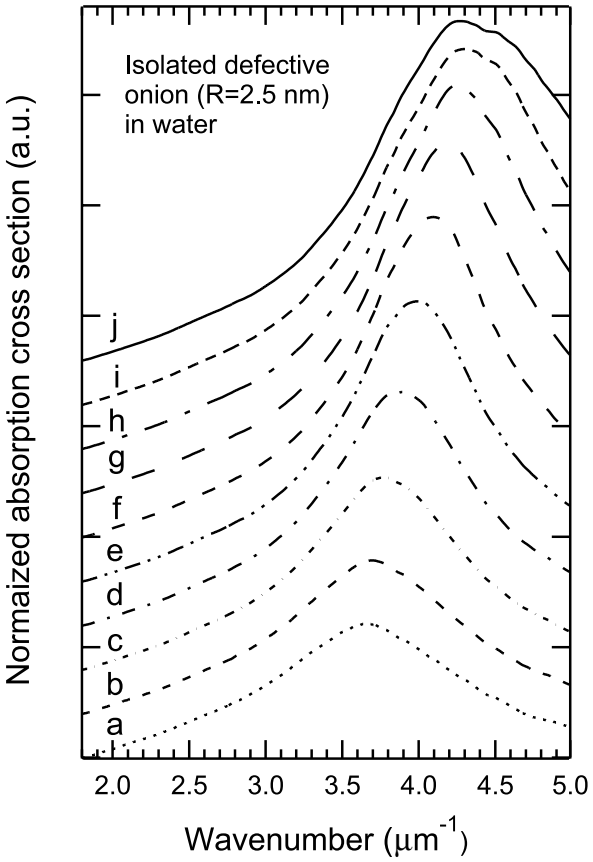

Figure 4.4: Calculated absorption spectra for an isolated defective spherical onion (R=2.5 nm) in water. The r/R are 0.96 (curve a), 0.9 (b), 0.8 (c), 0.7 (d), 0.6 (e), 0.5 (f), 0.4 (g), 0.3 (h), 0.2 (i) , 0.14 (j). For curve j the core is empty, while filled with diamond from curves a to i. c_g is set to be 0.8.

TEM image showed lattice fringes corresponding to (002) planes of graphite. For curve a to i the core is filled with diamond [7] while empty for curve j. The computed absorption cross section was divided by the particle volume (R^3) and then normalized by the Eq. (4.1).

In Fig. 4.4, the diamond nanoparticle with the defective graphite shell 0.1 nm in thickness at the initial stage in the transformation shows a broad absorption peak due to the surface plasmon at about 3.6 μm^{-1} (curve a). With decreasing r/R, i.e, as a diamond nanoparticle is transformed into a defective spherical onion, the peak becomes stronger and sifts to a higher wavenumber. The shift qualitatively agrees with the experimental results. However, the amount of the shift in calculation is larger than that in experimental spectra. The experimental spectrum for defective spherical onions without cores (1700 °C) shows a peak at 3.9 μm^{-1}, whereas the corresponding theoretical one (curve j) at 4.3 μm^{-1}; the peak of the calculated spectrum is located at higher wavenumber than that of experimental one. Additionally, Fig. 4.4 cannot explain the rising continuum in the experimental spectra up to 1100 °C. These misfits between experiments and calculations are believed to be caused by the aggregation effect. Indeed TEM micrographs at low magnification revealed that the onions clump together in much larger particles. The aggregation of the onions by van der Waals force is likely to subsist in water suspension, because the applied ultrasonic dispersion seems to be insufficient to break the adhesion between the particles [1]. It is thus obvious that considerations for the optical extinction by the aggregate of the defective spherical onions is required to explain well the experimental results.

4.3.2 Extinction by the aggregate of defective spherical onions

Here we attempt to calculate the extinction for an aggregate (radius a) of defective spherical onions in water medium. Since the aggregate is composed of the defective spherical onions (radius R) and water as illustrated in Fig. 4.2(b), the aggregate is assumed to have average dielectric function ($\epsilon_{av}(\omega)$). The average dielectric function of the system containing metallic spherical inclusions can be described well by the effective medium theory developed by Maxwell Garnet [8]. In the Maxwell Garnet approach, the interaction between inclusions is treated as the dipole-dipole interaction, and the $\epsilon_{av}(\omega)$ can be expressed as

$$\epsilon_{av}(\omega) = \epsilon_m \frac{3 + 2f\chi(\omega)}{3 - f\chi(\omega)}, \tag{4.7}$$

where ϵ_m is dielectric constant of the host medium in aggregate (water in the present study), f is the onions volume fraction [9]. $\chi(\omega)$ is proportional to the polarizability of the onion of order 1 ($\alpha_1(\omega)$), which has already been calculated in the previous subsection,

as follows

$$\chi(\omega) = \frac{3\alpha_1(\omega)}{4\pi R^3 \epsilon_0 \epsilon_m}. \tag{4.8}$$

Assuming the spherical aggregate of the defective spherical onions, the extinction efficiency of the aggregate having $\epsilon_{av}(\omega)$ can be calculated by the Mie theory described in detail in the standard textbook [10]. By introducing the Riccati-Bessel functions (ψ_n and ξ_n), the Mie coefficients (a_n and b_n) can be expressed as

$$a_n = \frac{[D_n(mx)/m + n/x]\psi_n(x) - \psi_{n-1}(x)}{[D_n(mx)/m + n/x]\xi_n(x) - \xi_{n-1}(x)}, \tag{4.9}$$

$$b_n = \frac{[mD_n(mx)/m + n/x]\psi_n(x) - \psi_{n-1}(x)}{[mD_n(mx)/m + n/x]\xi_n(x) - \xi_{n-1}(x)}, \tag{4.10}$$

where the size parameter x and the relative refractive index m are

$$x = ka = \frac{2\pi N a}{\lambda}, \qquad m = \frac{N_1}{N}. \tag{4.11}$$

N_1 and N are the refractive indices of the aggregate and medium, and thus given by $\sqrt{\epsilon_{av}}$ and $\sqrt{\epsilon_m}$, respectively. $D_n(mx)$ is the logarithmic derivative, which satisfies the recurrence relation

$$D_{n-1}(mx) = \frac{n}{mx} - \frac{1}{D_n(mx) + n/mx}. \tag{4.12}$$

In the present Mie calculation, $D_n(mx)$ is computed by downward recurrence beginning with $0.0 + i0.0$. On the other hands, both $\psi_n(x)$ and $\xi_n(x)$, where $\xi_n(x) = \psi_n(x) - i\rho_n(x)$, satisfy

$$\psi_{n+1}(x) = \frac{2n+1}{x}\psi_n(x) - \psi_{n-1}(x), \tag{4.13}$$

and are computed by upward recurrence relation beginning with $\psi_{-1}(x) = \cos x$, $\psi_0(x) = \sin x$, $\rho_{-1}(x) = -\sin x$, and $\rho_0(x) = \cos x$. As a result, the extinction cross section C_{ext} can be calculated by

$$C_{ext} = \frac{2\pi}{k^2}\sum_{n=1}^{\infty}(2n+1)Re\{a_n + b_n\}. \tag{4.14}$$

Finally, the extinction efficiency Q_{ext} follows from $Q_{ext} = C_{ext}/\pi a^2$.

The calculated extinction spectra for an aggregate of defective spherical onions (R=2.5 nm) in water medium are shown in Fig. 4.5. All of the spectra were normalized by Eq. (4.1). The radius of the aggregate (a) was set to be 0.06 μm same as the catalog specification of initial diamond nanoparticles. The parameters r, R and c_g, i.e., the defective onions used here, were the same as those in Fig. 4.4. Filling factor (f) was set to be of 0.4. Curve a, which is the spectrum for r=2.4 nm and thus corresponds to the diamond nanoparticle in the initial stage of the graphitization, shows rising extinction continuum to UV range with a shoulder at about 3.6 μm^{-1}. This calculated spectrum is very similar

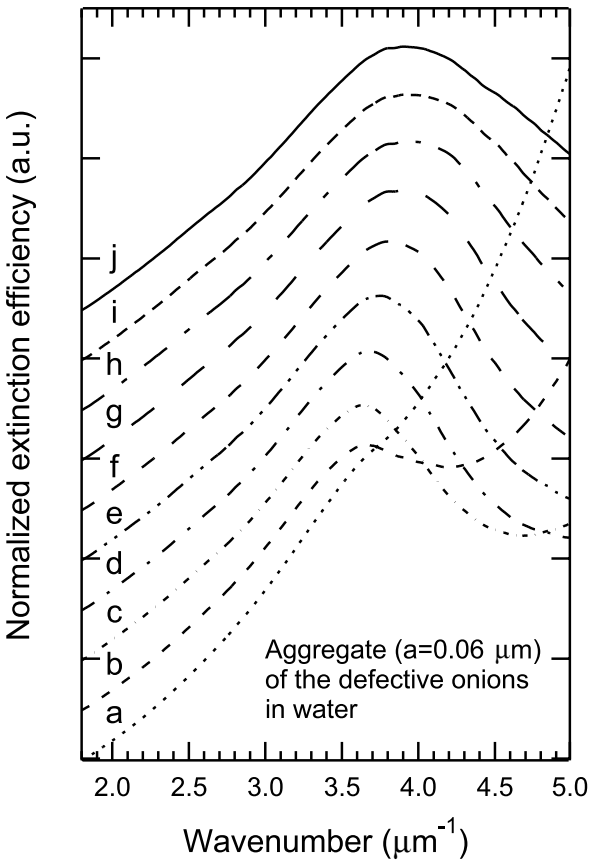

Figure 4.5: Calculated extinction spectra for an aggregate (a=0.06 μm) of defective spherical onions (R=2.5 nm) in water. The parameters used for the defective onions are the same as those in Fig. 4.4.

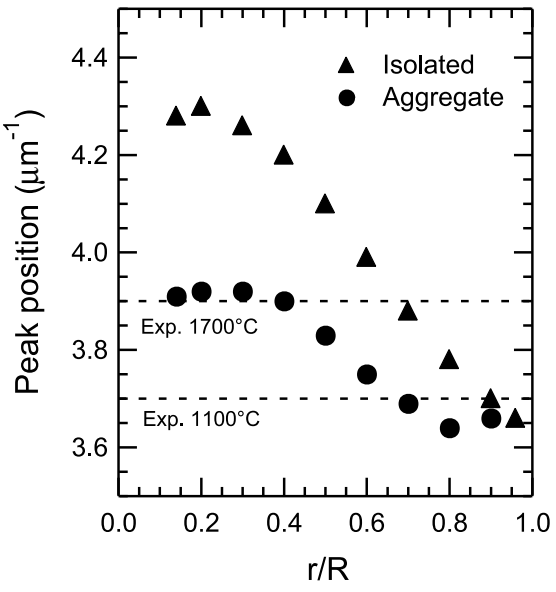

Figure 4.6: Peak positions of the isolated defective spherical onion (triangle) and their aggregate (circle) are plotted as a function of r/R.

to the experimental one for the sample annealed at 1100 °C. The similarity allows us to suggest that the rising continuum in the experimental spectrum for diamond nanoparticles can be explained by the Mie scattering by an aggregate of diamond nanoparticles coated with very thin amorphous or graphitic layers, which are shown in the previous TEM observations.

Figure 4.5 shows that the transformation from diamond nanoparticles into defective onions is accompanied by an increase in the intensity of the extinction peak at 3.6 μm^{-1} and a slight shift to a higher wavenumber; the peak finally reaches at 3.9 μm^{-1}. In Fig. 4.6, the peak positions of the spectra in Figs. 4.4 and 4.5 are plotted as a function of r/R. We should recall here that the extinction peaks of the experimental spectra shifted from 3.7 to 3.9 μm^{-1} by annealing up to 1700 °C, i.e., by transformation from diamond nanoparticles into defective spherical onions. This shift variation in the experimental results is also given in Fig. 4.6. Figure 4.6 shows that the peak position of the aggregate weakly depends on the r/R, bringing about a smaller variation with r/R for the aggregate than that for the isolated defective onion. As a result, the aggregate of defective onions successfully reproduces the experimental peak energy. These results clearly demonstrate that the optical extinction properties of the onions transformed from diamond nanoparticles can be explained well by the defective spherical onion model.

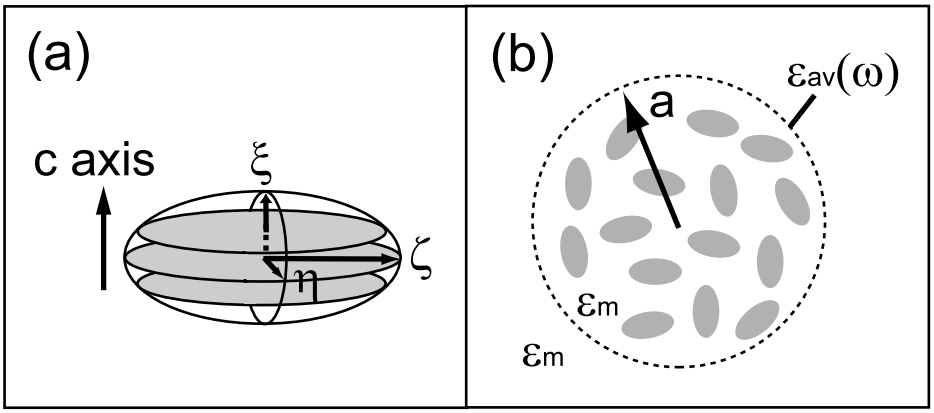

Figure 4.7: Schematic illustrations of (a) an ellipsoidal graphite with the crystalline anisotropy and the axis configurations, and (b) a spherical aggregate of the graphite ellipsoids.

4.3.3 Extinction by the aggregate of polyhedral onions

In experimental spectra above 1900 °C shown in Fig. 4.1, the appearance of two extinction peaks is apparently attributed to the formation of the aggregate consisting of polyhedral onions with facets. To consider the extinction properties of polyhedral onions, we use a different theoretical scheme from that used for spherical onions. In this study, we simply assume the facets of a polyhedral onion as planar graphite nanocrystals. Such a nanocystal is treated as an ellipsoidal graphite with crystalline anisotropy as shown in Fig. 4.7(a). The aggregate of polyhedral onions dispersed in water are thus modeled as a system consisting of anisotropic graphite ellipsoids that are randomly oriented in water [Fig. 4.7(b)]. We can here adopt a framework of Maxwell Garnet type average dielectric function for anisotropic ellipsoids developed by Hayashi *et al.* [11]. For an ellipsoidal particle, ξ, η, and ζ axes are set as shown in Fig. 4.7(a). Dielectric functions along each axis are expressed by ϵ_ξ, ϵ_η, and ϵ_ζ. Introducing depolarization factors ($L_j, \quad j = \xi, \eta, \zeta$) along j axis and filling factor (f), the average dielectric function can be described as

$$\epsilon_{av} = 1 + \frac{3(1-f)(\epsilon_m - 1) + f(\tilde{\epsilon_\xi} + \tilde{\epsilon_\eta} + \tilde{\epsilon_\zeta})}{3(1-f) + f(\hat{\epsilon_\xi} + \hat{\epsilon_\eta} + \hat{\epsilon_\zeta})}, \tag{4.15}$$

where

$$\sum_j L_j = 1 \qquad (j = \xi, \eta, \zeta), \tag{4.16}$$

$$\hat{\epsilon_j} = [1 + L_j(\epsilon_j/\epsilon_m - 1)]^{-1} \qquad (j = \xi, \eta, \zeta), \tag{4.17}$$

$$\tilde{\epsilon_j} = (\epsilon_j - 1)\hat{\epsilon_j} \qquad (j = \xi, \eta, \zeta). \tag{4.18}$$

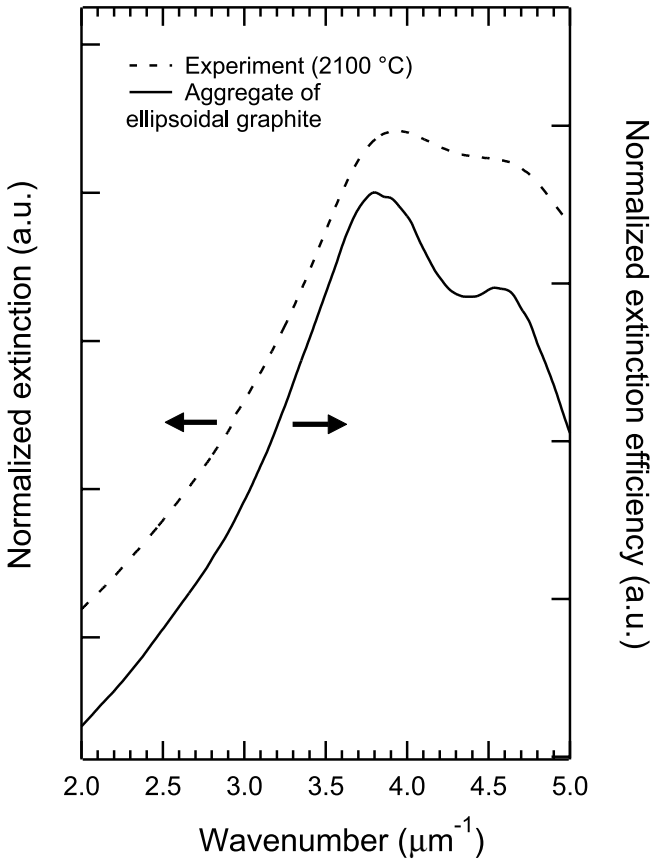

Figure 4.8: Solid line represents a computed spectrum for an aggregate of anisoropic ellipsoidal graphite nanocrystals. The ellipsoidal nanographite model can reproduce successfully the experimental spectrum for polyhedral onions at 2100 °C (dashed line).

Using ϵ_{av} derived from Eq. (4.15), we can calculate the extinction efficiency for an aggregate of polyhedral onions by the Mie theory using Eq. (4.14). ξ axis of the ellipsoid was set to parallel to the graphite c axis as shown in Fig. 4.7(a). Therefore, ϵ_ξ corresponds to $\epsilon_{g\parallel}(\omega)$, while ϵ_η and ϵ_ζ to $\epsilon_{g\perp}(\omega)$. For depolarization factors, by assuming rotational ellipsoid, we set $L_\xi = L_\eta$ and $2L_\xi + L_\zeta = 1$.

Solid line in Fig. 4.8 shows a calculated extinction efficiency for an aggregate of graphite ellipsoids in water. The radius of the aggregate (a) was set to be 0.06 μm. L_ζ was 0.1, and L_η and L_ξ were 0.45. The filling factor f was set to be 0.2. The computed spectrum was normalized by Eq. (4.1). The aggregate of ellipsoidal graphite nanoparticles that we considered here accounts for an extinction spectrum with two peaks at 2100 °C (dashed line in Fig. 4.8). These two peaks at 3.9 and 4.6 μm^{-1} are induced by surface plasmons along η and ζ axis of rotational ellipsoid.

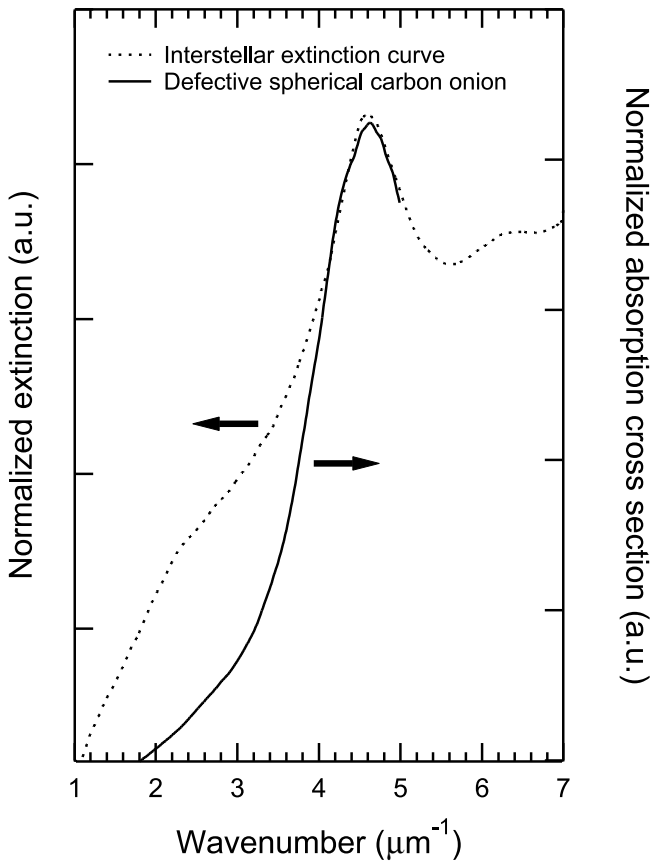

Figure 4.9: Comparison between simulated spectrum for the isolated defective onion in vacuum (solid line) and interstellar extinction curve (dashed line) reported by Savage and Mathis [12].

4.4 Defective Carbon Onion as a Possible Origin of Interstellar Absorption Bump

Our defective spherical onion model now allows us to simulate the extinction spectrum of the onions in interstellar space. In relation with this astrophysical context, we should consider the extinction by an isolated onion in vacuum, because the interstellar dust particles having a size in the 1-20 nm range are usually supposed not to clump together. For particles of nanoscopic sizes, scattering in the UV region is negligible and contribution to the extinction curve is dominated by absorption [1, 10].

The solid line in Fig. 4.9 shows the normalized simulation result for a defective spherical onion with R=2.5 nm having a hollow core with r=0.35 nm, i.e., the defective onion, of which the aggregate reproduced well the experimental spectrum at 1700 °C. The onion is placed in vacuum. The simulated spectrum reveals an absorption bump at 4.6 μm^{-1}.

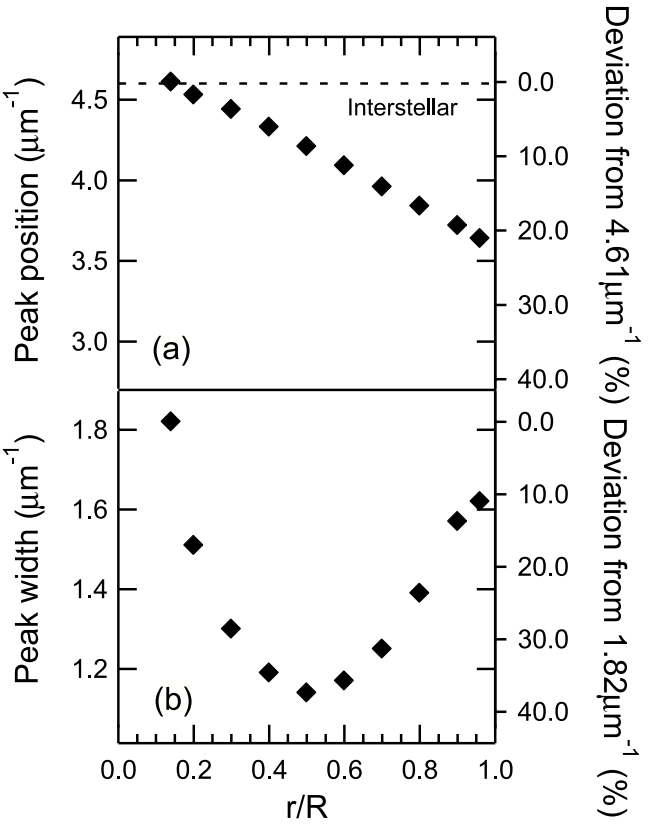

Figure 4.10: Peak position (a) and peak width (b) for an isolated defective spherical onion in vacuum are plotted as a function of r/R.

The observed interstellar extinction curve reported by Savage and Mathis [12] is shown as the dashed line in the same figure. The broad feature between 2-3 μm^{-1} in the observed data is considered to originate from astronomical silicate. Comparison between simulated and observed spectra in Fig. 4.9 clearly demonstrates that, even if without coating material, the defective spherical onion reproduces well the interstellar absorption bump at 4.6 μm^{-1} in terms of both peak position and width. The present onion model reproduces a decrease in the resonance width by increasing r (r/R). Figures 4.10(a) and 4.10(b) respectively show the peak position (x_0) and width (γ) plotted as a function of r/R. The x_0 and γ were obtained by fitting the numerical data with the Drude function given in reference [13]

$$\sigma(x) = a_1 + a_2 x + a_3 \frac{x^2}{(x^2 - x_0^2)^2 + \gamma^2 x^2}, \tag{4.19}$$

where x is the energy and a_1, a_2, a_3, x_0, and γ are the fitting parameters. Figure 4.10 shows that changing r/R from 0.14 to 0.4 brings about a large variation in the peak width

(about 35 %) despite the slight redshift in the position (about 6 %).

Here we turn to discuss the possibility for the existence of spherical carbon onions transformed from diamond nanoparticles in the interstellar space. Diamonds have been suggested to exist in interstellar space [14]. Indeed, sp^3-bonded carbon has been detected in dense clouds surrounding star formation regions [15] and several carbonaceous chondrites contain tiny diamonds several nm in diameter [16, 17]. It has been claimed that the low-pressure gas phase formation, like chemical vapor deposition (CVD), of diamond nanoparticles is considered to be an allowed process in a hydrogen rich interstellar sources [14, 16, 18].

The question is how these diamonds are transformed into the onions in the interstellar space. The thermal energy is the first explanation for the driving force as shown in the present experiment. The graphitization of very small diamond nanoparticles ($\sim$ 2 nm) starts at rather low temperature around 900 °C than large particles or bulk diamond, but many surviving pre-solar materials including diamonds are considered to be never exposed to temperature above 700 °C [19]. Another plausible account is the irradiation by high-energy particles [20, 21]. The long-term bombardment by electrons, ions, or atoms, which are abundant in the molecular cloud, induces the graphitization of diamond nanoparticles, resulting in the formation of spherical onions in interstellar space. Such onions are considered to have defective structure. It is thus concluded that defective spherical carbon onions as shown in Fig. 4.2(a) can be formed in the interstellar space and very much likely to be a carrier of the interstellar extinction bump at 4.6 μm^{-1}. The present study showed that the correlation between the absorption peak width and r/R, implying that the peak width should reflect the degree of the transformation into the onions. A variety of formation histories of the onions brings about the large variation in the peak width along different lines of sight in the interstellar space. The present study demonstrates that interstellar dust particles might be duplicated by the defective spherical carbon onions in the laboratory. This open the way to address experimentally to another open questions in the astronomy and astrophysics, such as unidentified infrared emission bands [22].

4.5 Conclusion

We have studied optical extinction properties of the carbon onions prepared from diamond nanoparticles. Experimental extinction spectra of the spherical and polyhedral onions were acquired by UV-Vis. optical transmission spectroscopy. In order to interpret the experimental results, we carried out theoretical considerations for the extinction properties of the onions. For spherical onions, experimental spectra show an extinction peak around

3.9 μm^{-1}. Theoretical considerations demonstrated that the experimental results are explained well by the aggregate of the defective spherical onions. For polyhedral onions, experimental spectrum exhibits two peaks at 3.9 and 4.6 μm^{-1}. The spectrum with double peak can be reproduced successfully by assuming the aggregate of polyhedral onions as that of graphite ellipsoids with crystalline anisotropy. Furthermore, we address the contribution of the onions to the interstellar extinction bump at 4.6 μm^{-1}. The theoretical simulation based on our defective spherical onion model allows us to suggest that the defective spherical onion is a strong candidate for the carbonaceous interstellar dust giving rise to the extinction bump at 4.6 μm^{-1}.

References

[1] A. A. Lucas, L. Henrard, and Ph. Lambin, Phys. Rev. B **49**, 2888 (1994).

[2] L. Henrard, Ph. Lambin, and A. A. Lucas, Astrophys. J. **487**, 719 (1997).

[3] V. L. Kuznetsov, A. L. Chuvilin, Y. V. Butenko, I. Y. Mal'kov, and V. M. Titov, Chem. Phys. Lett. **222**, 343 (1994).

[4] J. S. Mathis, Annu. Rev. Astron. Astrophys. **28**, 37 (1990).

[5] B. T. Drain and H. M. Lee, Astrophys. J. **285**, 89 (1984).

[6] B. Michel, Th. Henning, C. Jäger, and U. Kreibig, Carbon **37**, 391 (1999).

[7] H. R. Phillip and E. A. Taft, Phys. Rev. **136**, A1445 (1964).

[8] J. C. Maxwell Garnet, Philos. Trans. R. Soc. London **203**, 385 (1904).

[9] H.G. Craighead and A. M. Glass, Opt. Lett. **6**, 248 (1981).

[10] C. F. Bohren and D. R. Huffman, *Absorption and scattering of light by small particles* (John Wiley & Sons, New York, 1983).

[11] S. Hayashi, N. Nakamori, and H. Kanamori, J. Phys. Soc. Jpn. **46**, 176 1979.

[12] B. D. Savage and J. S. Mathis, Annu. Rev. Astron. Astrophys. **17**, 73 (1979).

[13] E. L. Fitzpatrick and D. Massa, Astrophys. J. Suppl. **72**, 163 (1990).

[14] E. D. Anders and E. Zinner, Meteoritics **28**, 490 (1993).

[15] L. J. Allamandola, S. A. Sandford, A. G. G. M. Tielens, and T. M. Herbst, Science **260**, 64 (1993).

[16] R. S. Lewis, M. Tang, J. F. Wacker, E. Anders, and E. Steel, Nature **326**, 160 (1987).

[17] D. F. Blake, F. Freund, K. F. M. Krishnan, C. J. Echer, R. Shipp, T. E. Bunch, A. G. Tielens, R. J. Lipari, C. J. D. Hetherington, and S. Chang, Nature **332**, 611 (1988).

[18] D. Ugarte, Astrophys. J. **443**, L85 (1995).

[19] J. A. Nuth, Nature **318**, 166 (1985).

[20] D. Ugate, Nature **359**, 707 (1992).

[21] L-C. Qin and S. Iijima, Chem. Phys. Lett. **262**, 252 (1996).

[22] W. W. Duley, Astrophys. J. **553**, 575 (2001).

Part II

Fabrication and Physical Properties of Filled Carbon Nanocapsule Systems

Chapter 5

Structure and Formation Mechanism of Magnetic-Metal Filled Carbon Nanocapsules

5.1 Introduction

As already described in Chapter 1, a fabrication method of size-controlled carbon nanocapsules with thickness-controlled graphitic coating via solid state reaction is desired to open the way to the application of filled carbon nanocapsules. In this chapter, we report a new and simple method for synthesizing Co, Ni and Fe nanoparticles coated with thin layers of graphite (Co, Ni, and Fe filled carbon nanocapsules). The method used is the heat treatment of the mixture of magnetic-metal nanoparticles about 30 nm in diameter and diamond nanoparticles about 5 nm in diameter. Transmission electron microscopy (TEM) shows that, after the heat treatment at 1700 °C, all the magnetic-metal nanoparticles were encapsulated with uniform thin graphitic layers. The thickness of the coating was nearly the same as the diameter of the initial diamond nanoparticles. These results imply that diamond nanoparticles being in contact with the metals are transformed into the thin graphitic coating.

Moreover, we intend to clarify the formation mechanism of Co filled carbon nanocapsules by *in-situ* TEM, x-ray diffraction (XRD) and Raman studies. In the initial mixture, surface oxidized β-Co nanoparticles about 30 nm in diameter are surrounded by diamond nanoparticles about 5 nm in diameter. The Raman study indicates that the surface native oxide (Co_3O_4) is reduced to metallic Co as the heat treatment temperature increases. The reduction is accompanied by the drastic progress of graphitization of diamond nanoparticles. The result supports our hypothesis that diamond nanoparticles being in contact with metallic Co are transformed into graphitic coating. Direct observation by *in-situ*

TEM demonstrates that the graphitic coating is formed not on a cooling but on a heating process. Once the coating is completely formed, the number of the graphitic layers is almost constant on further heating and cooling. These results brought by *in-situ* TEM studies cannot be explained within the framework of the dissolution-precipitation mechanism. We thus propose a metal-template graphitization mechanism, in which metallic Co particles simply act as templates for the coating.

5.2 Experiment

Fe-group magnetic-metal filled carbon nanocapsules were prepared by the heat treatment of the mixture of magnetic-metal and diamond nanoparticles. Diamond nanoparticles about 5 nm in diameter were mixed with the metal nanoparticles about 30 nm in diameter using ultrasonic dispersion. Both of the nanoparticles were commercially available. The mixture was put in a hole (2.5 mm in diameter) which was drilled through a graphite rod (5 mm in diameter and 7 mm in length). The graphite rod was then heat-treated at the temperatures ranging from 300 to 800 °C in vacuum ($< 2 \times 10^{-3}$ Pa) in a conventional electric furnace, and from 800 to 1700 °C by an electron beam irradiation in vacuum ($< 2.5 \times 10^{-3}$ Pa).

TEM studies were performed with JEOL JEM-2010 and Hitachi HF-2000 transmission electron microscopes at an acceleration voltage of 200 kV. For the *in-situ* observation, the sample was placed on a W filament, which was attached to the sample holder, and resistively heated. The temperature of the sample was roughly estimated from the current, which is supplied to a W filament, by using a calibration curve obtained from standard samples (Au). An XRD measurement was performed with an x-ray diffractometer [RINT-2100 (RIGAKU)] with the Cu K_α radiation. Raman spectroscopy was carried out with a SPEX 1877 Triplemate equipped with a charge coupled device. Spectra were recorded in a 90° scattering geometry. The excitation source was the 514.5 nm line of an Ar-ion laser. The excitation power was kept less than 10 mW in order to avoid local heating. Differential scanning calorimetry (DSC) was performed with a RIGAKU DSC-8230. The samples were filled with a Pt cell and then put into a chamber filled with N_2 gas. The temperature increasing speed during the measurements was 10 °C/min. α-Al_2O_3 was used as a reference sample.

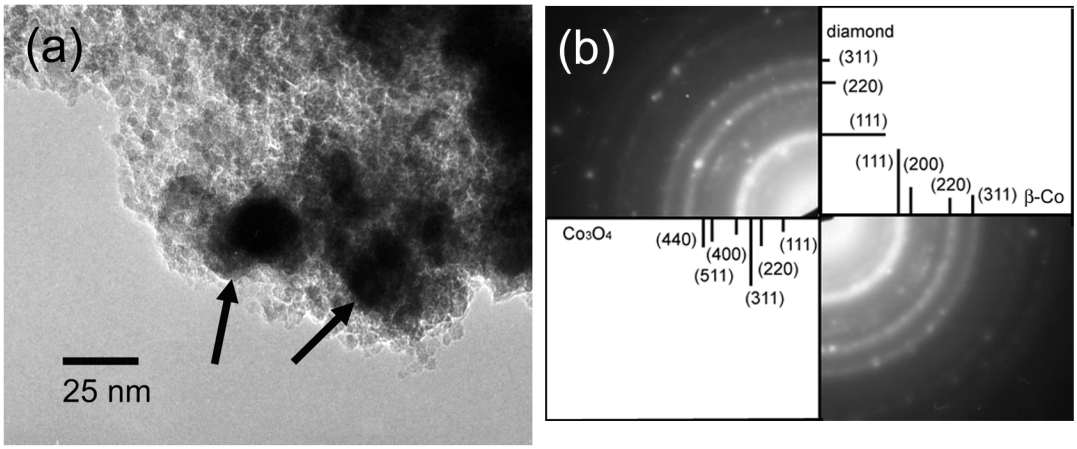

Figure 5.1: A TEM image (a) and an SAED pattern (b) of the initial mixture of Co and diamond nanoparticles. Co nanoparticles about 30 nm in diameter (indicated by arrows) are surrounded by diamond nanoparticles about 5 nm in diameter.

5.3 Results and Discussion

5.3.1 Formation of Co, Ni, Fe filled carbon nanocapsules

Figures 5.1(a) and 5.1(b) respectively show a TEM image and a selected-area electron diffraction (SAED) pattern of the mixture of Co and diamond nanoparticles before the heat treatment. Figure 5.1(b) also exhibits diffraction patterns calculated from ASTM data [1] for β-Co with a face-centered cubic (fcc) structure, Co_3O_4 and diamond; the length of the bars represents diffraction intensity. The SAED pattern indicates that the initial mixture consists of β-Co, Co_3O_4 and diamond. Co_3O_4 is a native oxide formed on the surface of Co nanoparticles [2]. The presence of Co_3O_4 as well as β-Co in the initial Co nanoparticles is also confirmed by an XRD study as shown in Fig. 5.2(a). Therefore, dark patches in Fig. 5.1(a) (indicated by arrows) correspond to β-Co nanoparticles with surface oxides, and the surroundings are diamond nanoparticles about 5 nm in diameter. The fcc structure is the high temperature phase for Co, and normally presents only above 420 °C. The presence of the high temperature phase at room temperature is probably due to the small particle nature of the material and/or "quenching" effects [3].

Figure 5.3 shows the heat treatment temperature dependence of Raman spectra. Before heat treatment (curve *a*), the spectrum exhibits a weak Raman band at about 1325 cm^{-1} which originates from diamond nanoparticles (indicated by an arrow). The band is slightly shifted toward a lower frequency compared with that for the bulk diamond (1332 cm^{-1}). This shift is explained by the phonon confinement effects [4, 5, 6]. In

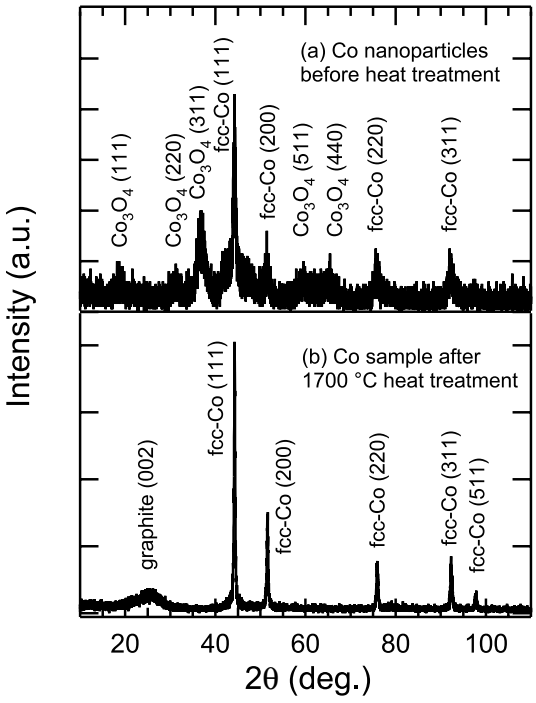

Figure 5.2: XRD profiles of initial Co nanoparticles before heat treatment (a) and the mixture of Co and diamond nanoparticles after the heat treatment at 1700 °C (b).

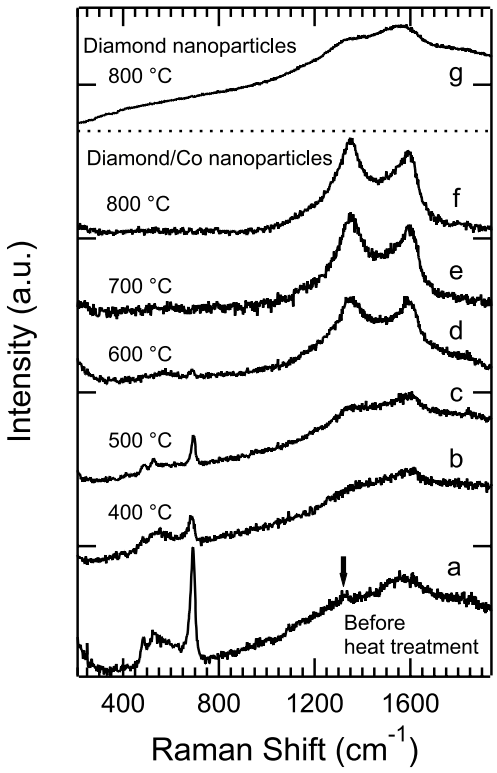

Figure 5.3: Raman spectra obtained from initial mixture (curve a) and samples with different heat treatment temperatures (curves b-f). The top curve g represents a Raman spectrum of the diamond nanoparticles heat-treated at 800 °C without Co nanoparticles.

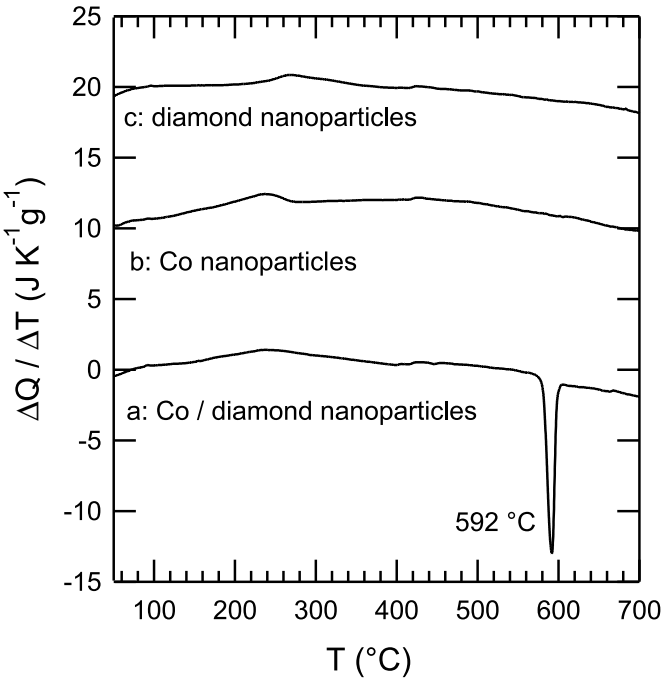

Figure 5.4: DSC results up to 700 °C for a mixture of Co and diamond nanoparticles (curve *a*), Co nanoparticles (curve *b*), and diamond nanoparticles (curve *c*). Only the mixture of Co and diamond nanoparticles shows an endothermic peak at 592 °C, which is due to the reduction of Co_3O_4.

addition to the diamond band, a broad band can be seen at a higher wavenumber region. The broad band is thought to originate from the surface amorphous carbon layers of the diamond nanoparticles [6]. The spectrum *a* also shows three Raman bands at about 483, 523, and 691 cm^{-1}. These bands are attributed to Co_3O_4 [7].

The carbon-related features above 1200 cm^{-1} do not change up to the heat treatment temperature of 500 °C (curves *b* and *c*). In contrast, the Co_3O_4 bands become weaker, suggesting that Co_3O_4 is reduced to metallic Co with increasing the heat treatment temperature. The Co_3O_4 bands almost disappear at 600 °C (curve *d*). The reduction of Co_3O_4 is confirmed also by DSC. Figure 5.4 shows DSC results for a mixture of Co and diamond nanoparticles (curve *a*), Co nanoparticles (curve *b*), and diamond nanoparticles (curve *c*). The vertical axis was calibrated using a standard sample (Pb). The mixture of Co and diamond nanoparticles (curve *a*) exhibits an endothermic peak at 592 °C. The endothermic peak is believed to be caused by a reduction of Co_3O_4 because the reduction is an endothermic reaction as described by Eq. (5.1).

$$Co_3O_4 + 2C_{(diamond)} = 3Co + CO_2 - 119\ kJ \qquad (5.1)$$

It is worth noticing in Fig. 5.4 that curve *b* for Co nanoparticles without diamonds shows no peaks up to 700 °C. Since Co_3O_4 is normally stable around 600 °C, diamond nanoparticles may act as a reducing agent in the present chemical reaction.

The disappearance of Co_3O_4-related Raman bands at 600 °C is accompanied by the drastic change in carbon-related Raman features; the band due to the graphitic structure (*G* band) at about 1580 cm^{-1} and disorder-induced band (called *D* band) at about 1350 cm^{-1} emerge. This implies that when the reduction of Co_3O_4 is completed, the graphitization of diamond nanoparticles starts. The reduction of surface Co_3O_4 layers allows diamond nanoparticles to directly contact with metallic Co particles. The direct contact enables diamond nanoparticles to be transformed into graphitic coating owing to the catalytic effect of metallic Co for graphitization [8, 9]. The top curve *g* in Fig. 5.3 represents a spectrum of the diamond nanoparticles annealed at 800 °C without mixing with Co particles. The carbon-related features are smeared and very similar to those in curves *b* and *c*, suggesting that, without Co nanoparticles, graphitization does not proceed even at 800 °C. This is in good agreement with the DSC result for diamond nanoparticles without Co (curve *c* in Fig. 5.4), which does not exhibit peaks up to 700 °C.

Figure 5.2(b) shows the XRD profile for the sample heat treated at 1700 °C. A broad diffraction peak at about 26.3 ° can be assigned to the (002) planes of hexagonal graphite structure. In addition to the peak at 26.3 °, we can see five sharp peaks. By comparing with the ASTM data, the peaks at 44.3 °, 51.6 °, 75.9 °, 92.3 ° and 97.7 ° can be identified to the (111), (200), (220), (311) and (222) planes of β-Co with a face-centered cubic (fcc) structure, respectively. It has been already reported that β-Co is a high-temperature phase of Co [10].

Figure 5.5(a) shows a TEM image for the sample heat-treated at 1700 °C. Nanocapsules about 65 nm in diameter with thin coating can be seen. Figure 5.5(b) shows a high-magnification image of Fig. 5.5(a). The image shows that the thickness of the coating is uniform and around 3 nm. The spacing of the lattice fringes of the coating is around 0.34 nm, which is close to that of the graphite (002) planes. We can also observe carbon onions on the graphitic coating. The thickness of the coating almost the same as the average diameter of diamond nanoparticles and the existence of the onions on the coating suggest that the diamond nanoparticles being in contact with Co are transformed into the graphitic coating.

We performed the same experiments for Ni nanoparticles and Fe nanoparticles. A TEM image of the Ni sample after annealing at 1700 °C [Fig. 5.6(a)] shows a particle around 50 nm in diameter. The whole surface is coated with a uniform graphitic layer about 3 nm in thickness. Figure 5.7(a) shows the XRD profile for Ni sample after 1700 °C annealing. Diffraction peaks above 40 ° can be assigned to Ni with a fcc structure. In

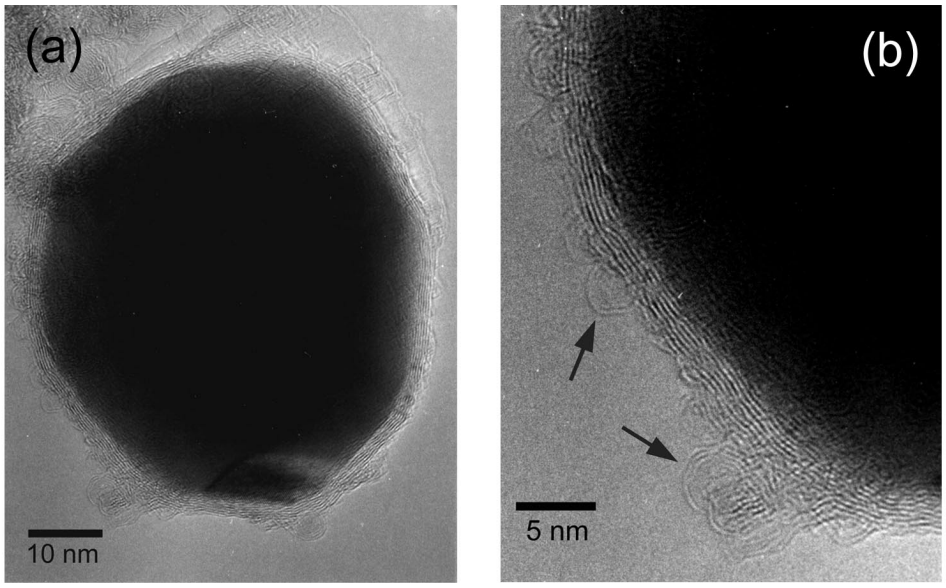

Figure 5.5: (a) A typical TEM image of a Co filled carbon nanocapsule formed after heat treatment at 1700 °C. (b) High magnification image of a part of the nanocapsule.

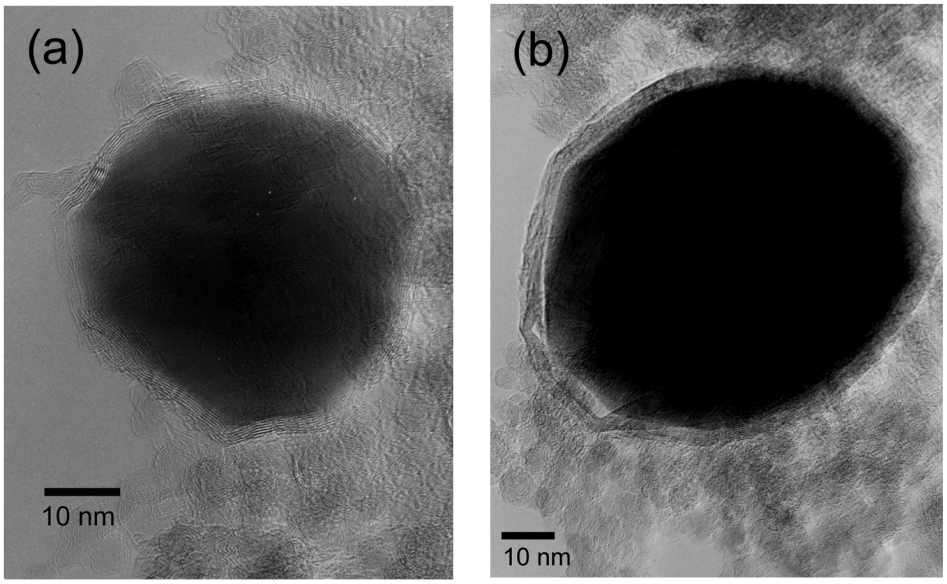

Figure 5.6: Typical TEM images of the nanocapsules after 1700 °C annealing; (a) Ni sample and (b) Fe sample.

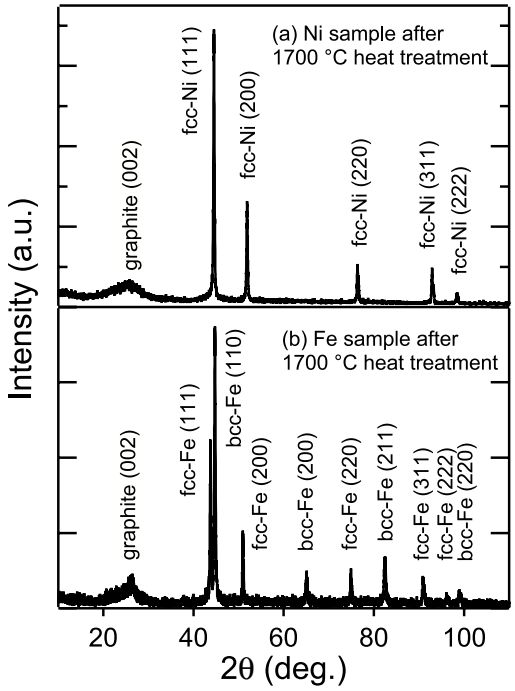

Figure 5.7: X-ray diffraction profiles of the samples after 1700 °C annealing; (a) Ni sample and (b) Fe sample.

the Fe sample [Fig. 5.6(b)], a particle around 80 nm in diameter with the uniform coating about 3 nm in thickness can be seen after 1700 °C annealing. In the XRD profile of the Fe sample after 1700 °C annealing [Fig. 5.7(b)], the diffraction patterns above 40 ° can be interpreted as the superposition of those of α-Fe with a body-centered cubic structure and γ-Fe with a fcc structure (Austenite). Consequently, we found that all the particles observed for Ni and Fe samples were uniformly coated and the thickness of the coating was almost the same.

These results of TEM, SAED, XRD, DSC and Raman studies revealed that diamond nanoparticles being in contact with metallic particles are transformed into graphitic coating, resulting in the formation of metal filled carbon nanocapsules. Nevertheless, the formation mechanism of the graphitic coating, particularly the role of metals, is still unclear. In order to gain more detailed information about the formation mechanism, we performed *in-situ* TEM experiments for Co samples.

5.3.2 Formation mechanism of filled carbon nanocapsules

The initial mixture of Co and diamond nanoparticles was put into the microscope and the sample temperature was gradually increased by increasing the current supplied to a

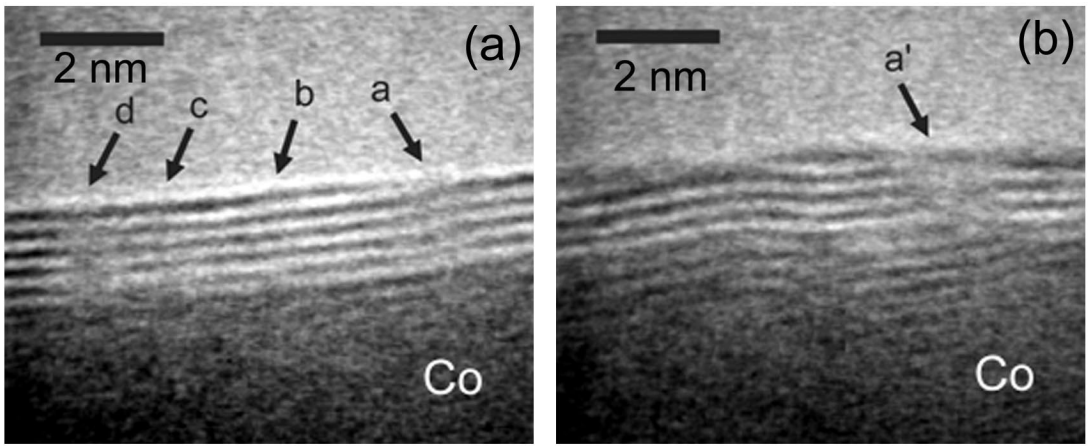

Figure 5.8: (a) An *in-situ* TEM image of the coating on heating process. The coating consists of 6 or 7 graphitic layers. The micrograph also shows defects as indicated by arrows *a*, *b*, *c*, and *d*. (b) An *in-situ* TEM image on cooling process at the same place as in (a). Note that the number of the layers on cooling is almost the same as that on heating although the crystallinity is much different.

W filament (heating process). The lattice fringes due to Co oxide disappeared above 600 °C, and then the graphitic coating of the nanocapsules is formed. Figure 5.8(a) shows a *in-situ* TEM image of a part of the coating during the heating process. The temperature of the sample was estimated to be about 1100 °C. Clear lattice fringes corresponding to (002) planes of graphite can be seen. The coating consists of 6 or 7 graphitic layers and is about 2 nm in thickness. Once the coating was completely formed, the number of graphitic layers was found to be almost constant on further heating. Figure 5.8(a) also shows that the coating has defects as indicated by arrows *a*, *b*, *c*, and *d*.

After heating up to 1100 °C, we gradually decreased the sample temperature by decreasing the current (cooling process). Upon cooling, Fig. 5.8(b) was obtained at the same place as in Fig. 5.8(a); the point a' is the same place as the point a in Fig. 5.8(a). Note here that the number of the layers on cooling is almost the same as that on heating. However, the crystallinity of the graphitic coating is much different. The coating becomes disordered and is similar to turbostratic carbon that is made up of small segments of graphitic sheets stacked roughly parallel to the particle surface. The disorder is thought to be induced by the different heat-expansion coefficient between Co and graphite.

From these results of *in-situ* TEM experiments, we will discuss here the formation mechanism of the graphitic coating and the role of metallic Co. It is obvious that the transformation of diamond nanoparticles into graphitic coating is assisted by the Co nanoparticles. Catalytic effects by the metals in graphitization have been investigated

for some decades [8, 9, 11]. Sinclair and co-workers [12, 13, 14] showed that amorphous carbon in contact with Co fully crystallizes between 500 and 600 °C. This graphitization temperature is close to the present result; the present Raman and DSC studies indicates that diamond nanoparticles are graphitized at about 600 °C. They suggested a model of metal-mediated graphitization, in which carbon is dissolved into the metal, and upon supersaturation, graphite precipitates outwardly at the interface, just similar to the dissolution-precipitation mechanism. However, as depicted in a binary alloy phase diagram [15], the equilibrium solubility of carbon in Co at 600 °C is extremely low (about 0.2 at.%); carbon atoms hardly dissolve into Co. Therefore there has been ambiguity whether or not graphitization at 600 °C is really mediated by the dissolution of the carbon atoms into the interstitial and/or substitutional sites in metallic Co.

For the nanocapsules prepared by modified arc discharge method [16], the thickness of the coating increased by post annealing, suggesting that the addition of graphitic layers results from a precipitation of carbon previously dissolved in the metal. This is thought to be an evidence of dissolution-precipitation mechanism. On the contrary, present TEM studies show that, once the coating is formed, the number of the graphitic layers does not increase on further heating and cooling. The present formation mechanism is thus different from the dissolution-precipitation mechanism. In other words, diamond nanoparticles are not dissolved into Co nanoparticles but directly transformed into the graphitic coating on the surface of Co. It is likely that the surface of metallic Co provides a fast path to release the excess free energy of diamond nanoparticles [17] and a medium for the diffusion of mobile carbon atoms [18], thus facilitating crystalline growth of graphitic layers. As a conclusion, we propose that the present formation mechanism of Co filled carbon nanocapsules is a metal-template graphitization, in which metallic Co simply acts as templates for the coating.

5.4 Conclusion

We have demonstrated a new and simple method for synthesizing Co, Ni, and Fe filled carbon nanocapsules via solid state reaction. The formation mechanism for Co filled carbon nanocapsules has been studied in detail by *in-situ* TEM, XRD and Raman spectroscopy. In the initial mixture, surface-oxidized β-Co nanoparticles about 30 nm in diameter were surrounded by diamond nanoparticles about 5 nm in diameter. Raman studies showed that the reduction of Co_3O_4 to metallic Co at about 600 °C is accompanied by the drastic progress of graphitization of diamond nanoparticles, suggesting that diamond nanoparticles being in contact with the metallic Co are transformed to the graphitic coating layers. *In-situ* TEM experiments showed that the graphitic coating is formed not on cooling but

on heating process. Moreover, once the coating was formed, the number of the graphitic layers was almost constant on further heating and cooling. These results allow us to conclude that metallic Co simply acts as templates for the formation of the graphitic coating and propose a metal-template graphitization mechanism. Metallic particles provide the place to release the excess free energy of diamond nanoparticles and diamond nanoparticles are re-crystallized as graphitic coating layers on the surface of metals.

References

[1] *American Society for Testing and Materials, Powder Diffraction Files*, (Joint Committee on Powder Diffraction Standards, U.S.A.)

[2] S. Gangopadhyay, G. C. Hadjipanayis, B. Dale, C. M. Sorensen, K. J. Klabunde, V. Papaefthymiou, and A. Kostikas, Phys. Rev. B **45**, 9778 (1992).

[3] J. J. Host, M. H. Teng, B. R. Elliott, J.-H. Hwang, T. O. Mason, D. L. Johnson, and V. P. Dravid, J. Mater. Res. **12**, 1268 (1997).

[4] J. W. Ager, D. K. Veirs, and G. M. Rosenblatt, Phys. Rev. B **43**, 6491 (1991).

[5] M. J. Lipp, V. G. Baonza, W. J. Evans, and H. E. Lorenzana, Phys. Rev. B **56**, 5978 (1997).

[6] E. D. Obraztsova, M. Fujii, S. Hayashi, V. L. Kuznetsov, Yu. V. Butenko, and A. L. Chuvilin, Carbon **36**, 821 (1998).

[7] H. Ohtsuka, T. Tabata, O. Okada, L. M. F. Sabatino, and G. Bellessi, Catalysis Letters **44**, 265 (1997).

[8] H. Marsh and A. P. Warburton, J. Appl. Chem. **20**, 133 (1970).

[9] A. Oya and H. Marsh, J. Mater. Sci. **17**, 309 (1982).

[10] Y. Saito, T. Yoshikawa, M. Okuda, N. Fujimoto, S. Yamamoto, K. Wakoh, K. Sumiyama, K. Suzuki, and A. Kasuya, J. Appl. Phys. **75**, 134 (1994).

[11] R. Lamber, N. Jaeger, and G. Schulz-Ekloff, Surface Sci. **197**, 402 (1988).

[12] T. J. Konno and R. Sinclair, Acta Metall. Mater. **42**, 1231 (1994).

[13] T. J. Konno and R. Sinclair, Acta Metall. Mater. **43**, 471 (1995).

[14] A. G. Ramírez, T. Itoh, and R. Sinclair, J. Appl. Phys. **85**, 1508 (1999).

[15] K. Ishida and T. Nishizawa, in *Binary Alloy Phase Diagrams (Second Edition) Vol. 1*, edited by T. B. Massalski *et al.* (Materials Park, Ohio: ASM International, 1990).

[16] J. Jiao and S. Seraphin, J. Appl. Phys. **83**, 2442 (1998).

[17] T. J. Konno and R. Sinclair, Philos. Mag. B **66**, 749 (1992).

[18] F. J. Derbyshire, A. E. B. Presland, and D. L. Trimm, Carbon **13**, 111 (1975).

Chapter 6

Fabrication and Magnetic Properties of Filled Carbon Nanocapsule Thin Films

6.1 Introduction

In order to attempt the application of carbon nanocapsules to magnetic recording media, it is important to develop thin films composed of filled carbon nanocapsules, so-called nanogranular thin films. Recently, we have succeeded in preparing thin films composing of Ni-filled carbon nanocapsules (Ni-C nanogranular thin films) [1]. Ni nanoparticles were about 5.6 nm in average diameter with a narrow size distribution. However, the coercivity of the film was not sufficiently high ($\sim$ 50 Oe). The low coercivity of the film is one of the drawbacks in the application for recording media. In order to improve the magnetic properties, we intend to add Co atoms into Ni nanoparticles. Ni and Co resolve each other over the entire concentration range and form $Ni_{1-x}Co_x$ alloy. The alloy formation is expected to increase the coercivity for the nanogranular thin films [2]. In addition to the applied physical context, the formation mechanism and magnetic properties of such nanogranular thin films are also of great interests from the viewpoints of fundamental physics of magnetic nanoparticle systems.

In this chapter, we demonstrate a successful fabrication of $Ni_{1-x}Co_x$ filled carbon nanocapsule thin films ($Ni_{1-x}Co_x$-C nanogranular thin films) by a co-sputtering method together with post-annealing. We find an improvement in the magnetic properties of the films by optimizing the Co/(Ni+Co) alloy ratio (x); the coercivity of the film exhibits a maximum at x=0.83. A possible mechanism for the appearance of the maximum in the coercivity is discussed. The discussion is mainly based on the correlation between the size distribution of the nanoparticles and their coercivities. Present results suggest that

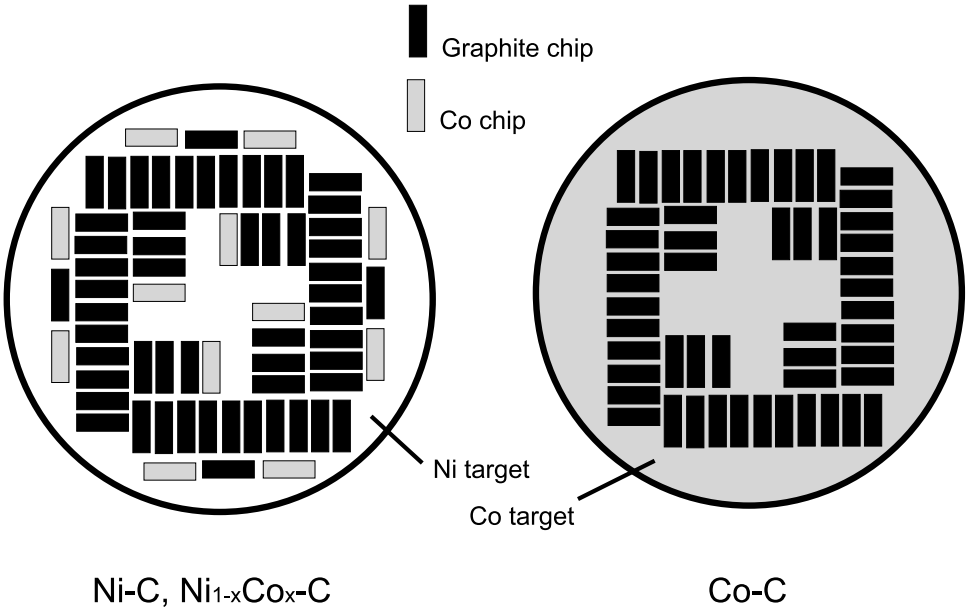

Figure 6.1: Configurations of the chips on the sputtering targets.

the controllability of the size distribution as well as the average diameter is especially important for realizing the nanogranular thin films with a high coercivity.

6.2 Experimental Procedure

Thin films of a mixture of Ni, Co and C were prepared by a co-sputtering method developed in our previous work [1]. As shown in Fig. 6.1, graphite and Co chips were placed on a Ni target for the Ni-C and $Ni_{1-x}Co_x$-C samples, and graphite chips are placed on a Co target for the Co-C sample. They were simultaneously sputtered in Ar gas of 2.7 Pa using an rf magnetron sputtering apparatus. In this technique, the concentration of Ni, Co, and C in the films can be changed by the areal ratio of Ni, Co, and graphite. The concentration of carbon atoms in the film was estimated by electron probe microanalyses (EPMA) and fixed at about 30 at.% for all the samples. The films were deposited onto Si substrates. The substrates were not intentionally heated during the deposition. The sputtering conditions were summarized in Table 6.1. As-deposited films were subsequently annealed at different temperatures from 300 to 700°C for 1 hour in vacuum ($< 10^{-5}$ Pa) using a conventional electrical furnace.

The structure of the films was studied by transmission electron microscopy (TEM) and selected-area electron diffraction (SAED). For TEM studies, thin films about 20 nm in thickness were scrubbed from the substrates, dispersed into ethanol, and put onto the

Table 6.1: Summary of the sputtering conditions.

Target	Co chips	Graphite chips	Rate [nm/min]	C [at.%]	x
Ni	0	56 (5×15 mm^2)	5.5	35	0
	4 (5×10 mm^2)				0.19
	4 (5×15 mm^2)				0.63
	12 (5×15 mm^2)				0.83
Co	-	52 (5×15 mm^2)	6.2	32	1

carbon-coated grids. The JEOL JEM-2010 transmission electron microscope operated at 200 kV was used. The Co/(Ni+Co) alloy ratio (x) was estimated using an energy dispersive x-ray spectrometer (EDS) attached to TEM. Raman spectroscopy was performed at room temperature using a SPEX 1877 Triplemate equipped with a charge coupled device. To remove the signal by light scattered by air, the samples were put into a cell with windows purged by Ar gas. The excitation source was the 514.5 nm line of an Ar-ion laser. The spectra were acquired with a 90° scattering geometry. The in-plane magnetic properties were studied at room temperature using a vibrating sample magnetometer (VSM) [TM-VSM 2030HG (Tamagawa)] with an applied magnetic field up to 10 kOe. For Raman and VSM studies, samples about 100 nm in thickness were used.

6.3 Results and Discussion

6.3.1 Formation of $Ni_{1-x}Co_x$-C nanogranular thin films

Figure 6.2(a) shows a typical high-resolution TEM image of $Ni_{0.17}Co_{0.83}$-C nanogranular thin films, which are formed by annealing at 425°C. Nanoparticles separated by matrices are seen. The average diameter (d_{ave}) and the standard deviation (σ) of the nanoparticles obtained from several TEM images are 7.8 and 1.6 nm, respectively. In the matrix region, lattice fringes corresponding to (002) planes of graphite are seen. Figure 6.2(b) shows the corresponding SAED pattern together with diffraction patterns calculated from the American Society for Testing and Materials data [3] for graphite and hcp-Co. Almost all diffraction patterns observed can be assigned to the hcp phase of Co. The change in lattice spacing of hcp-Co induced by alloying with Ni is too small to be distinguished by SAED. Although not shown here, SAED studies for all the samples elucidated that $Ni_{1-x}Co_x$ alloy nanoparticles have only fcc structure up to x=0.63. Above x=0.83, the hcp phase appears. This behavior is very similar to bulk $Ni_{1-x}Co_x$ crystal which is transformed from fcc into hcp above x=0.7 [4]. The structures of alloy nanoparticles at various x are listed

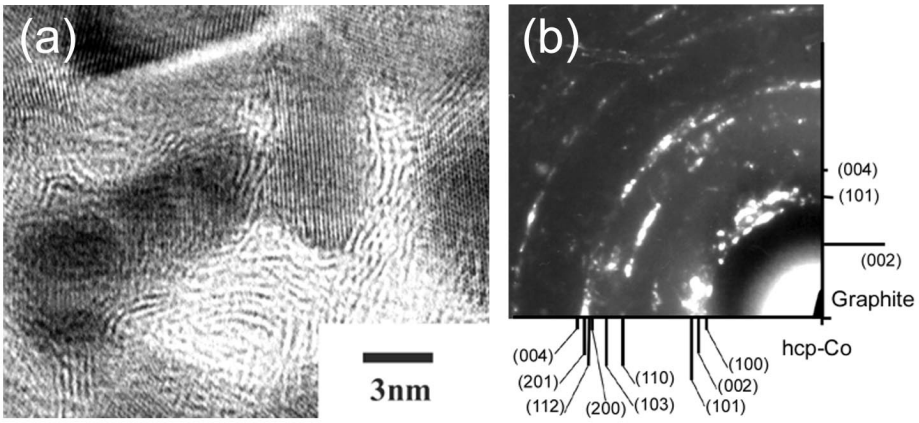

Figure 6.2: (a) A high-resolution TEM image and (b) a corresponding SAED pattern of $Ni_{0.17}Co_{0.83}$-C nanogranular thin film formed by annealing at 425°C. We can see that hcp-$Ni_{0.17}Co_{0.83}$ alloy nanoparticles are separated by graphitic matrices.

in Table 6.2.

The formation of graphitic matrices in the films was also confirmed by Raman spectroscopy. Figure 6.3 shows Raman spectra of the films with x=0.83 at various annealing temperatures. The spectrum for the as-deposited film exhibits a broad Raman band at around 1565 cm^{-1}. The band can be assigned to the E_{2g} mode in the graphitic structure (G band) [5]. In addition, a weak band is seen at about 1350 cm^{-1} being barely resolved from the G band. This band corresponds to the so-called D band, which is considered to be induced by disorders in the graphitic structure [6, 7]. The Raman features are similar to that of amorphous carbon [8, 9], indicating that the film is composed of very small fragments of carbon sp^2 sheets.

With increasing annealing temperature, both D and G bands become narrower and

Table 6.2: Summary of results for $Ni_{1-x}Co_x$ filled carbon nanocapsule thin films. T_a denotes the temperature where the nanogranular morphology is observed by TEM.

x	T_a (°C)	Structure	d_{ave} (nm)	σ (nm)	M_s (emu/g)	H_c (Oe)
0	400	fcc	5.6	0.92	37	48
0.19	400	fcc	6.7	1.0	58	330
0.63	400	fcc	6.7	0.93	125	736
0.83	425	hcp	7.8	1.6	139	907
1	600	hcp	9.5	4.4	145	407

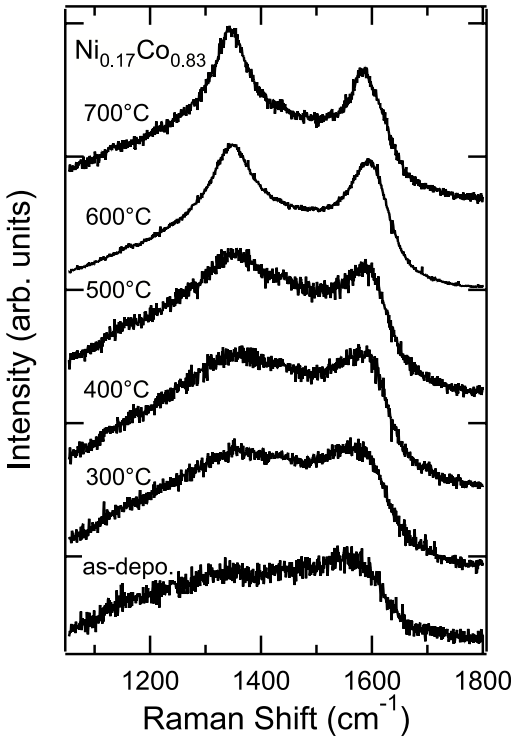

Figure 6.3: Raman spectra of the thin film with x=0.83 at various annealing temperatures.

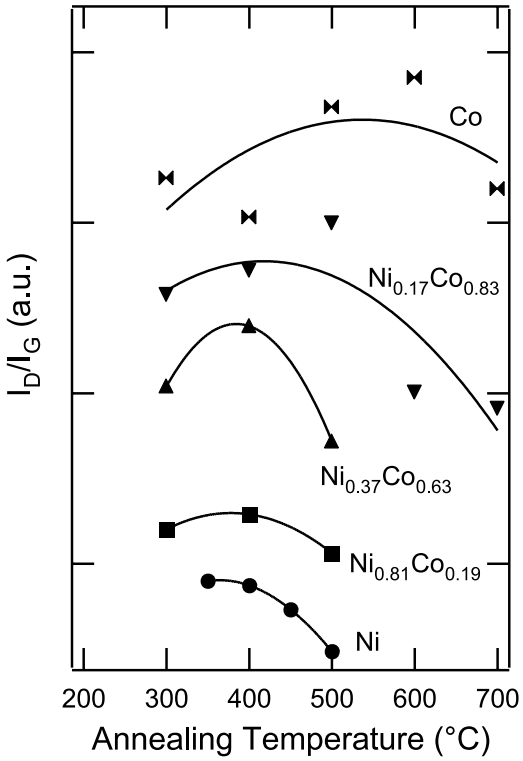

Figure 6.4: Integrated intensity ratio of the D to G bands as a function of annealing temperature for the films with different x. The solid curves are drawn to guide the eyes.

the G band shifts to higher frequency up to 1580 cm^{-1}. The well-defined D and G bands can be seen at temperatures higher than 300°C. Moreover, the intensity of the D band increases with the annealing temperature. In Fig. 6.4, the relative integrated intensities of the D to G bands (I_D/I_G) are plotted as a function of annealing temperature at various x. The solid curves are drawn to guide the eyes. For $Ni_{0.17}Co_{0.83}$, as the annealing temperature increases, I_D/I_G first increases and then decreases. Ferrari and Robertson [10] suggested that, in amorphous carbons, the development of a D band indicates the ordering of sp^2 sheets and increasing in the in-plane size (L_a) up to about 2 nm as shown in Fig. 6.5. On the other hand, the so-called Tuinstra-Koenig relationship [5] showed that I_D/I_G decreases with decreasing number of disorders in the nanocrystalline graphite having L_a above 2 nm [10]. It is thus plausible that I_D/I_G in Fig. 6.4 should show the maximum value at the temperature where the graphitic matrices are formed. In other words, the formation temperature of the carbon nanocapsule thin film with graphitic matrices can be estimated from the maximum point of I_D/I_G in Fig. 6.4 [11]. For example, $Ni_{0.17}Co_{0.83}$ filled carbon nanocapsule thin film is formed at about 450°C, being close to the temperature at which the nanogranular morphology with graphitic matrices

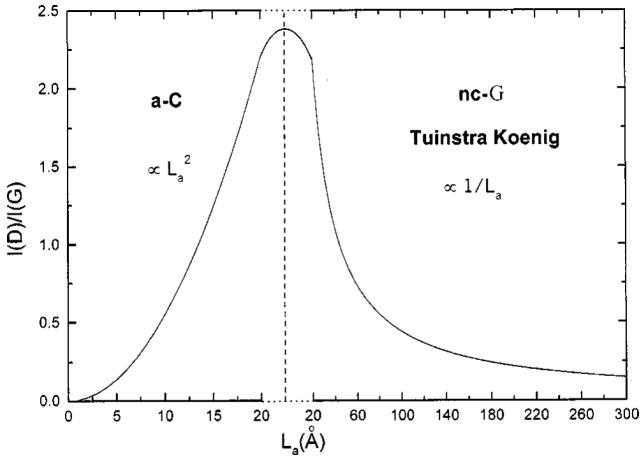

Figure 6.5: I_D/I_G as a function of the in-plane size of sp^2 sheet (L_a) [10].

was observed by TEM (425°C).

Figure 6.4 also shows that the formation temperature of the $Ni_{1-x}Co_x$-C nanogranular thin films increases with x. The fact that the formation temperature depends on x is deeply related to the formation mechanism of the carbon nanocapsule thin films with graphitic matrices. The formation mechanism has already been investigated in our previous work [1]. The as-deposited film is a mixture of metallic atoms and very small fragments of carbon sp^2 sheets. By post-annealing, the film is first transformed into a film consisting of metallic-carbide nanoparticles. Since the carbide nanoparticles are unstable at higher temperature [12], they are decomposed into metal and carbon. During the decomposition, the carbon atoms segregate out of the nanoparticles. The segregated carbon atoms are likely to form a graphitic structure. The decomposition is thus accompanied by the formation of the nanogranular thin films with graphitic matrices. This mechanism points out that the difference in the decomposition temperature of metallic-carbide nanoparticles gives rise to the difference in the formation temperature of the nanogranular thin films. It has been reported that the decomposition temperature of carbide is different between Ni and Co; Ni_3C separates into Ni and C at about 400°C [12], while Co_3C separates into Co and C above 500°C [13]. As a result, the formation temperature of the nanogranular thin film (T_a) increases with x in good agreement with the results of TEM studies for all the samples with different x as shown in Table 6.2.

A higher formation temperature of the nanogranular thin films brings about a longer diffusion length of metal grains [14], leading to the formation of larger particles at larger x. The size distributions evaluated from TEM micrographs are shown in Fig. 6.6. Both d_{ave} and σ increase with x. In the range of x from 0 to 0.83, the mean particle diameter

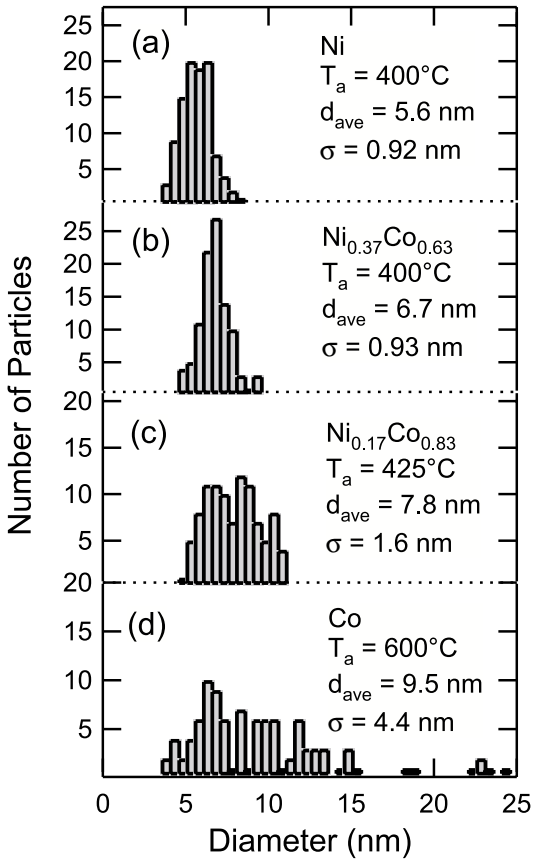

Figure 6.6: Size distribution of the nanoparticles estimated from TEM images. (a) Ni-C, (b) $Ni_{0.37}Co_{0.63}$-C, (c) $Ni_{0.17}Co_{0.83}$-C, and (d) Co-C nanogranular thin films.

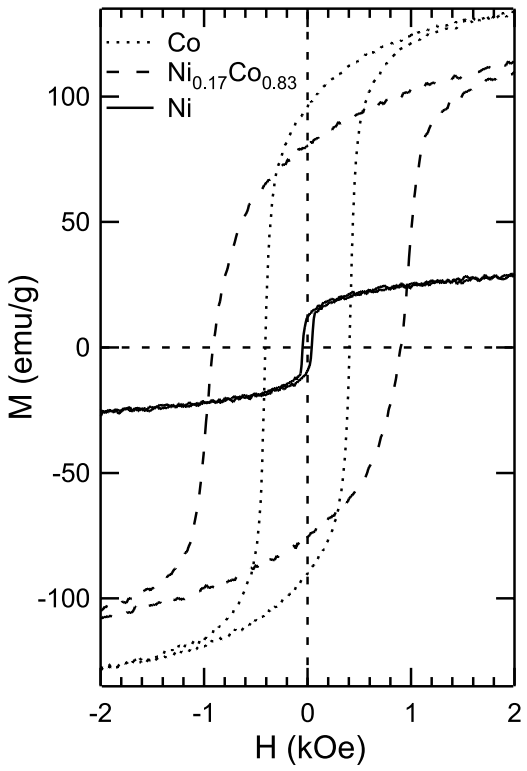

Figure 6.7: In-plane magnetic hysteresis loops of the $Ni_{1-x}Co_x$-C nanogranular thin films with x=0, 0.83, 1.

is less than 8 nm and the width of the size distribution is small ($\sim$ 20 % of d_{ave}). On the contrary, the Co-C nanogranular thin film (x=1) contains extremely large particles above 10 nm in diameter. The estimated d_{ave} and σ are summarized in Table 6.2.

6.3.2 Magnetic properties of nanogranular thin films

Figure 6.7 shows the in-plane magnetic hysteresis loops of the nanogranular thin films with x=0, 0.83 and 1. The magnetization in Fig. 6.7 is divided by the mass of the metal estimated by EPMA and EDS. We see that both the saturation magnetization (M_s) and coercivity (H_c) determined from the hysteresis loops strongly depend on x. The M_s and H_c for all the samples are given in Table 6.2, and plotted as a function of x in Figs. 6.8(a) and 6.8(b), respectively. The solid curves in Fig. 6.8 are drawn to guide the eyes. Figure 6.8(a) shows that M_s increases monotonically with x. In contrast, H_c in Fig. 6.8(b) initially increases with x, exhibits a maximum value of 907 Oe at x=0.83, and then decreases at x=1. The maximum H_c (907 Oe) in the present study is superior to that in Co-C nanogaranular films (370 Oe) in Ref. [15], and inferior to those in CoPt-C

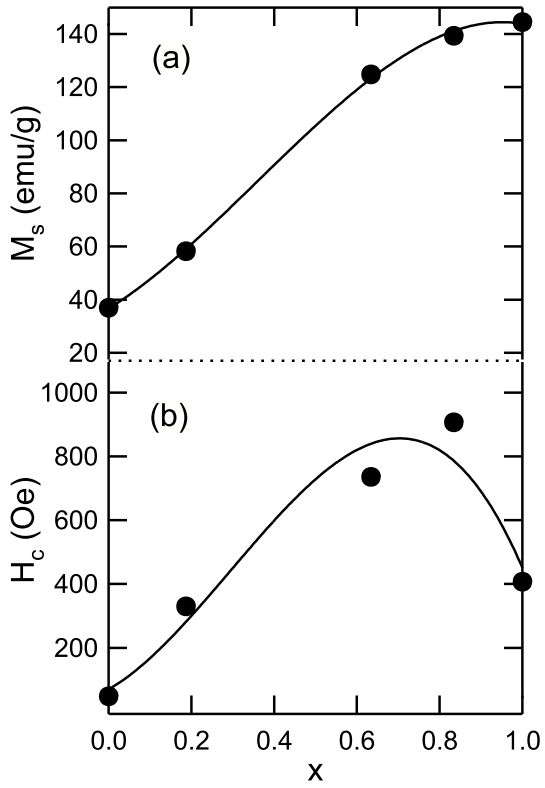

Figure 6.8: (a) M_s and (b) H_c for the $Ni_{1-x}Co_x$-C nanogranular thin films plotted as a function of x. The solid curves are drawn to guide the eyes. Note here that, as x increases, H_c first increases up to 907 Oe and then decreases.

nanogranular films (1500 Oe) in Ref. [16] and CoCrPt-C nanogranular films (10 kOe) in Ref [17].

In a bulk $Ni_{1-x}Co_x$ alloy crystal, both M_s and H_c continuously increase with x [2]. The increase in H_c of $Ni_{1-x}Co_x$-C nanogranular thin films at x ranging from 0 to 0.83 is believed to be due to alloying. At x=0.83, the further enhancement in the H_c may be interpreted by the transformation from the fcc to hcp phase because the magnetocrystalline anisotropy of hcp-$Ni_{1-x}Co_x$ alloy nanoparticles should be larger than that of fcc-$Ni_{1-x}Co_x$ [18]. The drop in the H_c at x=1, however, cannot be explained in the framework of the phase transition. Therefore, the magnetic properties in this system are not governed by the crystalline anisotropy. We should recall here that present TEM studies revealed that the width of the size distribution of the nanoparticles is large at x=1 [Fig. 6.6(d)]. The Co-C nanogranular thin film contains extremely large particles above 10 nm in diameter. The existence of the large particles is believed to cause the drop in H_c at x=1.

It is well known that for fine particles the coercivity depends striking on the size [19].

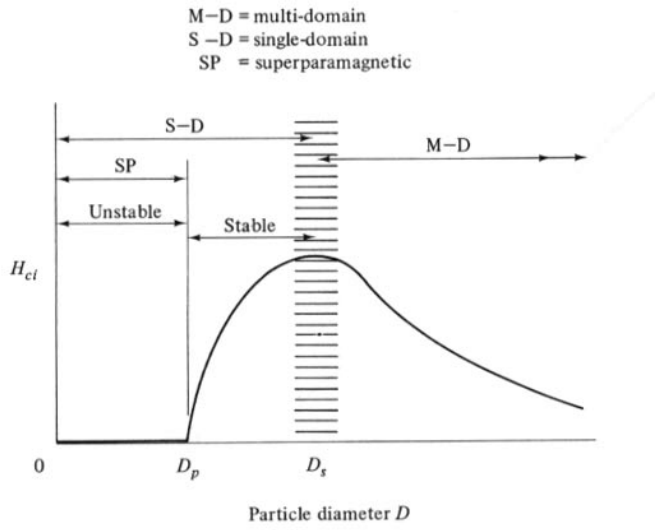

Figure 6.9: Variation of intrinsic coercivity H_{ci} with particle diameter D (schematic) [19]. The critical diameters for single-domain and superparamagnetic are denoted by D_s and D_p, respectively.

Here we consider an isolated spherical magnetic fine particle having a diameter of d. The particle with large d becomes multi-domain; the magnetization of the particle changes by domain wall motion. The size dependence of the coercivity H_c for the particle in this size range is experimentally found to be given approximately by

$$H_c = a + \frac{b}{d}, \tag{6.1}$$

where a and b are constants. In this range, H_c increases with decreasing d as shown schematically in Fig. 6.9.

The decrease in d is accompanied by a decrease in the width of the magnetic domain (w) as described in the following [4]. The domain wall energy U_w in the particle is roughly estimated as

$$U_w = \gamma \times \pi r^2 \times \frac{2r}{w}, \tag{6.2}$$

where γ is the surface energy of domain wall, r is the radius of thy particles ($= d/2$). On the other hands, the magnetostatic energy U_m of the particle follows

$$U_m = \frac{I_s^2}{6\mu_0} \times \frac{4}{3}\pi r^3 \times \frac{w}{2r}, \tag{6.3}$$

where I_s is the spontaneous magnetization, and μ_0 is the permeability of vacuum. The total energy U is thus provided by

$$U = U_w + U_m = \frac{2\pi\gamma r^3}{w} + \frac{\pi I_s^2 r^2}{9\mu_0} w. \tag{6.4}$$

The minimum of the U is given from the first derivative of Eq. (6.4) as follows

$$\frac{\partial U}{\partial w} = -\frac{2\pi\gamma r^3}{w^2} + \frac{\pi I_s^2 r^2}{9\mu_0} = 0. \tag{6.5}$$

We thus obtain the following expression for a domain wall width w

$$w = \sqrt{\frac{18\gamma\mu_0 r}{I_s^2}} = \sqrt{\frac{9\gamma\mu_0 d}{I_s^2}} \propto \sqrt{d}. \tag{6.6}$$

Equation (6.6) indicates that the domain wall width w decreases more slowly than the particle diameter d. As a results, below a critical diameter d_s, the domain wall width w is equal to d; the particle becomes singe-domain. The d_s is thus derived from Eq. (6.6) in the condition of $w = d_s$ as follows

$$d_s = \frac{9\gamma\mu_0}{I_s^2}. \tag{6.7}$$

As the particle size decreases below d_s, the coercivity H_c decreases, because of thermal effects, according to

$$H_c = g - \frac{h}{d^{3/2}}, \tag{6.8}$$

where g and h are constants. Consequently, the coercivity exhibits a maximum at d_s as shown in Fig. 6.9. As the d decreases further, the coercivity is zero below a critical diameter d_p, again because of thermal effects, which are now strong enough to spontaneously demagnetize a previously saturated assembly of particles. Such particles are called "superparamagnetic". The description in the above are based on the "ideal" isolated spherical magnetic particles. For the particles with magnetostatic interaction, the decrease in the magnetostatic energy U_m brings about a increase in the value of critical size d_s. For hcp-Co, the calculated d_s is above 40 nm [20].

As mentioned in the above, the transformation from the single-domain to multi-domain state gives the maximum in the coercivity at a critical diameter d_s. This is one of the possible explanations for the drop in H_c at x=1. However, taking into account the calculated d_s of hcp-Co nanoparticles ($>$ 40 nm), almost all the particles in the Co-C nanogranular thin film are thought to be in the single-domain state. The decrease in the H_c due to the transformation into multi-domain particles is thus unlikely.

An alternative possible explanation is the surface effects which appreciably influence the magnetic properties of nanoparticles. Chen *et al.* [21] reported that the surface anisotropy dominates in the coercivity of iron-group metal alloy nanoparticles with fcc structure. They showed that, considering an assembly of spherical, random and noninteracting single-domain particles (diameter d) with surface anisotropy constant K_s, the coercivity is given by

$$H_c = \frac{5.76K_s}{M_s d}\left[1 - \left(\frac{25kT}{K_s\pi d^2}\right)^{1.155}\right], \tag{6.9}$$

where k and T are the Boltzmann constant and the temperature, respectively. When d is larger than $d_p = (25kT/\pi K_s)^{1/2}$ (the upper particle diameter limit of superparamagnetic behavior), the last term in Eq. (6.9) can be neglected and the coercivity is thus proportional to the inverse of d, i.e., $H_c \propto 1/d$. For the sample with x=1, d_{ave} is 9.5 nm, which is larger than the d_p reported for hcp-Co (about 7 nm) [20]. Therefore, the decrease in H_c at x=1 can be explained by the formation of the large particles, for which the surface anisotropy is a dominant factor determining the magnetic coercivity.

6.4 Conclusion

$Ni_{1-x}Co_x$ filled carbon nanocapsule thin films ($Ni_{1-x}Co_x$-C nanogranular thin films) have been successfully prepared by a co-sputtering method together with post-annealing. TEM observation showed nanoparticles with a small mean diameter and narrow size distribution in the film. From TEM and Raman studies, it was found that the formation temperature of the carbon nanocapsule thin films increases with x, mainly owing to the increase in the decomposition temperature of the carbide. The higher formation temperature causes the larger mean diameter and wider size distribution of the nanoparticles. Particularly at x=1 (Co-C nanogranular thin film), an existence of extremely large particles above 10 nm in diameter can be observed.

The magnetic properties of the nanogranular thin films were also studied. With increasing x, the coercivity of the carbon nanocapsule thin film increases, exhibits a maximum value of 907 Oe at x=0.83 and then decreases at x=1. The increase with x can be explained within the framework of the alloy formation. On the other hand, taking into consideration the surface anisotropy effect, the existence of extremely large Co particles is thought to result in a decrease in the coercivity of Co-C nanogranular thin films. Present results allow us to conclude that the magnetic properties of the magnetic alloy nanogranular thin films can be improved by optimizing the alloy ratio. Moreover, the controllability of the size distribution as well as the particle diameter is important for realizing the tailored nanogranular thin films with a high coercivity.

References

[1] O. Mamezaki, H. Adachi, S. Tomita, M. Fujii, and S. Hayashi, Jpn. J. Appl. Phys. **39**, 6680 (2000).

[2] R. M. Bozorth, *Ferromagnetism* (Van Nostrand, New York, 1951).

[3] *American Society for Testing and Materials, Powder Diffraction Files* (Joint Committee on Powder Diffraction Standards, U.S.A.).

[4] S. Chikazumi, *Physics of Ferromagnetism* (Syokabo, Tokyo, 1978) [in Japanese].

[5] F. Tuinsra and J. L. Koenig, J. Chem. Phys. **53**, 1126 (1970).

[6] R. J. Nemanich and S. A. Solin, Phys. Rev. B **20**, 392 (1979).

[7] M. J. Matthews, M. A. Pimenta, G. Dresselhause, M. S. Dresselhause, and M. Endo, Phys. Rev. B **59**, R6585 (1999).

[8] Q. Wang, D. D. Allred, and J. González-Hernández, Phys. Rev. B **47**, 6119 (1993).

[9] J. Z. Wan, F. H. Pollak, and B. F. Dorfman, J. Appl. Phys. **81**, 6407 (1997).

[10] A. C. Ferrari and J. Robertson, Phys. Rev. B **61**, 14095 (2000).

[11] H. Wang, S. P. Wong, W. Y. Cheung, N. Ke, M. F. Chiah, H. Liu, and X. X. Zhang, J. Appl. Phys. **88**, 2063 (2000).

[12] S. Nagakura, J. Phys. Soc. Jpn. **12**, 482 (1957).

[13] S. Nagakura, J. Phys. Soc. Jpn. **16**, 1213 (1961).

[14] J. J. Host, J. A. Block, K. Parvin, V. P. Dravid, J. L. Alpers, T. Sezen, and R. Raduca, J. Appl. Phys. **83**, 793 (1998).

[15] T. Hayashi, S. Hirono, M. Tomita, and S. Umemura, Nature **381**, 772 (1996).

[16] J. -J. Delaunay, T. Hayashi, M. Tomita, S. Hirono, and S. Umehara, Appl. Phys. Lett. **71**, 3427 (1997).

[17] H. Zeng, M. L. Yan, Y. Liu, and D. J. Sellmyer, J. Appl. Phys. **89**, 810 (2001).

[18] H. Sato, O. Kitakami, T. Sakurai, Y. Shimada, Y. Otani, and K. Fukamichi, J. Appl. Phys. **81**, 1858 (1997).

[19] B. D. Cullity, *Introduction to Magnetic Materials* (Addison-Wesley, Reading, MA, 1972).

[20] O. Kitakami, T. Sakurai, Y. Miyashita, Y. Takeno, Y. Shimada, H. Takano, H. Awano, K. Ando, and Y. Sugita, Jpn. J. Appl. Phys. **36**, 1724 (1996).

[21] C. Chen, O. Kitakami, S. Okamoto, and Y. Shimada, J. Appl. Phys. **86**, 2161 (1999).

Chapter 7

Concluding Remarks of This Thesis

In this thesis, the author has studied the formation and physical properties of novel carbonaceous nano-materials. The present study has given deeper insights into the structural, electronic and optical properties of carbon onions, and into the formation mechanism and magnetic properties of carbon nanocapsule systems. The followings are the concluding remarks of the present study.

In Chapter 2, the structure and electronic states of carbon onions prepare form diamond nanoparticles were investigated. High-resolution transmission electron microscopic (HRTEM) observation demonstrated that diamond nanoparticles are transformed into spherical carbon onions by the annealing at 1700 °C, and finally into polyhedral onions with facets above 1900 °C. The transformation is brought about by the progress of graphitization with increasing the annealing temperatures. HRTEM and Raman studies suggested that spherical onions are composed of graphitic sp^2 network. Electron energy-loss spectrum in plasmon-loss region indeed indicated the presence of π electrons, which are induced by the sp^2 network. On the other hands, core-loss spectrum in carbon K-edge region revealed that spherical onions contain a number of sp^3 bonds. In addition, electron spin resonance (ESR) studies for the spherical onions indicated the presence of dangling bonds associated with structural defects and the absence of conduction electron spins due to π electrons. These results allow us to suggest a precise structural model of spherical onions; the spherical onion consists of small domains of graphitic sp^2 sheets with dangling bond defects in the peripheries, which are induced by sp^3 bridge-like bondings between the adjacent sheets. π electrons in spherical onions are thus localized in the small domains and do not act as conduction electrons. On the other hand, for polyhedral onions, ESR spectra showed the generation of conduction electrons, suggesting that further graphitization decreases the number of dangling bonds in the onions and leads to the delocalization of π electrons. The experimental results in this chapter strongly suggest that the structure of spherical carbon onions is far from perfectly closed graphitic shells and the sphericity

is attributed to imperfect sp^2 graphitic shells with a number of defects such as sp^3-like dangling bonds (a defective spherical onion model). The hybrid sp^2-sp^3 structures of spherical onions realize their intriguing electronic properties.

In Chapter 3, we focused on the structure of the onions and monitored the transformation of diamond nanoparticles by heat treatment up to 2000 °C using synchrotron x-ray diffraction (XRD). Precise measurements have been made on initial diamond nanoparticles and three heat-treated samples (1400 °C, 1700 °C, and 2000 °C) using a high intensity beam from a synchrotron radiation source. The results demonstrate a sequence of changes which correlate well with TEM studies on same samples and involve a transformation from a sp^3 to sp^2-type bonding configuration. At 1400 °C, there is an initial development of a graphitic outer coat on the diamond nanoparticles which then becomes transformed into a carbon onion with a spherical shell surrounding a diamond core at 1700 °C. At higher temperatures of 2000 °C, the diamond core disappeared and the outer layers develop a facetted graphitic structure. The estimated interlayer distance for the onions is larger than the bulk graphite value. These results are in good agreement with other studies based on Raman, ESR, and electron energy-loss measurements, suggesting the defective spherical onion model. Due to the broad nature of the peaks and limited k-range in the preset experiment, the detailed atomic arrangement of the carbon onions cannot be deduced unfortunately from the present measurements but further work using pulsed neutron measurements could throw some light on this issue.

In Chapter 4, optical extinction properties of the carbon onions were studied. Experimental extinction spectra of the spherical and polyhedral onions prepared from diamond nanoparticles were acquired by UV-Vis. optical transmission spectroscopy. In order to interpret the experimental results, we also carried out theoretical considerations for the extinction properties of the onions. Experimental spectra for spherical onions shows an extinction peak around at 3.9 μm^{-1}. By considering the aggregate of the defective spherical onions, theoretical calculations can explain well the experimental results. For polyhedral onions, experimental spectrum exhibits two peaks at 3.9 and 4.6 μm^{-1}. The spectrum with double peaks can be reproduced successfully by assuming the aggregate of polyhedral onions as that of anisotropic graphite ellipsoids. Furthermore, we address the contribution of the onions to the interstellar extinction bump at 4.6 μm^{-1}. The theoretical simulation by our defective spherical onion model permits us to suggest that the defective spherical onion, which are prepared in the present studies, is a strong candidate for the carbonaceous interstellar dust giving rise to the absorption bump at 4.6 μm^{-1}. The result implies that the interstellar dust particles might be duplicated by the defective onions in laboratory, thus opening the way to address experimentally to another open questions in the astronomy and astrophysics, such as unidentified infrared emission bands.

In Chapter 5, we developed a new preparation method of magnetic-metal filled carbon nanocapsules via solid state reaction, and studied their formation mechanism by *in-situ* TEM, XRD and Raman spectroscopy. The method was just to anneal the mixture of magnetic-metal (Co, Ni, and Fe) and diamond nanoparticles. For Co samples, surface-oxidized β-Co nanoparticles about 30 nm in diameter were surrounded by diamond nanoparticles about 5 nm in diameter in the initial mixture of Co and diamond nanoparticles. Raman studies showed that the reduction of Co_3O_4 to metallic Co at about 600 °C is accompanied by the drastic progress of graphitization of diamond nanoparticles, suggesting that diamond nanoparticles being in contact with the metallic Co are transformed to the graphitic coating layers. *In-situ* TEM experiments showed that the graphitic coating is formed not on cooling but on heating process. Moreover, once the coating was formed, the number of the graphitic layers was almost constant on further heating and cooling. These results allow us to conclude that metallic Co simply acts as templates for the formation of the graphitic coating (a metal-template graphitization mechanism) instead of dissolution-precipitation mechanism that is proposed in the vapor phase formation. The template mechanism make it possible to form size-controlled filled nanocapsules with very thin graphitic coating as shown in the present study.

In Chapter 6, $Ni_{1-x}Co_x$ filled carbon nanocapsule thin films ($Ni_{1-x}Co_x$-C nanogranular thin films) were successfully fabricated by a co-sputtering method together with post-annealing. TEM observation showed nanoparticles with a small mean diameter and narrow size distribution in the film. From TEM and Raman studies, it was found that the formation temperature of the carbon nanocapsule thin films increases with alloy ratio x, mainly owing to the increase in the decomposition temperature of the carbide. The higher formation temperature causes the larger mean diameter and wider size distribution of the nanoparticles. Particularly at x=1 (Co-C nanogranular thin film), the existence of extremely large particles above 10 nm in diameter were observed. The magnetic properties of the nanogranular thin films were also studied. With increasing x, the coercivity of the carbon nanocapsule thin film increased, exhibited a maximum value of 907 Oe at x=0.83 and then decreased at x=1. The increase with x can be explained within the framework of the alloy formation. On the other hand, taking into consideration the surface anisotropy effect, the existence of extremely large Co particles is thought to result in a decrease in the coercivity of Co filled carbon nanocapsule thin films. Present results clearly showed that the magnetic properties of the magnetic alloy filled nanocapsule thin films can be improved by optimizing the alloy ratio. Moreover, the controllability of the size distribution as well as the particle diameter is important for realizing the tailored carbon nanocapsule thin films with a high coercivity.

Acknowledgment

The author would like to express his sincere gratitude to Professor Shinji Hayashi for his stimulating discussions and continuous encouragement throughout the course of this study, and for the critical reading of this thesis.

The author would like to express his profound gratitude to Professor Nobuo Ohmae and Professor Tadashi Mukai for their fruitful discussions and valuable comments on this thesis.

The author want to make his deep acknowledgment to Dr. Minoru Fujii for his continuous supports throughout this work, and for valuable discussions leading to the experimental and theoretical ideas implemented in this thesis. The author also wish to make his acknowledgment to Associate Professor Kazuyuki Moriwaki for his valuable discussions and helpful comments in this work. The author wish to extend special acknowledgment to Professor Keiichi Yamamoto to his valuable comments in the initial stage of this work.

The author would like to express his heartfelt gratitude to Professor Hitoshi Ohta and Mr. Takahiro Sakurai for their helpful teaching and discussion on the ESR study of carbon onions. The author also would like to express his greatest thanks to Professor John C. Dore (University of Kent, U.K.) and Dr. Andrej Burian (University of Silesia, Poland) for their useful teaching and discussions on the synchrotron XRD measurements of carbon onions. The author also wish to make his acknowledgment to Professor Hidehiro Yasuda and Dr. Kensuke Akamatsu for their kind teaching and helpful discussion on the structural analyses of carbon nanocapsules using *in-situ* TEM and XRD. Acknowledgment is also due to Mr. Hidenori Ogawa (College of Industrial Technology) for his permission to use the VSM apparatus.

This work has been done at Mesoscopic Material Laboratory, Department of Electrical and Electronics Engineering, Faculty of Engineering, Kobe University, under the direction of Professor Shinji Hayashi. The author wish to give his highest appreciation to his co-workers in the laboratory who have contributed to this work, particularly, to Mr. Masahiro Hikita for his valuable discussion and technical assistance on the study of carbon nanocapsules, to Mr. Hiroaki Adachi for his useful discussion and skillful techni-

cal assistance on the study of carbon nanocapsule thin films, and also to Mr. Yasunori Tsukuda for his skillful technical assistance on the study of extinction spectra of carbon onions.

The author gratefully thanks all colleagues in the Mesoscopic Material Laboratory. In particular, usual and enjoyable discussions with Dr. Yoshihiko Kanzawa, Dr. Yoku Inoue, Dr. Shinji Takeoka, Dr. Osamu Mamezaki, Mr. Atsushi Minura, Mr. Kimiaki Toshikiyo, Mr. Kei Watanabe, and Mr. Hiroshi Tabata are much appreciated.

The author is profoundly indebted to Ms. Keiko Nakamura for her stimulative discussions and endless encouragement throughout this work.

Finally, the author is deeply indebted to his father, Takashi, to his mother, Kazuko, to his brothers, Naohito and Daisuke, to his cats, Hamaoka and Shintaro, and to all his friends for all their hearty support and endless encouragement till now, without which the author could not be able to achieve this work.

List of Publications

(* Papers Relevant to This Study)

1. **Journal Papers**

(1)* Satoshi Tomita, Minoru Fujii, Shinji Hayashi, Keiichi Yamamoto:
"Electron energy-loss spectroscopy of carbon onions"
Chemical Physics Letters, Vol. 305, pp. 225-229, May 1999.
(Chapter 2)

(2)* Satoshi Tomita, Masahiro Hikita, Minoru Fujii, Shinji Hayashi, Keiichi Yamamoto:
"A new and simple method for thin graphitic coating of magnetic-metal nanoparticles"
Chemical Physics Letters, Vol. 316, pp. 361-364, January 2000.
(Chapter 5)

(3)* Satoshi Tomita, Masahiro Hikita, Minoru Fujii, Shinji Hayashi, Kensuke Akamatsu, Shigehito Deki, Hidehiro Yasuda:
"Formation of Co filled carbon nanocapsules by metal-template graphitization of diamond nanoparticles"
Journal of Applied Physics, Vol. 88, No. 9, pp. 5452-5456, November 2000.
(Chapter 5)

(4)* Satoshi Tomita, Takahiro Sakurai, Hitoshi Ohta, Minoru Fujii, Shinji Hayashi:
"Structure and electronic properties of carbon onions"
The Journal of Chemical Physics, Vol. 114, No. 9, pp. 7477-7482, May 2001.
(Chapter 2)

(5)* Satoshi Tomita, Hiroaki Adachi, Minoru Fujii, Shinji Hayashi:
"$Ni_{1-x}Co_x$-C nanogranular thin films prepared by a co-sputtering method: Improvement in magnetic properties by optimizing the alloy ratio"

Japanese Journal of Applied Physics, Vol. 40, No. 11, pp. 6370-6374, November 2001.
(Chapter 6)

(6)* Satoshi Tomita, John C. Dore, Andrzej Burian, Minoru Fujii, Shinji Hayash:
"Diamond nanoparticles to carbon onions transformation: X-ray diffraction studies"
Carbon, accepted.
(Chapter 3)

(7)* Satoshi Tomita, Yasunori Tsukuda, Minoru Fujii, Shinji Hayash:
"Defective carbon onions in the interstellar space as the carrier of the optical extinction bump at 217.5 nm"
Submitted.
(Chapter 4)

(8)* Satoshi Tomita, Minoru Fujii, Shinji Hayashi:
"Optical extinction properties of carbon onions prepared from diamond nanoparticles"
Submitted.
(Chapter 4)

Articles to which the author also contributed:

(9) Osamu Mamezaki, Hiroaki Adachi, Satoshi Tomita, Minoru Fujii, Shinji Hayashi:
"Thin films of carbon nanocapsules and onion-like graphitic particles prepared by the cosputtering method"
Japanese Journal of Applied Physics, Vol. 39, No. 12A, pp. 6680-6683, December 2000.

(10) Keiko Nakamura, Michael E. Zolensky, Satoshi Tomita, Kazushige Tomeoka:
"In situ observation of carbonaceous globules in Tagish Lake chondrite"
Submitted.

2. **Conference Papers**

(1) Satoshi Tomita, Minoru Fujii, Shinji Hayashi, Keiichi Yamamoto:
"Transformation of carbon onions to diamond by low-temperature heat treatment in air"
Diamond and Related Materials, Vol. 9, pp. 856-860, May 2000.

(2)* Satoshi Tomita, Shinji Hayashi, Yasunori Tsukuda, Minoru Fujii:
"Ultraviolet-visible absorption spectroscopy of carbon onions"
Physics of Solid State, accepted.
(Chapter 4)

An article to which the author also contributed:

(3) John C. Dore, Andrzej Burian, Satoshi Tomita:
"Structural studies of carbon nanotubes and related materials by neutron and x-ray diffraction"
Acta Physica Polonica A, Vol. 98, pp. 495-504, November 2000.